Design for Local Web Shear at Brace Connections: An Adaptation of the Uniform Force Method

RAFAEL SABELLI, BRANDT SAXEY, CHAO-HSIEN LI, and WILLIAM A. THORNTON

ABSTRACT

Recent literature has examined local shear forces in beams in chevron braced frames (Fortney and Thornton, 2015). Subsequently, design methods based on optimal stress distributions to address these shears were developed (Sabelli and Arber, 2017; Sabelli and Saxey, 2021). This paper extends those design methods to gusset connections at columns, utilizing the adaptability of the Uniform Force Method to facilitate design to reduce required member shear strength. The design model presented reduces the required member shear strength required, as compared to the conventional application of the Uniform Force Method. The model allows for redistribution of force from the beam interface to the column interface using a "bypass method," as well as utilizing the gusset plate as part of a moment connection using the "haunch method." Finite element analyses are used to confirm the adequacy of a design employing these methods.

Keywords: gusset plates, braced frames, truss connections.

INTRODUCTION

Design of brace connections requires consideration of local forces induced in the surrounding framing members. Although the discussion of these forces initially focused on beam midspan connections (Fortney and Thornton, 2015), such forces also occur at beam-column-brace connections. These local forces are typically missed by analysis methods that neglect connection dimensions. Richards et al. (2018) studied midspan gussets; their finite element analyses confirm the presence of these local forces, as well as redistribution of stresses similar to those posited by Sabelli and Arber (2017). [A design procedure for beam-to-column connections with full-height gussets based on such a stress redistribution is presented in Sabelli and Saxey (2021).]

The Uniform Force Method (UFM) (Thornton, 1991; Muir and Thornton, 2014; AISC, 2017) is commonly used to analyze forces at gusset-plate connections. It is a powerful tool that permits designers to proportion and optimize connections. This study presents an adaptation of the UFM specifically developed to allow the designer to proportion and analyze connections to reduce required member shear strength and thus to reduce the instances of connections requiring web doublers. Similar to the UFM as originally developed, the methods presented in this paper rely on the lower bound theorem as presented by Thornton (1984) for similar connections, demonstrating adequate strength through investigation of an advantageous load path in a ductile connection and examining forces at gusset edges.

This paper addresses the UFM and adds two options. To further optimize designs, a "bypass" method is developed that permits assigning more of the brace force to the column than is possible using the UFM. This approach recognizes that shear yielding of the beam does not constitute formation of a complete mechanism and that inelastic shear deformation of the beam web requires inelastic deformation of the column web or gusset. (Even inelastic deformation of both the beam web and column web does not constitute a complete mechanism, and additional strength can be mobilized as is discussed in the bypass section.)

Additionally, a "haunch" method is developed, permitting the use of the gusset as part of a moment-resisting connection. Equations are presented for UFM forces; for UFM forces in combination with bypass forces; and for UFM, bypass, and haunch forces combined.

This paper begins with the derivation of design equations for the three methods, along with the combined force equations. For clarity, a summary table presents the equation numbers that apply for the design quantities for each method. Design examples are presented for each method. Finally, there is a brief presentation of validating finite element analyses of one of the design examples.

Each of the methods presented (the adapted Uniform Force Method and the bypass method and haunch method

Rafael Sabelli, Director of Seismic Design, Walter P Moore, San Francisco, Calif. Email: rsabelli@walterpmoore.com (corresponding)

Brandt Saxey, Technical Director, CoreBrace, West Jordan, Utah. Email: brandt.saxey@corebrace.com

Chao-Hsien Li, PhD Candidate, University of California at San Diego, Calif. Email: chl228@eng.ucsd.edu

William A. Thornton, Vice President, Cives Engineering Corporation, Roswell, Ga. Email: bthornton@cives.com

Paper No. 2020-06R

enhancements) depends on the lower-bound theorem to justify the use of a relatively simple design model. While the design model is not intended to produce forces matching those of more sophisticated analytical models, the methods are expected to result in designs with adequate strength. The finite element analyses performed confirm this strength. Additionally, the analyses produce force distributions similar to those determined using the design model.

This paper focuses exclusively on the design of braced-frame-connections to achieve the required strength of each component for a defined set of forces. The design forces considered are brace axial forces, beam axial and shear forces, and (for the haunch method) beam moment. Inelastic deformation demands related to brace buckling are not considered; as such, the methods are appropriate for wind design and for the design of buckling-restrained braced frames but are not sufficient for providing the required ductility of special concentrically braced frames.

Member Shear Checks

The presence of local shears in beam and column webs is necessary for static equilibrium. All beam-column-brace (and truss) connections must resist these forces, regardless of the connection design and analysis techniques used. The shear is due to both the force normal to the member axis and to the moment at the gusset-flange interface. While different analysis methods assign different force distributions, there is no method that eliminates both normal force and moment in connections of members with non-zero depth.

For gusset-plate connections, local member shear may be at a maximum in either of two locations for each member (considering the column above and below the beam as separate members). The maximum member shear may be due to the total normal force, which is fully delivered by the gusset at the section nearest the workpoint. For the column, one such section is just above the beam top flange in Figure 1 (section C1); for the beam, it is at the beam-to-column connection (section B1). Additionally, moments at the gusset-to-column or gusset-to-beam interface may be large enough such that the associated shear in the member at or near the mid-length of the gusset (sections C2 and B2) may exceed the value at C1 and B1.

The member shear checks at C1 and B1 are straightforward. These are simply the normal forces transverse to the member axis delivered by the gussets (horizontal forces for the column; vertical forces for the beam). In the case of a beam such as shown in Figure 1, the transverse forces from the gusset above and below are additive. Similarly, column-shear forces from gussets on opposite column flanges are additive.

At sections C2 and B2, the member shear is a function of both the portion of the normal force delivered between the gusset end and the section in question, and the moment on the gusset-flange interface. The combined effects of flexure and normal force can be analyzed using a number of models, three of which are shown in Figure 2. The elastic and (conventional) plastic distributions are adapted from the AISC *Steel Construction Manual* (2017), hereafter referred to as the AISC *Manual*. The third method, the "concentrated stress method," is described by Sabelli and Saxey (2021).

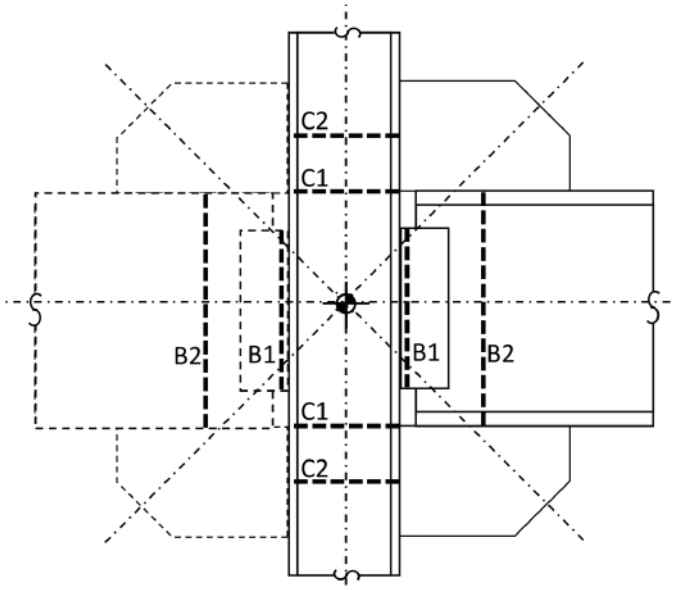

Fig. 1. Sections for shear check in beam and column.

[The results from the concentrated stress method match the "optimized plastic method" from the AISC *Manual* (2017) for cases in which the section is fully plasticized.] In each diagram the flexural stresses are sufficiently large so that the shear at an interior section (B2) is greater than the shear at B1. Note that the precise location of the section B2 varies among the stress-distribution models in Figure 2. For a given combination of moment and normal force, the length required for a limit on the maximum stress differs for each model.

In this paper the conventional plastic distribution is used. In that distribution, the sections B2 and C2 are always at the gusset mid-length, which simplifies the equations derived based on the moments at the gusset interfaces. However, the concentrated stress method requires a lower force to transmit the same moment over the same length and thus can provide for a more efficient design (Sabelli and Saxey, 2021).

Using conventional plastic distribution, the shear at section B2 or C2 is:

$$V_{mid} = \frac{M}{e} + \frac{N}{2} \quad (1)$$

where

L = gusset length, in.

M = moment at gusset interface to beam or column flange, kip-in.

N = normal force on beam or column flange, kips

e = eccentricity in force couple resisting moment M equal to half the gusset length L, in.

This shear loading from Equation 1 must be combined with additional shear that may be present in the member.

Sign Conventions

Figure 3 shows a typical brace-connection diagram. Subscripts are employed in some equations to distinguish actions and dimensions related to one gusset or one brace from another. Gussets are designated 1 and 2. Dimensions and forces associated with each gusset are given the subscript 1 or 2.

Braces have two subscripts. The first pertains to which side of the column the gusset connects to (1 or 2). The second pertains to which of the two braces connecting to a

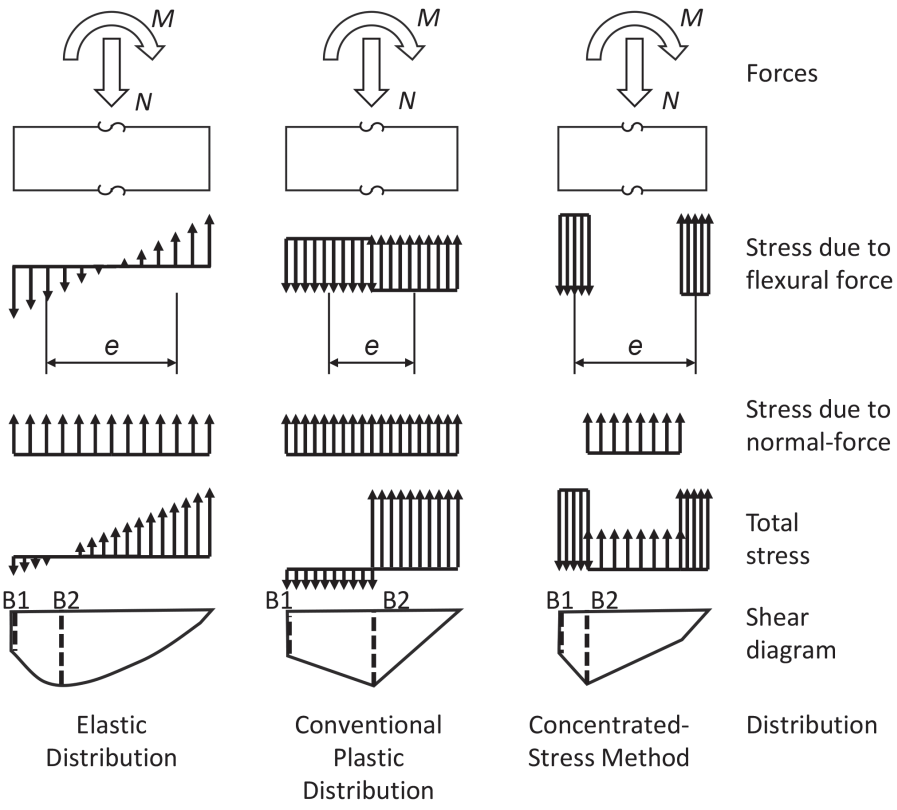

Fig. 2. Stress-distribution models.

beam is indicated (above or below). Sign conventions match the figures such that positive brace axial forces $F_{1,2}$ and $F_{2,1}$ correspond to compression and positive brace axial force $F_{1,1}$ and $F_{2,2}$ correspond to tension. Forces and angles pertaining to each brace carry the same designation subscript.

The term *workpoint* refers to the intersection of brace centerlines with the beam and column centerline. (Eccentric workpoints are not addressed in this paper.)

Sabelli and Saxey (2021) derive local member shears based on a full-height gusset that has continuous thickness. Similar column shears occur in traditional gussets, and similar methods may be employed to utilize the gusset size and an optimal stress distribution to eliminate the need for local reinforcement.

The Uniform Force Method (UFM) (AISC, 2017) is a commonly employed method of analyzing traditional gussets. The UFM utilizes the gusset dimensions 2α and 2β, as well as the beam and column eccentricities e_b and e_c. Note that 2α and 2β are the dimensions of a virtual gusset, and the actual gusset dimensions ($2\overline{\alpha}$ and $2\overline{\beta}$) may be different, as shown in Figure 4 and discussed later. The method presented here is a supplement to the UFM, showing necessary dimensions to eliminate the need for web reinforcement. For additional guidance and background on the application of the UFM readers should consult the AISC *Manual* (AISC, 2017) and AISC Design Guide 29 (Muir and Thornton, 2014).

Force Equations

The UFM defines vertical and horizontal forces at the gusset interfaces with the column and the beam. The column vertical force corresponding to the brace axial force, P, is given by AISC *Manual* Equation 13-2:

$$V_c = \frac{\beta}{r} P \tag{2}$$

where

r = gusset centroid offset from workpoint per AISC *Manual* Equation 13-6:

$$= \sqrt{(\alpha + e_c)^2 + (\beta + e_b)^2} \tag{3}$$

and

P = brace axial force, kips

e_b = eccentricity from beam flange to beam centerline, equal to half the beam depth, in.

e_c = eccentricity from column flange to column centerline, equal to half the column depth, in.

α = distance from column face to centroid of Uniform Force Method force acting on beam flange, in.

β = distance from beam flange to centroid of Uniform Force Method force acting on column face, in.

The column horizontal force is given by AISC *Manual* Equation 13-3:

$$H_c = \frac{e_c}{r} P \tag{4}$$

The beam vertical force is given by AISC *Manual* Equation 13-4:

$$V_b = \frac{e_b}{r} P \tag{5}$$

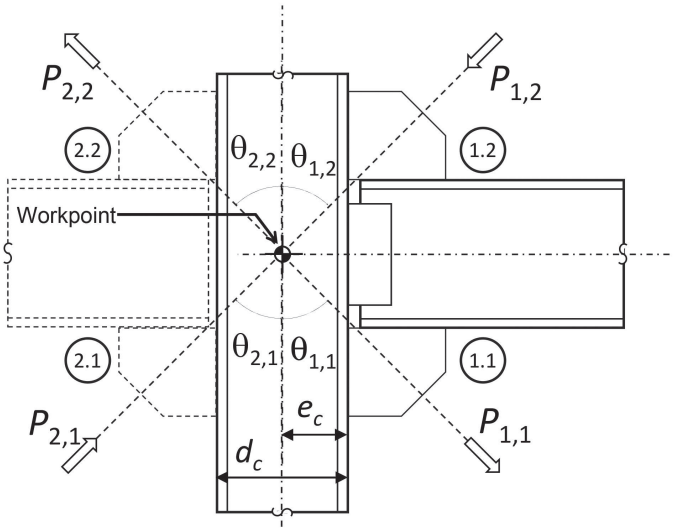

Fig. 3. Diagram with numbering and sign conventions.

The beam horizontal force is given by AISC *Manual* Equation 13-5:

$$H_b = \frac{\alpha}{r} P \tag{6}$$

For both edges of the virtual gusset to be centered on the forces acting on the beam and column flanges, the virtual dimensions α and β must conform to the following relationship (AISC *Manual* Equation 13-1):

$$\alpha - \beta \tan\theta = e_b \tan\theta - e_c \tag{7}$$

where

θ = brace angle from vertical, deg

Equation 7 may also be expressed as:

$$\beta = \frac{\alpha + e_c}{\tan\theta} - e_b \tag{8}$$

Equation 3 may be combined with Equation 7 and Equation 8 thus:

$$r = \frac{e_b + \beta}{\cos\theta} = \frac{e_c + \alpha}{\sin\theta} \tag{9}$$

These relationships may also be expressed as:

$$\alpha = r\sin\theta - e_c \tag{10}$$

$$\beta = r\cos\theta - e_b \tag{11}$$

These virtual dimensions locate the centroids of the forces acting on the beam flange and column flange. As presented here, the UFM gusset forces are constrained to conform to the proportioning relationships defined by Equations 7 through 11, regardless of the actual gusset proportioning. Specifically, Equations 9, 10, and 11 are used to convert the force equations into functions of *r*, which can then be selected to optimize the connection. Thus, although three dimensions (*r,* α, and β) are used in the following equations, they are constrained to each other and represent a single variable in the design.

In the UFM procedure [both as defined by Thornton (1991) and as applied here], these gusset forces act on the beam and column at the points indicated on Figure 4 and are proportioned such that their force vectors pass through "control points" at the beam centerline at the column face (for beam forces H_b and V_b) and at the column centerline at the beam top or bottom elevation (for column forces H_c and V_c).

The virtual dimensions α and β do not necessarily correspond to the centroid of the gusset welds or bolted joints.

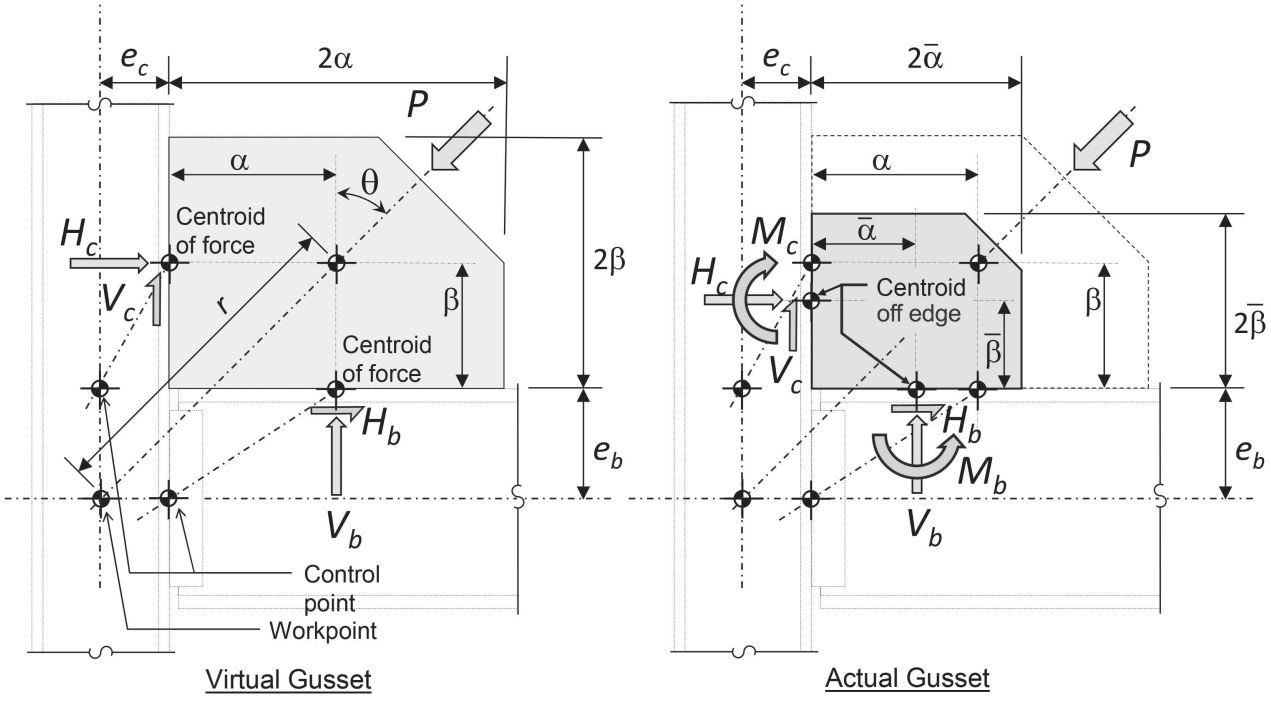

Fig. 4. Uniform Force Method dimensions.

They locate the centroids of the shear and normal forces at the beam or column flange, respectively. At those locations, there is effectively no moment. However, if that location is not also the centroid of the joint (i.e., when the gusset dimension $\overline{\alpha} \neq \alpha$ or $\overline{\beta} \neq \beta$), there is a resulting moment due to the eccentricity. The AISC *Manual* provides methods of determining the relationship between the ideal gusset dimensions (2α and 2β) and actual dimensions ($2\overline{\alpha}$ and $2\overline{\beta}$) and for determining the resulting moments (AISC, 2017). For efficient design, it is convenient to determine the minimum virtual dimensions α and β to control the transverse loading on the column and beam so as to avoid overloading these members in shear and to subsequently select smaller gusset dimensions $2\overline{\alpha}$ and $2\overline{\beta}$ independently (i.e., not constrained to each other) and design the gusset and its interfaces for the resulting combination of normal force, shear force, and moment.

Figure 4 shows the UFM forces acting on the gusset, along with the dimensions used in the UFM. (Forces acting on the member are of opposite sign.) The diagram on the left shows a gusset with virtual dimensions 2α and 2β; forces on the column act at the centroids of the interfaces with the virtual gusset with no moment. The diagram on the right shows the smaller gusset of dimensions $2\overline{\alpha}$ and $2\overline{\beta}$; forces acting at the centroids of the actual gusset edges include moments due to the difference between the virtual and actual gusset dimensions.

In the following derivations, the relationship between α and β defined by Equation 7 is maintained. This simplifies the method, while still permitting independent selection of actual dimensions $2\overline{\alpha}$ and $2\overline{\beta}$ that are not constrained by this relationship.

Using Equations 7 through 11 with Equations 2 through 6, the force equations can be presented in terms of the virtual dimension, r:

$$V_c = \left(\cos\theta - \frac{e_b}{r}\right)P \tag{12}$$

$$H_c = \frac{e_c}{r}P \tag{13}$$

$$V_b = \frac{e_b}{r}P \tag{14}$$

$$H_b = \left(\sin\theta - \frac{e_c}{r}\right)P \tag{15}$$

The larger the virtual dimension, r, the larger the portion of the brace force that is resisted in shear at the interfaces with the column flange and beam flange (V_c and H_b, Equations 12 and 15), and the less is resisted in the normal forces that cause member shear (H_c and V_b, Equations 13 and 14, which are used to evaluate sections C1 and B1, respectively). Subsequent equations solve for the minimum virtual dimension, r, based on those forces in comparison to the member shear strength. From that dimension, the virtual dimensions α and β are defined by Equations 10 and 11. Once those virtual dimensions are computed, the actual gusset dimensions $2\overline{\alpha}$ and $2\overline{\beta}$ are selected. There is not a unique relationship between the force distribution (represented by the virtual dimensions r, α, and β) and the gusset geometry (i.e., $2\overline{\alpha}$ and $2\overline{\beta}$); a range of dimensions $2\overline{\alpha}$ and $2\overline{\beta}$ may be used with the same virtual dimensions α and β, and vice versa. The engineer may optimize the design by selecting values of α and β to produce forces that do not overload the beam (or connection) and column in shear at the B1 and C1 sections and subsequently select among a range of possible gusset dimensions $2\overline{\alpha}$ and $2\overline{\beta}$ that are consistent with those forces and do not overload the beam and column in shear at the B2 and C2 sections.

GUSSETS RESISTING UFM BRACE FORCES ONLY

This section derives closed-form solutions for minimum virtual and actual gusset dimensions based on UFM gusset forces if no other forces are required to be transmitted by the gussets. The subsequent sections develop the (more complicated) equations that include other forces that the designer may elect to assign to the gusset: bypass forces to transfer more force to the column than would result from the application of the UFM and haunch forces for beam-end moments.

Determination of Column Effective Shear Strength

Column and beam shears are readily obtained using the UFM; they are H_c and V_b, respectively, combined with any shear in the member from other sources. (If the moment at the interface is large, the resulting effect on local shear may increase the member shear, as is discussed later.)

$$H_c \leq V_{efCol} \tag{16}$$

where

V_{efCol} = effective column shear strength

The column effective shear strength is reduced by additional shear demands that must be simultaneously resisted by the column. For rigid beam-to-column connections, the moment at the column face due to lateral loads entails a panel-zone shear in the column web and a corresponding shear in the column segments above and below the connection. Typically, the panel-zone shear is not critical as its direction is opposite that of the connection shear induced by the braces. The column shear outside of the panel zone, however, needs to be considered in determining the total shear demand:

$$V_{efCol} = \phi V_n - V_{col} \tag{17}$$

where

V_{col} = column shear due to moment-frame behavior, kips

V_n = nominal member shear strength, kips

ϕ = resistance factor

Determination of Beam and Beam-to-Column Effective Shear Strength

The shear demand from the brace connection must not exceed the beam effective shear capacity, considering this shear demand present in the beam due to lateral loads. Gravity shear, V_g, and frame shear, V_{BMF}, may further reduce the effective beam shear strength:

$$V_{efBm} = \phi V_n - V_g - V_{BMF} \tag{18}$$

where

V_{BMF} = beam shear due to moment-frame behavior, kips

V_g = beam shear due to gravity, kips

When the vertical brace force is acting upward, such as in the case of the braces on left-hand side of Figure 3 (or the case with braces on the right-hand side during the reversal of the indicated force), the gravity shear, V_g, is in the opposite direction of the brace-induced shear, and thus increases the effective shear strength of the beam; reduced-gravity load combinations are appropriate for such cases.

The shear strength of the beam connection to the column, V_{efConn}, may be less than that of the beam:

$$V_{efConn} = \phi R_n - V_g - V_{BMF} \le V_{efBm} \tag{19}$$

where

R_n = nominal strength (of beam-to-column connection), kips

For convenience, a strength ratio, U_C, is defined:

$$U_C = \frac{V_{efConn}}{V_{efBm}} \le 1 \tag{20}$$

Thus,

$$V_{efConn} = U_C V_{efBm} \tag{21}$$

Note that the factor U_c varies with the load combinations that correspond to the shears V_g and V_{BMF}.

Apportionment of Shear Strength for Multiple Gussets

For connections with gussets both above and below (e.g., $P_{1,1}$ and $P_{1,2}$), the column shear must be checked for both separately. For connections with gussets both left and right of the column (e.g., $P_{1,1}$ and $P_{2,1}$), the column forces $H_{c1,1}$ and $H_{c2,1}$ of these gussets are additive, and only a portion of the column shear capacity may be utilized to resist each of these forces. The effective shear capacity of the column, V_{efCol}, must be apportioned between the braces to the left and right of the column (e.g., $P_{1,1}$ and $P_{2,1}$, as shown in Figure 3). In this method, it is apportioned considering their horizontal components as follows:

$$V_{efC1,1} = V_{efCol} \frac{P_{1,1} \sin\theta}{P_{1,1} \sin\theta + P_{2,1} \sin\theta} \tag{22}$$

$$V_{efC2,1} = V_{efCol} \frac{P_{2,1} \sin\theta}{P_{1,1} \sin\theta + P_{2,1} \sin\theta} \tag{23}$$

This apportionment is arbitrary and may be modified based on the demands $H_{c1,1}$ and $H_{c2,1}$. Apportionment as shown in Equations 22 and 23, however, permits independent design of the two gussets.

The condition at the beam is evaluated similarly for connections with both a brace above the beam and another below the beam; only a portion of the beam shear capacity may be utilized to resist each UFM vertical beam force, V_b. The effective shear capacity of the beam, V_{efBm}, must be apportioned between the braces above and below the beam (see Figure 3):

$$V_{efB1,1} = V_{efBm} \frac{P_{1,1} \cos\theta}{P_{1,1} \cos\theta + P_{1,2} \cos\theta} \tag{24}$$

$$V_{efB1,2} = V_{efBm} \frac{P_{1,2} \cos\theta}{P_{1,1} \cos\theta + P_{1,2} \cos\theta} \tag{25}$$

This apportionment applies to both the beam shear strength and the connection shear strength. As with the apportionment of column shear strength (Equations 22 and 23), this apportionment is arbitrary and may be modified based on the demands ($V_{b1,1}$ and $V_{b1,2}$ in this case).

Determination of Minimum Virtual Dimensions

The virtual dimension, r, determines the shear at the column section C1 and the beam section B1, and thus the minimum value for this dimension is established based on the effective shear strength at those sections.

The horizontal force must not exceed the column effective shear strength. Combining Equations 13 and 16 gives:

$$r \ge r_{minCol} = \frac{e_c P}{V_{efC}} \tag{26}$$

where

r_{minCol} = minimum dimension, r, based on column shear yielding, in.

The condition at the beam is evaluated similarly. The shear is set equal to the beam shear capacity (deducting shear due to other sources), and the minimum dimension, r, is derived based on the effective shear capacity of the beam-to-column connection (considering shear demands on the beam not due to the brace force).

The vertical force on the beam due to the brace force

from the UFM analysis is set equal to the effective beam-connection shear strength apportioned to that gusset:

$$V_b \le U_C V_{efB} \tag{27}$$

Per Equation 19, the connection effective shear strength, V_{efConn}, may be limited by the effective beam shear strength, V_{efBm}.

Combining Equation 14 and Equation 27 gives:

$$r \ge r_{minBm} = \frac{e_b P}{U_C V_{efB}} \tag{28}$$

where

r_{minBm} = minimum dimension, r, based on beam shear yielding, in.

The maximum length, r, from the check of the column and the beam controls the design of the gusset (or the need for reinforcement):

$$r \ge \max(r_{minCol}, r_{minBm}) \tag{29}$$

The value of r selected is used in subsequent equations for determination of UFM forces. The corresponding virtual gusset dimensions α and β (determined using Eqs. 10 and 11) are used in the determination of the minimum actual dimensions $\bar{\alpha}$ and $\bar{\beta}$, respectively. Note that by selecting one of these two values (r_{minCol} or r_{minBm}), the design method constrains the corresponding evaluation of member shear (section C1 or B1) to indicate a demand-to-capacity ratio of 1.0. While larger values of the virtual dimension, r, may be used, selection of the lowest value tends to minimize the member shears. It is possible that greater economy in the gusset can be achieved with a larger dimension, r, for designs that can accommodate higher member shear.

Similar designs are performed for each gusset, determining the minimum dimension, r, for beam or connection shear yielding and column shear yielding and apportioning the effective shear strength, considering the gusset on the opposite side of the beam or column for the respective gusset design.

Selection of Actual Gusset Dimensions: Column Interface

As discussed earlier, the minimum virtual gusset dimensions can be established based on the shear strengths at sections C1 and B1, and the minimum actual gusset dimensions can be established based on the virtual dimensions and the shear strengths at sections C2 and B2.

The required gusset dimension $2\bar{\beta}$ at the column is determined based on the combined effects of the force, H_c, corresponding to the virtual gusset dimension, r, and, if $\bar{\beta} \ne \beta$ (as is typical), a moment, M_c, on the gusset-column interface:

$$M_c = H_c(\beta - \bar{\beta}) \tag{30}$$

The larger the deviation of the actual dimension $\bar{\beta}$ from the virtual dimension β, the larger the moment that must be resisted at the gusset interface.

As shown in Figure 5, the column shear at section C2 at the gusset mid-height combines the shear required to transmit the moment with half of the interface horizontal force:

$$V_{mid} = \frac{H_c}{2} + \frac{M_c}{\bar{\beta}} = H_c\left(\frac{\beta}{\bar{\beta}} - \frac{1}{2}\right) \tag{31}$$

This shear must be less than the column effective (apportioned) shear capacity from Equation 17:

$$|V_{mid}| \le V_{efC} \tag{32}$$

The minimum dimension $\bar{\beta}$ may be determined by combining Equations 31 and 32:

$$\bar{\beta} \ge \frac{\beta}{\left|\frac{V_{efC}}{H_c}\right| + \frac{1}{2}} \qquad \text{for } r \ge r_{minCol} \tag{33}$$

The minimum gusset dimension obtained using Equation 33 should be compared to the gusset size required for the brace-to-gusset connection.

If the virtual dimension, r, is equal to r_{minCol}, Equation 33 can be combined with Equations 4 and 26 and simplified to:

$$\bar{\beta} \ge \frac{2}{3}\beta \qquad \text{for } r = r_{minCol} \tag{34}$$

If r is greater than r_{minCol}, Equation 34 will result in a larger value than Equation 33, which gives the true minimum length; nevertheless, Equation 34 may be used for convenience.

Figure 5 shows column shear diagrams in the column due to the effects of the horizontal force, H_c (distributed over the gusset height), and the moment, M_c. (The effects of the vertical force, V_c, are not shown because they do not contribute to column shear.) Two cases are shown. In the upper set of diagrams, the virtual column dimension, r, is selected such that the column shear is exactly equal to the column-effective shear strength, and thus $r = r_{minCol}$. In this case, the column shear at section C1 at the bottom of the gusset, H_c, will equal the effective shear strength, V_{efC}. As such, the shear at section C2 at the midheight, V_{mid}, must not exceed the shear at the bottom, and the moment (and the eccentricity causing the moment) must consequently be limited. In the lower set of diagrams, the column shear at section C1 at the bottom of the gusset, H_c, is less than the effective shear strength, V_{efC}. As such, the shear at section C2 at the gusset mid-height can be larger than the shear at section C1, and a greater moment and eccentricity can be tolerated; a larger eccentricity results from selecting a smaller dimension $\bar{\beta}$.

If $\bar{\beta} > \frac{2}{3}\beta$, the maximum shear occurs at section C1. Conversely, if $\bar{\beta} < \frac{2}{3}\beta$, the maximum shear occurs at section C2. (If $\bar{\beta} = \frac{2}{3}\beta$, the maximum shear occurs for the entire bottom half of the gusset height between sections C1 and C2; this case is not shown in the figure.)

Note that Equation 34 can be used to determine the required shear strength of the column based on a selected gusset size $2\bar{\beta}$ such as might be determined based on the brace-to-gusset connection. Assuming r_{minCol} controls, Equations 9, 13, 16, and 34 can be combined to estimate the required shear strength:

$$V_{efC} \geq \frac{e_c \cos\theta P}{\frac{3}{2}\bar{\beta} + e_b} \tag{35}$$

This value can also be used to design web reinforcement for an already selected column and gusset dimension $2\bar{\beta}$.

Selection of Actual Gusset Dimensions: Beam Interface

The required gusset dimension $2\bar{\alpha}$ at the beam is determined similarly, based on the force distribution corresponding to the virtual gusset dimension α. Similar to the condition at the column, if $\bar{\alpha} \neq \alpha$, there is a moment, M_b, on the gusset-beam interface:

$$M_b = V_b(\alpha - \bar{\alpha}) \tag{36}$$

The shear at section B2 at the gusset mid-length combines the shear required to transmit the moment with half of the interface vertical force:

$$V_{mid} = \frac{V_b}{2} + \frac{M_b}{\bar{\alpha}} = V_b\left(\frac{\alpha}{\bar{\alpha}} - \frac{1}{2}\right) \tag{37}$$

This shear must be less than the beam shear capacity:

$$|V_{mid}| \leq V_{efB} \tag{38}$$

Note that as this check is performed away from the connection, the full (apportioned) beam shear effective strength, V_{efB}, is used without the reduction related to connection effective shear strength, U_C.

The minimum dimension, $\bar{\alpha}$, may be determined by combining Equations 37 and 38:

$$\bar{\alpha} \geq \frac{\alpha}{\left|\frac{V_{efB}}{V_b}\right| + \frac{1}{2}} \quad \text{for } r \geq r_{minBm} \text{ or } V_{efBm} > V_{efConn} \tag{39}$$

The minimum gusset dimension obtained using Equation 39 should be compared to the gusset size required for the brace-to-gusset connection.

If the virtual dimension, r, is equal to r_{minBm}, Equation 39 can be combined with Equation 27 and simplified to:

$$\bar{\alpha} \geq \frac{\alpha}{\frac{1}{U_C} + \frac{1}{2}} \quad \text{for } r = r_{minBm} \text{ and } V_{efBm} > V_{efConn} \tag{40}$$

If $V_{efBm} = V_{efConn}$, Equation 39 can be further simplified to:

$$\bar{\alpha} \geq \frac{2}{3}\alpha \quad \text{for } r = r_{minBm} \text{ and } V_{efBm} = V_{efConn} \tag{41}$$

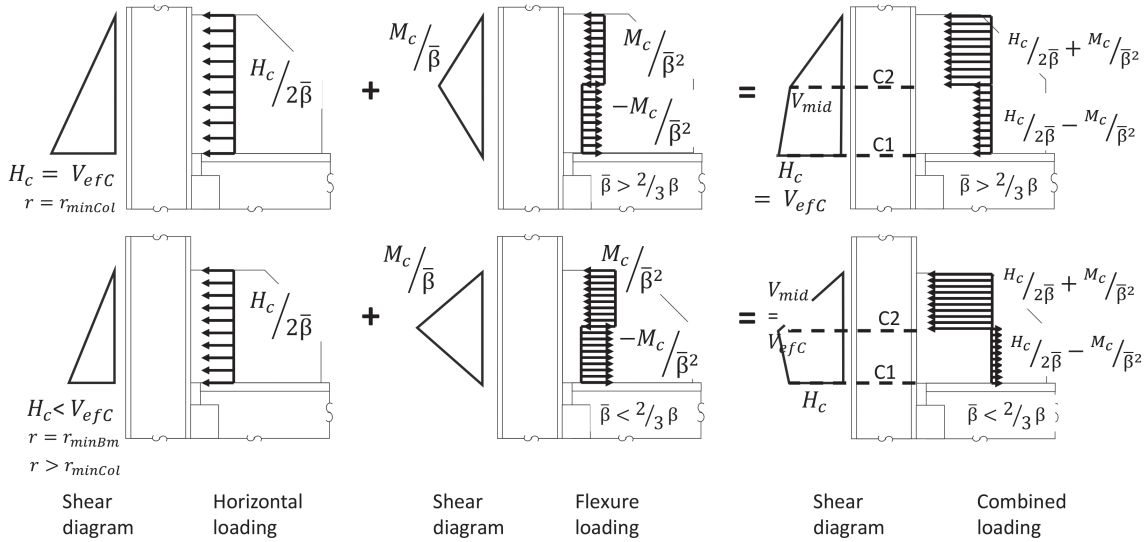

Fig. 5. Shear in column due to horizontal force and moment.

If r is greater than r_{minBm}, Equations 40 and 41 will result in larger values than Equation 39, which gives the true minimum length.

Figure 6 shows beam shear diagrams and vertical loading for two cases. In the upper set of diagrams, the connection effective shear strength, V_{efConn}, is equal to the beam shear effective strength, V_{efBm}. The limit on shear demand at section B1 at the connection, V_b, and the shear demand on section B2 at the gusset mid-length are thus the same. (This occurs when the maximum eccentricity is defined by Equation 41 for cases in which $r = r_{minBm}$ and $V_{efBm} = V_{efConn}$.) In the lower set of diagrams, a connection weaker than the beam is shown ($U_c < 1.0$), and thus a higher shear than V_b can be resisted at the gusset mid-length. (A shear at section B2 higher than V_b results from selection of $\bar{\alpha} < \frac{2}{3}\alpha$. If $\bar{\alpha} > \frac{2}{3}\alpha$, the shear at section B2 is less than V_b; this case is not shown in Figure 6 but is similar to the upper diagrams in Figure 5.)

Similar to Equation 34, Equation 41 can be used to determine the required shear strength of the connection based on a selected gusset size $2\bar{\alpha}$:

$$U_C V_{efB} \geq \frac{e_b \sin\theta P}{\frac{3}{2}\bar{\alpha} + e_c} \tag{42}$$

If the beam shear strength is equal to the connection shear strength (that is, if $U_C = 1.0$), Equation 42 also defines the required beam shear strength. If the connection shear strength is the limiting factor (that is, if $U_C < 1.0$), the required beam shear strength is determined from Equations 5, 28, and 40:

$$V_{efB} \geq \frac{e_b P \sin\theta}{\bar{\alpha}\left(1 + \frac{U_C}{2}\right) + U_C e_c} \tag{43}$$

This value can also be used to design beam-web reinforcement for a given beam and desired gusset dimension $2\bar{\alpha}$.

Selection of Gusset Thickness

The gusset and its connections must be evaluated for the combined effects of moment, horizontal, and vertical forces at both the column interface (M_c, H_c, and V_c), and the beam interface (M_b, H_b, and V_b). The von Mises yield criterion may be used to determine the minimum gusset thickness, t_g, considering forces at the interface with the column:

$$t_g \geq \sqrt{\left(\frac{V_c}{\phi 0.6 F_y 2\bar{\beta}}\right)^2 + \left[\frac{|H_c|}{\phi F_y 2\bar{\beta}} + \frac{|M_c|}{\phi F_y (2\bar{\beta})^2/4}\right]^2} = \frac{1}{\phi F_y 2\bar{\beta}} \sqrt{\left(\frac{V_c}{0.6}\right)^2 + \left(|H_c| + \frac{2|M_c|}{\bar{\beta}}\right)^2} \tag{44}$$

where

F_y = material specified minimum yield stress, ksi

The minimum thickness at the beam interface is similarly determined:

$$t_g \geq \sqrt{\left(\frac{H_b}{\phi 0.6 F_y 2\bar{\alpha}}\right)^2 + \left[\frac{|V_b|}{\phi F_y 2\bar{\alpha}} + \frac{|M_b|}{\phi F_y (2\bar{\alpha})^2/4}\right]^2} = \frac{1}{\phi F_y 2\bar{\alpha}} \sqrt{\left(\frac{H_b}{0.6}\right)^2 + \left(|V_b| + \frac{2|M_b|}{\bar{\alpha}}\right)^2} \tag{45}$$

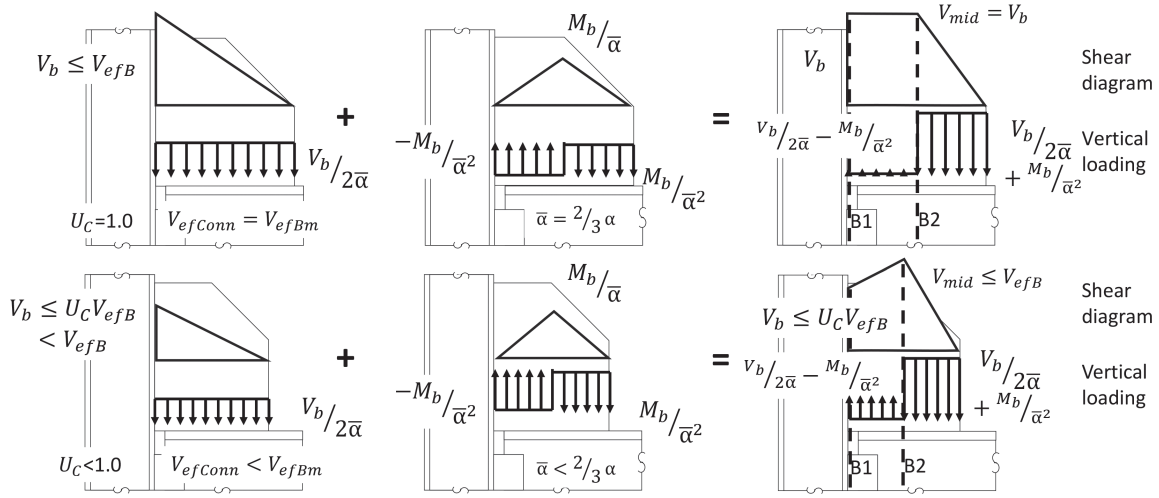

Fig. 6. Shear in beam due to vertical force and moment.

The larger thickness from Equations 44 and 45 should be used. If the required gusset thickness is excessive, a larger value of $\overline{\beta}$ or $\overline{\alpha}$ (as appropriate) may be selected. [If the length $\overline{\beta}$ or $\overline{\alpha}$ required for a certain gusset thickness is desired, the required gusset length is the root of a fourth-power polynomial; various solution methods are available, including trial-and error and computer solvers. A closed-form solution may also be derived using Ferrari's formula (Euler, 1765).]

Normal Forces on Column and Beam

The column and beam should each be evaluated for web local yielding and web crippling for a required strength, R_u, due to the combined effects of normal force and moment over a bearing length, N, of $\overline{\beta}$ or $\overline{\alpha}$, respectively:

$$R_u = V_{mid} = H_c\left(\frac{\beta}{\overline{\beta}} - \frac{1}{2}\right) \tag{46}$$

$$R_u = V_{mid} = V_b\left(\frac{\alpha}{\overline{\alpha}} - \frac{1}{2}\right) \tag{47}$$

GUSSETS RESISTING ADDITIONAL FORCES

The preceding derivations are based on the gussets being designed using the UFM to transmit the brace force to the beam and column. The methods developed (including selection of dimensions to preclude the need for member shear reinforcement) can be extended to gussets designed to resist other forces as well. In the following section, forces corresponding to two refinements are developed: gussets designed with a "bypass" method to transfer more of the brace force to the column (and less to the beam) than would result from the application of the UFM, and gussets acting as moment-transferring haunches. Equations for minimum virtual and actual gusset dimensions considering the total gusset forces (UFM, bypass, and haunch forces) are derived.

Force Transfer from Beam to Column Using Bypass Method

Gussets proportioned in the manner described in the previous section will have sufficient strength and will not cause local yielding in the beam and column webs. Nevertheless, such gussets may be overly large or otherwise undesirable, or such a design might entail reinforcing the web of one of the members (typically the beam). Additionally, the shear yielding of the web of one of the members does not constitute a complete plastic mechanism; both webs must yield to allow this to occur.

In fact, a complete mechanism requires extensive shear yielding of both member webs over the entire gusset region and diagonal elongation of the gusset in the direction transverse to the brace axis. Such a mechanism engages member shear and flexure outside of the connection region. When, as is typical, such forces are not considered in the member design, the design of the connection, to be consistent, should not depend on such forces. In such cases, the complete mechanism is limited by the capacity of the beam and column to withstand flexural forces not considered in the design in conjunction with the axial forces and other actions that were considered. The mechanism may nevertheless represent significant reserve strength over that of the design.

Often there is a great deal of economy to be achieved by taking advantage of the additional capacity of the column to relieve the beam of some of the force. The UFM provides a method of transferring some of the vertical force: "Special Case #2" (AISC, 2017). An alternative method is presented here in which the brace force is divided into two components: a "UFM force" that is delivered to the column and beam per the method described above and a "bypass force" that is delivered only to the column. The apportionment is achieved by selecting a factor, λ, between 0.0 and 1.0. The UFM portion of the force is λP and is addressed using the UFM as described previously (with modified effective column shear strength). The remaining bypass force is $(1-\lambda)P$ and is assigned to the column, which must resist the additional vertical and horizontal forces, as well as the corresponding moment. Note that for the design approach anticipated (in which $\overline{\beta} < \beta$), this moment is in the opposite direction from the UFM column moment. The factor, λ, may be selected to reduce the required length of gusset on the beam or to eliminate the overstress in the beam that would necessitate a web doubler.

The resulting column forces due to the bypass force are:

$$H_{cBP} = (1-\lambda)P\sin\theta \tag{48}$$

$$V_{cBP} = (1-\lambda)P\cos\theta = \frac{H_{cBP}}{\tan\theta} \tag{49}$$

$$M_{cBP} = H_{cBP}(e_b + \overline{\beta}) - V_{cBP}e_c \tag{50}$$

where

λ = brace force apportionment factor

Figure 7 shows these forces acting on the gussets.

If the beam strength is the limiting factor in sizing the virtual gusset ($r = r_{minBm}$ and $V_{efConn} = V_{efBm}$), the factor, λ, required to avoid beam web doublers may be obtained by modifying Equation 42:

$$\lambda \le \frac{V_{efB}}{e_b \sin\theta P}\left[\frac{3}{2}\overline{\alpha} + e_c\right] \tag{51}$$

If the beam strength is not the limiting factor, the λ factor required to avoid beam web doublers may be obtained by modifying Equation 43:

$$\lambda \le \frac{V_{efB}}{e_b \sin\theta P}\left[\bar{\alpha}\left(1+\frac{U_C}{2}\right)+U_C e_c\right] \tag{52}$$

If this bypass-force method is used, Equations 26 and 28 should be modified as follows:

$$r_{minCol} = \frac{\lambda P e_c}{V_{efC} - H_{cBP}} \tag{53}$$

$$r_{minBm} = \frac{\lambda P e_b}{U_C V_{efB}} \tag{54}$$

Similarly, the equations for minimum values of $\bar{\beta}$ and $\bar{\alpha}$ must be modified to address bypass forces; Equations 33 and 39 are not valid for such cases. Modified equations (Equations 77 and 78) considering total forces and moments (including haunch forces) are presented in a subsequent section.

Equations 53 and 54 may be combined with Equation 48 to facilitate member selection. The result is an equation for λ:

$$\lambda = 1 - \frac{V_{efC} - \dfrac{e_c}{e_b} U_C V_{efB}}{P \sin\theta} \tag{55}$$

This can be combined with Equation 52 to derive the required relationship between horizontal gusset length and column and beam connection strength:

$$\bar{\alpha} \ge \frac{e_b P \sin\theta - V_{efC} e_b}{V_{efB}\left(1+\dfrac{U_C}{2}\right)} \tag{56}$$

The bypass method can be used to design connections that satisfy this relationship to preclude the need for reinforcement.

In some circumstances, it may be convenient to transfer force from the column to the beam (rather than from the beam to the column). In such circumstances the engineer may either derive similar bypass equations for the beam or may use a value of λ greater than 1.0, increasing the beam UFM forces and reducing the total column forces.

Use of Gussets as Haunches for Moment Transfer

It is possible to transfer the beam moment utilizing the gusset as a haunch as shown in Figure 8. The use of gussets as haunches will affect the force transfer at the gusset edges, and these forces must be combined with those related to the brace axial force. The resulting equations for the minimum virtual gusset dimension, *r*, to preclude shear yielding (determined in a subsequent section), and the corresponding virtual dimensions α and β, are necessarily more complicated. For convenience, the method presented utilizes the beam moment at the column face, M_f, rather than at a location based on the (as yet undetermined) gusset horizontal dimension. Thus, if the moment is based on beam flexural strength (as might be the case for seismic design) projection of that moment based on an assumed gusset dimension and corresponding beam shear is necessary.

$$M_f = M_{BM} + V_{BMF}(2\bar{\alpha}) \tag{57}$$

where

M_{BM} = moment at a beam section aligned with the gusset edge face, kip-in.

The designer has some discretion in selecting the height of the force couple utilized. To permit independent design

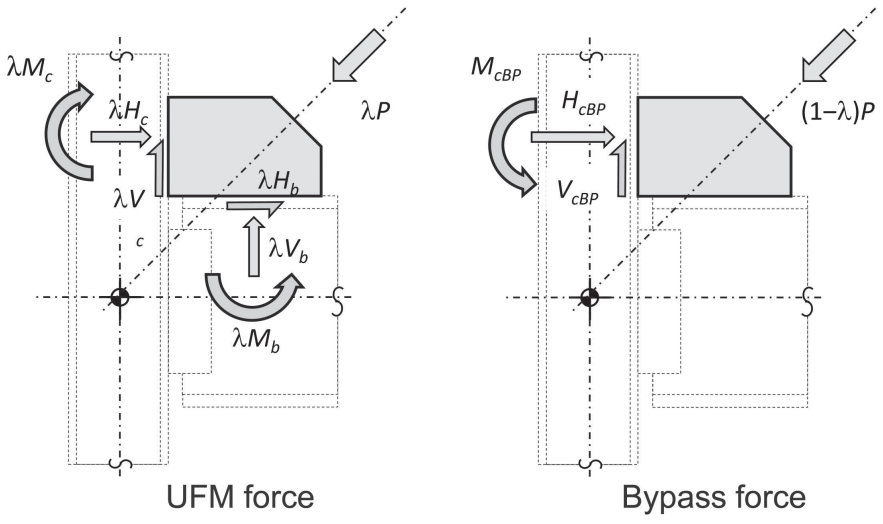

Fig. 7. Force proportioning.

of the gusset (considering the possibility of no gusset on the opposite beam flange or a gusset of yet-to-be-determined size), the gusset is assigned one-half of the beam moment to be resisted by a force couple over a vertical distance from the beam centerline to the virtual gusset centroid defined by β. (Other values of this depth may be used, but this value provides for efficient gusset designs using simpler equations in determining the appropriate dimension, β.)

As shown in Figure 8, at conditions with a gusset, the horizontal force that forms part of this moment-resisting force couple may be resisted by the beam flange connection to the column, the gusset, or a combination of the two.

The value of the moment is ½M_f, assuming that the moment is resisted by two force couples: one involving the top flange or gusset and the web connection and the other involving the bottom flange or gusset and the web connection. If the connection involves only the top, for example, and there is no bottom gusset and no bottom-flange connection to the column, the value of the moment assigned to the top flange or gusset and beam web force couple is the full M_f.

The moment is apportioned between a beam-connection moment, M_{BC}, and a haunch moment, M_H, using a distribution factor ρ (between 0.0 and 1.0); thus:

$$M_{BC_{i,j}} = \frac{\rho_{i,j} M_{fi}}{2} \tag{58}$$

where

$$M_{H_{i,j}} = (1-\rho_{i,j})\frac{M_{fi}}{2} \tag{59}$$

ρ = beam moment apportionment factor (between beam flange and haunch force in gusset)

Thus, the total moment from beam "i," M_{fi}, is divided into four (potential) parts:

$$M_{fi} = M_{BC_{i,1}} + M_{BC_{i,2}} + M_{H_{i,1}} + M_{H_{i,2}} \tag{60}$$

It is expected, however, that in most cases, ρ will be selected as either 1.0 or 0.0 for each flange of each beam as is shown in Figure 8, and thus two of the components of Equation 60 will be of zero value.

For simplicity, the beam-connection moment is assigned to the beam flange as a force, P_f:

$$P_{f_{i,j}} = \frac{M_{BC_{i,j}}}{½ h_{o_i}} = \frac{\rho_{i,j} M_{f_i}}{h_{o_i}} \tag{61}$$

where

h_o = distance between beam flange centroids

The haunch moment results in a horizontal force, H_{cH} (gusset-designation subscripts omitted):

$$H_{cH} = \frac{M_H}{\frac{d_b}{2}+\beta} = \frac{(1-\rho)M_f}{2(e_b+\beta)} \tag{62}$$

where

d_b = beam depth, in.

To satisfy equilibrium, there is an opposite horizontal force, H_{bH}, at the gusset interface with the beam:

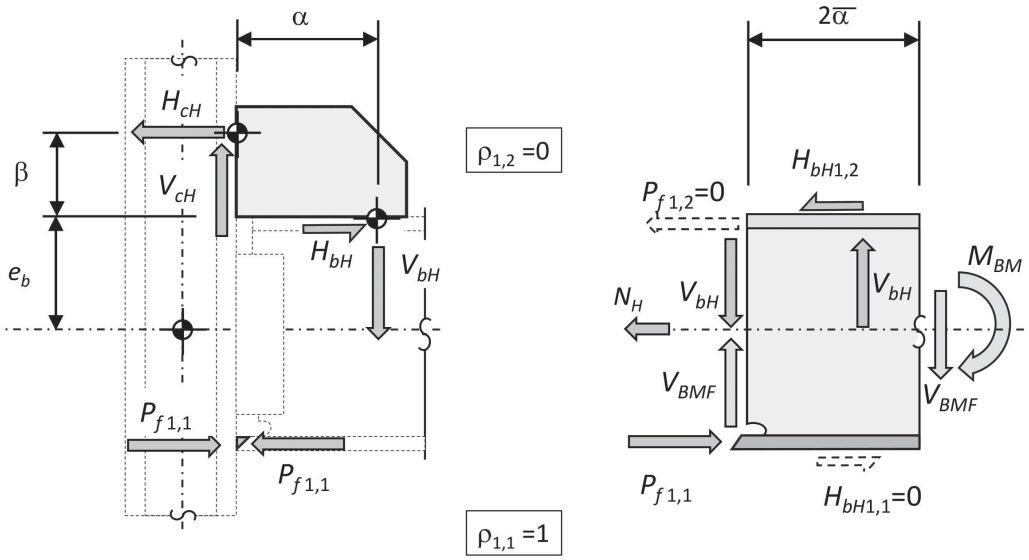

Fig. 8. Gusset plates acting as haunches.

$$H_{bH} = H_{cH} \tag{63}$$

The eccentricity between H_{cH} and H_{bH} is β, and there is thus a moment, βH_{cH}, that must be resolved. A counteracting force couple is determined, with a vertical force, V_{cH}, at the column flange and an opposite vertical force, V_{bH}, which is assigned to the location α for simplicity:

$$V_{bH} = V_{cH} = \frac{\beta H_{cH}}{\alpha} \tag{64}$$

At the gusset centroid, H_{cH} causes a moment, M_{cH}, due to the eccentricity between β and $\bar{\beta}$:

$$M_{cH} = (\beta - \bar{\beta}) H_{cH} \tag{65}$$

The moment due to the vertical force at the beam interface, M_{bH}, is:

$$M_{bH} = (\alpha - \bar{\alpha}) V_{bH} \tag{66}$$

The horizontal force acting at the beam midheight may not completely cancel with the horizontal force from the remaining half of the moment addressed at the opposite flange, potentially necessitating a small additional force, N_H, to be resisted at the beam-to-column connection. As shown in Figure 8, the horizontal force acting on the beam at one flange ($P_{f1,2} + H_{bH1,2}$) has a corresponding force at the opposite flange resisted by a combination of flange and gusset forces ($P_{f1,1} + H_{bH1,1}$). Due to potentially different values of ρ used in Equations 58 and 59, and potentially different moment arms used to determine these forces in Equation 62, the horizontal forces at opposite flanges may not be equal, and the difference must be resisted in the beam web-to-column connection to satisfy equilibrium. This force, N_H, is:

$$N_H = P_{f1,2} + H_{bH1,2} - \left[P_{f1,1} + H_{bH1,1}\right] \tag{67}$$

The haunch method may be used in conjunction with the UFM with or without applying the bypass method.

Total Gusset Forces: UFM, Bypass, and Haunch Forces

Figure 9 shows these forces acting on the gusset edges. Forces shown are gusset forces; member forces are equal and opposite. Note that the beam UFM forces are reduced by the factor λ. In most cases, the haunch forces can have a beneficial effect; the designer should consider whether it is appropriate to neglect that term or take a reduced value to address uncertainty in the level of moment. For seismic design, the potential for cyclic inelastic drift may result in moments in the opposite direction of those shown, which could be a more critical case. Determination of appropriate combinations of design forces is outside of the scope of this study. At a minimum, connections should have sufficient strength to resist maximum brace forces and maximum beam forces both combined with each other (with consistent directions of forces as shown) and separately.

The direction of the UFM, haunch, and bypass column forces is shown in Figure 9. The resulting total column forces (considering the direction of each component) are determined:

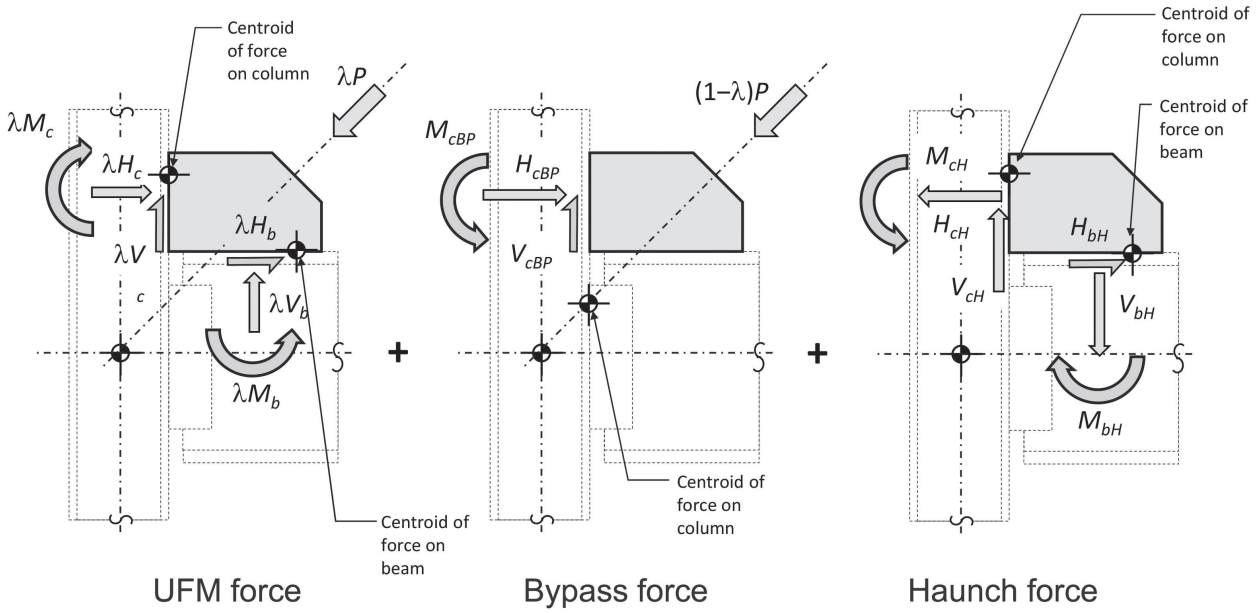

Fig. 9. Total gusset forces.

$$H_{cTot} = \lambda H_c + H_{cBP} - H_{cH} \quad (68)$$

$$V_{cTot} = \lambda V_c + V_{cBP} + V_{cH} \quad (69)$$

$$M_{cTot} = \lambda M_c - M_{cBP} - M_{cH} \quad (70)$$

The shear in the column panel zone is:

$$V_{PZ} = H_{cTot} - P_f \quad (71)$$

The total beam forces (including the UFM, haunch, and bypass forces) are:

$$H_{bTot} = \lambda H_b + H_{bH} \quad (72)$$

$$V_{bTot} = \lambda V_b - V_{bH} \quad (73)$$

$$M_{bTot} = \lambda M_b - M_{bH} \quad (74)$$

These equations are used to select the minimum virtual dimension, r, considering the shear loading of the column, H_{cTot}, at the beam flange and the shear loading of the beam, V_{bTot}, at the column flange. Once this is selected, the actual dimensions $2\bar{\alpha}$ and $2\bar{\beta}$ may be selected considering the shear loading of the column and beam at the mid-length of the gusset as it is affected by the moments (M_{cTot} and M_{bTot}) that are functions of these dimensions. The interface moments are then computed based on the selected dimensions and are used in conjunction with the vertical and horizontal forces to design the gusset and its connections to the beam and column.

Figure 10 shows a free-body diagram of the gusset. The centroid of the UFM column force, λH_c, is at the location defined by the virtual dimension, β, which is typically greater than $\bar{\beta}$, causing a moment, λM_c, (when evaluated at the centroid of the gusset-column interface.). The haunch force, H_{cH}, (which acts in the direction opposite to λH_c) is applied at the same elevation, and the bypass force, H_{cBP}, (which acts in the same direction as λH_c) is located on the brace centerline where it crosses the column face; these two forces cause moments in the opposite direction of M_c.

Minimum Virtual Gusset Dimensions Considering Haunch and Bypass Forces

In previous sections, Equations 26 and 28 provide the minimum virtual dimensions, r, for cases with UFM forces only; Equations 53 and 54 address combined UFM and bypass forces. If haunch forces are included in the gusset design, equations for minimum virtual dimensions, r, become more complicated (but nevertheless solvable). A satisfactory value for this virtual dimension can be determined by trial and error, such that the beam and column are not overloaded in shear by V_{bTot} and H_{cTot}, respectively. Alternatively, the following methods can be used.

Combining Equations 16 and 68 results in a quadratic equation for the minimum virtual dimension, r, considering column web shear, r_{minCol}:

$$r_{minCol}^2\left[(V_{efC} - H_{cBP})\cos\theta\right] + r_{minCol} \left[(V_{efC} - H_{cBP})(e_c - e_b) + (1-\rho)\frac{M_f}{2} - \lambda P e_c \cos\theta\right] + \left[\lambda P e_c (e_b - e_c)\right] \geq 0 \quad (75)$$

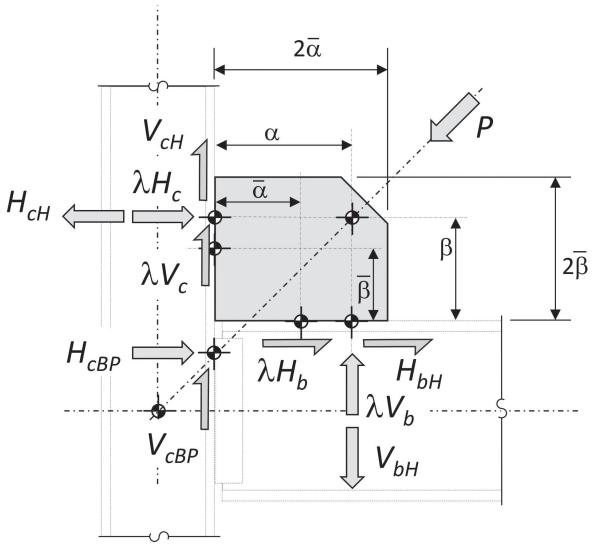

Fig. 10. Free-body diagram of gusset.

Combining Equations 28 and 73 results in a quadratic equation for the minimum virtual dimension, r, considering beam web shear:

$$r_{minBm}^2\left[\sin\theta U_c V_{efBm}\right] + r_{minBm}\left[M_H - e_c U_c V_{efBm} - \lambda P e_b \sin\theta\right] + \left[\lambda P e_b e_c - M_H \frac{e_b}{\cos\theta}\right] \geq 0 \quad (76)$$

The largest of the roots from Equations 75 and 76 is used. Excessively large values of the minimum dimension, r, may indicate that more of the moment, M_f, should be transferred by the beam flanges. Note also that both the effective column shear strength, V_{efCol}, in Equation 75 and the effective beam shear strength, V_{efB}, in Equation 76 include terms that, similar to M_f, are reflective of the moment-frame behavior, and the use of consistent loads is recommended. As discussed in the design examples, consideration of cases without these flexural forces may be appropriate to address the range of possible conditions.

Equation 76 presupposes a value of λ. If the design considers both the condition with moment and the condition with moment equal to zero (for which haunch forces are likewise zero), Equation 52 may be used to select a value of λ for the latter condition. As illustrated in the design example, the value of λ determined for the zero-moment condition may be sufficient for all conditions; otherwise, trial and error may be used.

The maximum virtual dimension, r, from the check of the column and the beam from Equations 75 and 76 controls the design of the gusset (or the need for reinforcement), and therefore, the larger value should be used for the virtual dimension, r, in subsequent equations per Equation 29. As the haunch forces causing shear in the beam and column are opposite those from the Uniform Force Method for the typical direction of moment, member shear may not always be a governing consideration. Thus, selection of the minimum permissible value of the virtual dimension, r, may not be the most economical choice in all cases; the gusset thickness could be optimized in some cases by selecting a higher value of r. The authors have not developed equations to solve for this optimum value; trial and error may be used. Note that if the design also considers a case without the moment, that latter case typically is governed by beam shear and governs the required gusset thickness.

Minimum Actual Gusset Dimensions Considering Haunch and Bypass Forces

The minimum gusset dimension, $2\bar{\beta}$, is governed by the shear in the column at the gusset mid-height; $\bar{\beta}$ is defined by combining Equations 16, 31, 68, and 70:

$$\bar{\beta} \geq \left(\beta - \frac{\alpha}{\tan\theta}\frac{H_{cBP}}{H_{cTot}}\right)\frac{1}{\left|\frac{V_{efC}}{H_{cTot}}\right| + \frac{1}{2}} \quad (77)$$

The minimum gusset dimension, $\bar{\alpha}$, is likewise determined by combining Equations 27, 37, 73, and 74:

$$\bar{\alpha} \geq \frac{\alpha}{\left|\frac{V_{efB}}{V_{bTot}}\right| + \frac{1}{2}} \quad (78)$$

Note that this is based on the beam shear at the gusset mid-length, and thus the connection factor, U_C, is not used.

Designers may wish to begin trials using Equations 77 and 78 with $\lambda = 1.0$ (i.e., with no bypass force). If the gusset dimension $2\bar{\alpha}$ is excessive, the value of λ may be decreased and the dimension $\bar{\beta}$ may be selected using Equation 77.

Beam-Web-to-Column Connection

The sum of the horizontal forces at the beam web-to-column connection, H_{bW}, is:

$$H_{bW} = N_B + H_{bTot1,2} - H_{bTot1,1} + N_H \quad (79)$$

where

N_B = beam axial force delivered to the connection, kips

Note that the horizontal forces, H_b, from the gussets above and below counteract each other. For connections with only one gusset, the required strength of this connection will be significantly larger; this may be an important consideration in determining how much force to divert using the bypass method, which increases H_b.

The sum of the vertical forces at the beam web-to-column connection, V_{bW}, is:

$$V_{bW} = V_g + V_{BMF} + V_{bTot1,2} + V_{bTot1,1} \quad (80)$$

The forces in the beam flange are given in Equation 61. These web and flange forces are shared with the gusset plate, and the designer should avoid connecting the beam to column in a manner that is not compatible with the connection of the gusset to column such as a welded gusset connection and bolted beam-web connection.

DESIGN OF WELDS

At a minimum, the welds connecting the gusset plates must be capable of transferring the forces at the joint determined for the design of the gusset. In some cases, such welds may be insufficient to develop the full strength of the gusset plate. As the design methods presented here utilize the lower-bound theorem, the ductility of such weak-weld/strong-gusset joints must be demonstrated. It is important

Table 1. Summary of Equations			
Design Quantity	**UFM Method**	**Bypass Method**	**Haunch Method**
λ	—	(52) or (55)	—
V_{efCol}	(17)		
Required V_{efC}	(35)	(35) [λP for P] or (55)	
V_{efBm}, V_{efConn}	(18), (19)		
U_C	(20)		
$U_C V_{efB}$ [below; above]	(24), (25)		
Required $U_C V_{efB}$	(42)	(42) [λP for P]	
Required V_{efB}	(43)	(43) [λP for P]	
r_{minCol}	(26)	(53)	(75)
r_{minBm}	(28)	(54)	(76)
r	(29)		
α, β	(10), (11)		
V_c, H_c, V_b, H_b	(2), (4), (5), (6)		
H_{cBP}, V_{cBP}	—	(48), (49)	—
H_{cH}, H_{bH}	—	—	(62), (63)
V_{cH}, V_{bH}	—	—	(64)
H_{cTot}, V_{cTot}	—	(68), (69)	
H_{bTot}, V_{bTot}	—	(72), (73)	
Required $\overline{\beta}$	(33)	(77)	
Required $\overline{\alpha}$	(40)	(78) or (56)	(78)
M_c	(30)		
M_{cBP}	—	(50)	—
M_{cH}	—	—	(65)
M_{cTot}	—	(70)	
M_b	(36)		
M_{bH}	—	—	(66)
M_{bTot}	—	(74)	
V_{mid} (column, beam)	(31), (37)		
t_g	Maximum of (44) and (45)		

to consider that the redistributions required to engage other elements necessitates that separate joints in the connection deform together. For example, the limitation of the gusset-to-beam forces in the bypass method may assign more force to the beam-to-column connection, and the deformation demands on the two weld groups are not independent. In the absence of a nonlinear or mechanism analysis demonstrating that weld deformations are within their rupture limit, design of the weld for the gusset plate strength ensures the ductility of the joint by favoring inelastic deformation of the gusset or the web of the member over rupture of the weld.

SUMMARY OF EQUATIONS

The preceding discussion includes many intermediate equations necessary for derivation of the design equations. Additionally, some equations have multiple forms: simpler equations for the UFM and more terms with the introduction of bypass and haunch forces. Table 1 presents the equation numbers to be used for the determination of design quantities for the UFM, bypass, and haunch methods. (The haunch method equations include bypass forces.) Certain equations developed for the UFM are modified by substituting λP for P; this is indicated in the table.

Table 2. Brace Forces			
	P (kips)	$P_{cos}\theta$ (kips)	$P_{sin}\theta$ (kips)
$P_{1,1}$	550	352	423
$P_{1,2}$	460	295	353

DESIGN EXAMPLES

The connection shown in Figure 11 will be designed using the methods developed in this study.

The design is performed three times:

- Preliminary design (wind loads). The gusset is designed using UFM method without bypass forces.
- Redesign with bypass forces (wind loads). The gusset is redesigned using UFM and bypass to eliminate web reinforcement.
- Seismic design including haunch forces (and bypass forces).

The design forces are presented in Table 2. To facilitate subsequent calculations, the horizontal and vertical components of the brace forces are determined and presented in the table. (P denotes the axial force in the brace.) The angle from vertical, θ, is 50.2°.

To facilitate comparison, the same brace axial forces are used for both the wind-load and seismic-load designs.

The beam and column forces delivered to the connection are shown in Table 3.

The seismic forces correspond to the formation of plastic hinges at each end of the beam, represented by the symbol E_{cl}. The plastic-hinge moment is the maximum flexure that the beam can deliver and is thus not combined with the gravity moment, although the corresponding shear is additive to the gravity shear. The plastic-hinge moment is 1.1 times the beam expected

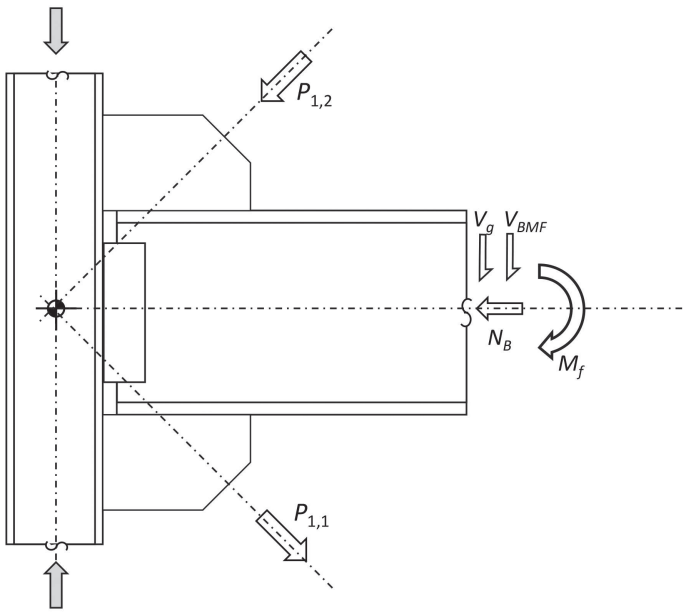

Fig. 11. Design example connection.

Table 3. Beam and Column Forces			
Load Case or Combination		**Load**	**Force**
Gravity	$1.2D + L$	V_g	10 kips
		M_f	100 kip-in.
Wind	$1.0W$	V_{BMF}	7.1 kips
		M_f	not used
		V_{col}	17.1 kips
Seismic	E_{cl}	V_{BMF}	44.9 kips
		M_f	7770 kip-in.
		V_{col}	108 kips
Gravity + wind	$1.2D + L + 1.0W$	$V_g + V_{BMF}$	17.1 kips
		M_f	not used
Gravity + seismic	$1.2D + L + 1.0E_{cl}$	$V_g + V_{BMF}$	54.9 kips
	$0D + 0L + E_{cl}$	M_f	7770 kip-in.

Table 4. Member Sizes and Grades		
Member	**Size**	**Grade**
Column	W14×120	50 ksi
Beam	W18×55	50 ksi
Gussets	—	50 ksi

beam flexural strength, as required for the design of Special Concentrically Braced Frames and Buckling-Restrained Braced Frames in the AISC *Seismic Provisions* (AISC, 2016) Sections F2.6b(b) and F4.6b(b), respectively.

The member sizes and materials are shown in Table 4. Members are ASTM A992 material, and plate is ASTM A572 material.

The connection strength is based on a 15-in.-deep portion of the beam complete-joint-penetration (CJP) welded to the column flange:

$\phi R_n \geq 176$ kips

Based on the brace-to-gusset connection (not shown in this example), minimum dimensions for the gusset plate are 23 in. wide and 17 in. high. The dimensions used for calculation allow for an extra inch for weld termination. The minimum gusset interface centroids are:

$\bar{\beta} \geq 8$ in.

$\bar{\alpha} \geq 11$ in.

1. Preliminary Design: Design of Top Gusset (with No Bypass or Haunch Force)

The following example shows the design of the top gusset to resist the force $P_{1,2}$. The design considers the effect of the force $P_{1,1}$ on the beam, but otherwise the two gusset designs are independent of each other.

For preliminary design, the gusset will be proportioned to resist brace forces only, assuming the beam moment is transferred to the column by the flanges (i.e., $\rho = 1.0$). Similarly, the bypass-force method will not be used. Both of these methods are addressed in a gusset redesign.

Column Effective Shear Strength

The effective column shear strength is reduced considering the column shear.

$$V_{col} = 17.1 \text{ kips}$$

$$\begin{aligned} V_{efCol} &= \phi V_n - V_{col} \\ &= 257 \text{ kips} - 17.1 \text{ kips} \\ &= 240 \text{ kips} \end{aligned} \tag{17}$$

Using Equation 35, the minimum shear strength is:

$$\begin{aligned} V_{efCol} &= V_{efC} \\ &\geq \frac{e_c \cos\theta P}{\frac{3}{2}\overline{\beta} + e_b} \\ &= \frac{(7.25 \text{ in.})0.640(460 \text{ kips})}{\frac{3}{2}(8.0 \text{ in.}) + (9.05 \text{ in.})} \\ &= 101 \text{ kips} \end{aligned} \tag{35}$$

Beam Effective Shear Strength

The effective beam shear strength is limited by the strength of the connection and is reduced considering the beam shear:

$$\begin{aligned} V_{efBm} &= \phi V_n - V_g - V_{BMF} \\ &= 212 \text{ kips} - 10.0 \text{ kips} - 7.1 \text{ kips} \\ &= 195 \text{ kips} \end{aligned} \tag{18}$$

$$\begin{aligned} V_{efConn} &= \phi R_n - V_g - V_{BMF} \\ &= 176 \text{ kips} - 10.0 \text{ kips} - 7.1 \text{ kips} \\ &= 158 \text{ kips} \end{aligned} \tag{19}$$

$$\begin{aligned} U_C &= \frac{V_{efConn}}{V_{efBm}} \\ &= \frac{158 \text{ kips}}{195 \text{ kips}} \\ &= 0.814 \end{aligned} \tag{20}$$

The apportioned effective beam shear strength that can be utilized for each gusset can be apportioned considering the vertical components of the brace forces:

$$\begin{aligned} U_C V_{efB1,1} &= U_C V_{efBm} \frac{P_{1,1}\cos\theta}{P_{1,1}\cos\theta + P_{1,2}\cos\theta} \\ &= 0.814(195 \text{ kips}) \frac{352 \text{ kips}}{352 \text{ kips} + 295 \text{ kips}} \\ &= 86.2 \text{ kips} \end{aligned} \quad \text{(from Eq. 24)}$$

$$\begin{aligned} U_C V_{efB1,2} &= U_C V_{efBm} \frac{P_{1,2}\cos\theta}{P_{1,1}\cos\theta + P_{1,2}\cos\theta} \\ &= 0.814(195 \text{ kips}) \frac{295 \text{ kips}}{352 \text{ kips} + 295 \text{ kips}} \\ &= 72.1 \text{ kips} \end{aligned} \quad \text{(from Eq. 25)}$$

Using Equation 42, the minimum apportioned effective connection shear strength is:

$$U_C V_{efB1,2} \geq \frac{e_b \sin\theta P}{\frac{3}{2}\bar{\alpha} + e_c} \quad \text{(from Eq. 42)}$$

$$= \frac{(9.05 \text{ in.})(0.768)(460 \text{ kips})}{\frac{3}{2}(11.0 \text{ in.}) + (7.25 \text{ in.})}$$

$$= 135 \text{ kips} > 72.1 \text{ kips}$$

Reinforcement is therefore required.

The beam shear strength is apportioned:

$$V_{efB1,2} = V_{efBm} \frac{P_{1,2} \cos}{P_{1,1} \cos\theta + P_{1,2} \cos\theta} \quad (25)$$

$$= (195 \text{ kips})(0.455)$$

$$= 88.7 \text{ kips}$$

The minimum apportioned effective beam shear strength is:

$$V_{efB} \geq \frac{e_b P \sin\theta}{\bar{\alpha}\left(1 + \frac{U_C}{2}\right) + U_C e_c} \quad (43)$$

$$= \frac{(9.05 \text{ in.})(460 \text{ kips})(0.768)}{(11.0 \text{ in.})\left(1 + \frac{0.814}{2}\right) + 0.814(7.25 \text{ in.})}$$

$$= 150 \text{ kips} > 88.7 \text{ kips}$$

Because $V_{efB} > V_{efB1,2}$, reinforcement is required.

If the proposed gusset length is to be used, both the connection strength and the beam strength are insufficient. Based on the degree of this deficiency, it is anticipated that an unreinforced beam will require an excessively long gusset. (In fact, calculations were performed, and the required horizontal length exceeds 42 in.) Instead, the web will be reinforced with a ⅜-in. doubler, 15 in. deep (matching the available web depth of the connection) and extending horizontally to match the gusset length. The reinforced strength for both the connection and the beam is determined and apportioned as before. The additional strength is:

$$\phi R_n \geq \phi 0.6 F_y dt$$

$$= (1.0)(0.6)(50 \text{ ksi})(15 \text{ in.})(⅜ \text{ in.})$$

$$= 169 \text{ kips}$$

The beam strength is:

$$\phi V_n = 212 \text{ kips} + 169 \text{ kips}$$

$$= 381 \text{ kips}$$

The connection strength is:

$$\phi V_n = 176 \text{ kips} + 169 \text{ kips}$$

$$= 344 \text{ kips}$$

The effective strengths are recalculated:

$$V_{efBm} = \phi V_n - V_g - V_{BMF} \quad (18)$$
$$= 381 \text{ kips} - 10.0 \text{ kips} - 7.1 \text{ kips}$$
$$= 363 \text{ kips}$$

$$V_{efConn} = \phi R_n - V_g - V_{BMF} \quad (19)$$
$$= 344 \text{ kips} - 10.0 \text{ kips} - 7.1 \text{ kips}$$
$$= 327 \text{ kips}$$

With this reinforcement, the value of U_c is:

$$U_C = \frac{V_{efConn}}{V_{efBm}} = 0.900 \quad (20)$$

$$U_C V_{efB1,2} = 0.455(327 \text{ kips})$$
$$= 149 \text{ kips} > 135 \text{ kips} \quad \textbf{o.k.}$$

With this additional beam web reinforcement, the effective beam and effective connection capacities will be increased.

$$V_{efB1,2} = 0.455(363 \text{ kips})$$
$$= 166 \text{ kips} > 150 \text{ kips} \quad \textbf{o.k.}$$

Minimum Virtual Gusset Dimensions

The virtual gusset dimensions are determined based on the effective column and beam shear strengths calculated earlier.

$$r_{minCol} = \frac{e_c P}{V_{efC}} \quad (26)$$
$$= \frac{(7.25 \text{ in})(460 \text{ kips})}{240 \text{ kips}}$$
$$= 13.9 \text{ in.}$$

$$r_{minBm} = \frac{e_b P}{U_C V_{efB1,2}} \quad \text{(from Eq. 28)}$$
$$= \frac{(9.05 \text{ in})(460 \text{ kips})}{0.900\,(166 \text{ kips})}$$
$$= 27.9 \text{ in.}$$

$$r \geq \max(r_{minCol}, r_{minBm}) \quad (29)$$
$$\geq \max(13.9 \text{ in.}, 27.9 \text{ in.})$$
$$= 27.9 \text{ in.}$$

This value will be used for subsequent calculations. The corresponding virtual dimensions are:

$$\alpha = r \sin\theta - e_c \quad (10)$$
$$= (27.9 \text{ in.})(0.768) - 7.25 \text{ in.}$$
$$= 14.2 \text{ in.}$$

$$\beta = r \cos\theta - e_b \quad (11)$$
$$= (27.9 \text{ in.})(0.640) - 9.05 \text{ in.}$$
$$= 8.80 \text{ in.}$$

Gusset Forces and Member Shear Checks (at Connection)

The virtual gusset dimensions are used to determine the forces acting at the centroids of the virtual gusset interfaces with the beam and the column:

$$V_c = \frac{\beta}{r} P \tag{2}$$
$$= \left(\frac{8.80 \text{ in.}}{27.9 \text{ in.}}\right)(460 \text{ kips})$$
$$= 146 \text{ kips}$$

$$H_c = \frac{e_c}{r} P \tag{4}$$
$$= \left(\frac{7.25 \text{ in.}}{27.9 \text{ in.}}\right)(460 \text{ kips})$$
$$= 119 \text{ kips} < V_{efC} \quad \textbf{o.k.}$$

$$V_b = \frac{e_b}{r} P \tag{5}$$
$$= \left(\frac{9.05 \text{ in.}}{27.9 \text{ in.}}\right)(460 \text{ kips})$$
$$= 149 \text{ kips} < U_C V_{efB1,2} \quad \textbf{o.k.}$$

$$H_b = \frac{\alpha}{r} P \tag{6}$$
$$= \left(\frac{14.2 \text{ in.}}{27.9 \text{ in.}}\right)(460 \text{ kips})$$
$$= 234 \text{ kips}$$

Minimum Actual Gusset Dimensions and Member Shear Checks (at Mid-Length of Gusset)

The value of r_{minBm} controls; therefore, $r = r_{minBm}$ and $r > r_{minCol}$. The dimensions for $\overline{\alpha}$ and $\overline{\beta}$ are calculated as follows:

$$\overline{\beta} \geq \frac{\beta}{\left|\frac{V_{efC}}{H_c}\right| + \frac{1}{2}} \tag{33}$$
$$= \frac{8.80 \text{ in.}}{\left|\frac{240 \text{ kips}}{119 \text{ kips}}\right| + \frac{1}{2}}$$
$$= 3.50 \text{ in.}$$

$$\overline{\alpha} \geq \frac{\alpha}{\frac{1}{U_C} + \frac{1}{2}} \tag{40}$$
$$= \frac{14.2 \text{ in.}}{\frac{1}{0.900} + \frac{1}{2}}$$
$$= 8.81 \text{ in.}$$

The following values will be used:

$\overline{\beta} = 8$ in.

$\overline{\alpha} = 11$ in.

Both of these values exceed two-thirds of the corresponding virtual dimensions:

$$\frac{\bar{\beta}}{\beta} = \frac{8 \text{ in.}}{8.80 \text{ in.}}$$
$$= 0.909 > \tfrac{2}{3}$$

$$\frac{\bar{\alpha}}{\alpha} = \frac{11 \text{ in.}}{14.2 \text{ in.}}$$
$$= 0.775 > \tfrac{2}{3}$$

As such, the maximum member shear will be at sections C1 and B1 rather than C2 and B2. For completeness, the evaluation is shown next.

The moments due to the eccentricities between the actual dimensions and the virtual dimensions are:

$$M_c = H_c(\beta - \bar{\beta}) \tag{30}$$
$$= 119 \text{ kips}(8.80 \text{ in.} - 8 \text{ in.})$$
$$= 100 \text{ kip-in.}$$

$$M_b = V_b(\alpha - \bar{\alpha}) \tag{36}$$
$$= 149 \text{ kips}(14.2 \text{ in.} - 11 \text{ in.})$$
$$= 479 \text{ kip-in.}$$

Check column shear:

$$V_{mid} = \frac{H_c}{2} + \frac{M_c}{\bar{\beta}} \tag{31}$$
$$= \frac{119 \text{ kips}}{2} + \frac{100 \text{ kip-in.}}{8 \text{ in.}}$$
$$= 72.8 \text{ kips} < V_{efCol} \quad \textbf{o.k.}$$

Check beam shear:

$$V_{mid} = \frac{V_b}{2} + \frac{M_b}{\bar{\alpha}} \tag{37}$$
$$= \frac{149 \text{ kips}}{2} + \frac{479 \text{ kip-in.}}{11 \text{ in.}}$$
$$= 118 \text{ kips} < V_{efBm} \quad \textbf{o.k.}$$

Gusset Thickness

The gusset thickness is selected considering the combined forces on the gusset-to-column interface and the gusset-to-beam interface. Considering the column side, the minimum thickness is:

$$t_g \geq \frac{1}{\phi F_y 2\bar{\beta}} \sqrt{\left(\frac{V_c}{0.6}\right)^2 + \left(|H_c| + \frac{2|M_c|}{\bar{\beta}}\right)^2} \tag{44}$$
$$= \frac{1}{0.90(50 \text{ ksi})2(8 \text{ in.})} \sqrt{\left(\frac{146 \text{ kips}}{0.6}\right)^2 + \left(|119 \text{ kips}| + \frac{2|100 \text{ kip-in.}|}{8 \text{ in.}}\right)^2}$$
$$= 0.390 \text{ in.}$$

Considering the beam side, the minimum thickness is:

$$t_g \geq \frac{1}{\phi F_y 2\bar{\alpha}}\sqrt{\left(\frac{H_b}{0.6}\right)^2+\left(|V_b|+\frac{2|M_b|}{\bar{\alpha}}\right)^2} \tag{45}$$

$$= \frac{1}{0.90(50\text{ ksi})2(11\text{ in.})}\sqrt{\left(\frac{234\text{ kips}}{0.6}\right)^2+\left(|149\text{ kips}|+\frac{2|479\text{ kip-in.}|}{11\text{ in.}}\right)^2}$$

$$= 0.460\text{ in.}$$

A ½- in.-thick gusset is required, with overall dimensions of 23 in. wide by 17 in. high (providing extra length for weld termination). The gusset design is shown in Figure 12.

2. Redesign with Bypass Forces

The connection in this example is redesigned using the bypass method in order to avoid the need for the beam-web doubler. Values for V_{efB} and U_c correspond to the unreinforced condition.

The transfer factor λ is obtained from Equation 52:

$$\lambda \leq \frac{V_{efB}}{e_b \sin\theta P}\left[\bar{\alpha}\left(1+\frac{U_C}{2}\right)+U_C e_c\right] \tag{52}$$

$$= \frac{88.6\text{ kips}}{(9.05\text{ in.})0.768(460\text{ kips})}\left[(11\text{ in.})\left(1+\frac{0.814}{2}\right)+0.814(7.25\text{ in.})\right]$$

$$= 0.592$$

Bypass forces are calculated:

$$H_{cBP} = (1-\lambda)P\sin\theta \tag{48}$$

$$= (1-0.592)(460\text{ kips})0.768$$

$$= 144\text{ kips}$$

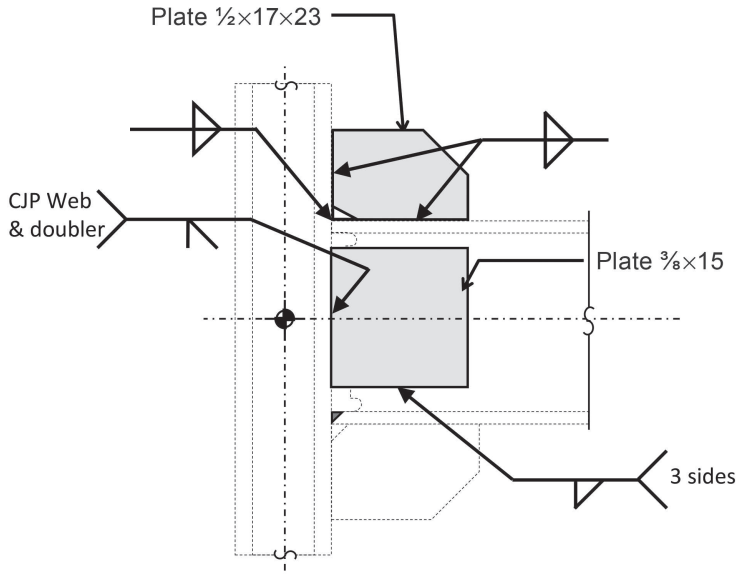

Fig. 12. Preliminary gusset design.

$$V_{cBP} = \frac{H_{cBP}}{\tan\theta} \tag{49}$$
$$= \frac{144 \text{ kips}}{1.20}$$
$$= 120 \text{ kips}$$

Minimum Virtual Gusset Dimensions

The virtual gusset dimensions are determined:

$$r_{minCol} = \frac{\lambda P e_c}{V_{efC} - H_{cBP}} \tag{53}$$
$$= \frac{(0.592)(460 \text{ kips})(7.25 \text{ in.})}{(240 \text{ kips}) - (144 \text{ kips})}$$
$$= 20.7 \text{ in.}$$

$$r_{minBm} = \frac{\lambda P e_b}{U_C V_{efB}} \tag{54}$$
$$= \frac{(0.592)(460 \text{ kips})(9.05 \text{ in.})}{0.814(88.6 \text{ kips})}$$
$$= 34.2 \text{ in.}$$

$$r \geq \max(r_{minCol}, r_{minBm}) \tag{29}$$
$$= \max(20.7 \text{ in.}, 34.2 \text{ in.})$$
$$= 34.2 \text{ in.}$$

This value will be used for subsequent calculations. The corresponding virtual dimensions

$$\alpha = r\sin\theta - e_c \tag{10}$$
$$= (34.2 \text{ in.})(0.768) - 7.25 \text{ in,}$$
$$= 19.0 \text{ in.}$$

$$\beta = r\cos\theta - e_b \tag{11}$$
$$= (34.2 \text{ in.})(0.640) - 9.05 \text{ in.}$$
$$= 12.8 \text{ in.}$$

Gusset Forces and Member Shear Checks (at Connection)

The virtual gusset dimensions are used to determine the forces acting at the centroids of the virtual gusset interfaces with the beam and the column:

$$\lambda V_c = \frac{\beta}{r}\lambda P \qquad \text{(from Eq. 2)}$$
$$= \left(\frac{12.8 \text{ in.}}{34.2 \text{ in.}}\right)(0.592)(460 \text{ kips})$$
$$= 102 \text{ kips}$$

$$\lambda H_c = \frac{e_c}{r}\lambda P \qquad \text{(from Eq. 4)}$$
$$= \left(\frac{7.25 \text{ in.}}{34.2 \text{ in.}}\right)(0.592)(460 \text{ kips})$$
$$= 57.8 \text{ kips}$$

$$\lambda V_b = \frac{e_b}{r}\lambda P \qquad \text{(from Eq. 5)}$$
$$= \left(\frac{9.05 \text{ in.}}{34.2 \text{ in.}}\right)(0.592)(460 \text{ kips})$$
$$= 72.1 \text{ kips}$$

$$\lambda H_b = \frac{\alpha}{r}\lambda P \qquad \text{(from Eq. 6)}$$
$$= \left(\frac{19.0 \text{ in.}}{34.2 \text{ in.}}\right)(0.592)(460 \text{ kips})$$
$$= 151 \text{ kips}$$

Determination of Total Forces and Member Shear Checks (at Connection)

The total vertical and horizontal forces are used in the determination of minimum required gusset dimensions. (Moments cannot be computed until the actual gusset dimensions are set.) The forces on the column edge of the gusset are:

$$H_{cTot} = \lambda H_c + H_{cBP} \qquad \text{(from Eq. 68)}$$
$$= 57.8 \text{ kips} + 144 \text{ kips}$$
$$= 202 \text{ kips} < V_{efC} \quad \textbf{o.k.}$$

$$V_{cTot} = \lambda V_c + V_{cBP} \qquad \text{(from Eq. 69)}$$
$$= 102 \text{ kips} + 120 \text{ kips}$$
$$= 222 \text{ kips}$$

The forces on the beam edge of the gusset are:

$$H_{bTot} = \lambda H_b \qquad \text{(from Eq. 72)}$$
$$= 151 \text{ kips}$$

$$V_{bTot} = \lambda V_b \qquad \text{(from Eq. 73)}$$
$$= 72.1 \text{ kips} < U_C V_{efB} \quad \textbf{o.k.}$$

Determination of Minimum Actual Gusset Dimensions

$$\bar{\beta} \geq \left(\beta - \frac{\alpha}{\tan\theta}\frac{H_{cBP}}{H_{cTot}}\right)\frac{1}{\left|\frac{V_{efC}}{H_{cTot}}\right| + \frac{1}{2}} \qquad (77)$$
$$= \frac{12.8 \text{ in.} - \left(\frac{19.0 \text{ in.}}{1.20}\right)\left(\frac{144 \text{ kips}}{202 \text{ kips}}\right)}{\left|\frac{240 \text{ kips}}{202 \text{ kips}}\right| + \frac{1}{2}}$$
$$= 0.900 \text{ in.}$$

$$\bar{\alpha} \geq \frac{\alpha}{\left|\frac{V_{efB}}{V_{bTot}}\right| + \frac{1}{2}} \tag{78}$$

$$= \frac{19.0 \text{ in.}}{\left|\frac{88.6 \text{ kips}}{72.1 \text{ kips}}\right| + \frac{1}{2}}$$

$$= 11.0 \text{ in.}$$

The following values will be used:

$\bar{\beta} = 8$ in.

$\bar{\alpha} = 11$ in.

Determination of Moments at Interfaces and Member Shear Checks (at Mid-Length of Gusset)

The moments on the column edge of the gusset are:

$$\lambda M_c = \lambda H_c (\beta - \bar{\beta}) \quad \text{(from Eq. 30)}$$

$$= (57.8 \text{ kips})(12.8 \text{ in.} - 8 \text{ in.})$$

$$= 279 \text{ kip-in.}$$

$$M_{cBP} = H_{cBP}(e_b + \bar{\beta}) - V_{cBP} e_c \quad \text{(50)}$$

$$= (144 \text{ kips})(9.05 \text{ in.} + 8 \text{ in.}) - (120 \text{ kips})(7.25 \text{ in.})$$

$$= 1{,}590 \text{ kip-in.}$$

$$M_{cTot} = \lambda M_c - M_{cBP} \quad \text{(from Eq. 70)}$$

$$= 279 \text{ kip-in.} - 1{,}590 \text{ kip-in.}$$

$$= -1{,}310 \text{ kip-in.}$$

The moments on the beam edge of the gusset are:

$$M_{bTot} = \lambda M_b \quad \text{(from Eq. 74)}$$

$$= \lambda V_b (\alpha - \bar{\alpha}) \quad \text{(from Eq. 36)}$$

$$= (72.1 \text{ kips})(19.0 \text{ in.} - 11 \text{ in.})$$

$$= 577 \text{ kip-in.}$$

Check column shear:

$$V_{mid} = \frac{H_{cTot}}{2} + \frac{M_{cTot}}{\bar{\beta}} \quad \text{(from Eq. 31)}$$

$$= \frac{202 \text{ kips}}{2} + \frac{-1{,}310 \text{ kip-in.}}{8 \text{ in.}}$$

$$= 62.6 \text{ kips} < V_{efC} \quad \textbf{o.k.}$$

Check beam shear:

$$V_{mid} = \frac{V_{bTot}}{2} + \frac{M_{bTot}}{\bar{\alpha}} \quad \text{(from Eq. 37)}$$

$$= \frac{72.1 \text{ kips}}{2} + \frac{577 \text{ kip-in.}}{11 \text{ in.}}$$

$$= 88.5 \text{ kips} < V_{efB} \quad \textbf{o.k.}$$

Note that Equations 31 and 37 are modified to utilize total forces (H_{cTot}, etc.).

Determination of Required Gusset Thickness

Considering the column side, the minimum thickness is:

$$t_g \geq \frac{1}{\phi F_y 2\bar{\beta}} \sqrt{\left(\frac{V_{cTot}}{0.6}\right)^2 + \left(|H_{cTot}| + \frac{2|M_{cTot}|}{\bar{\beta}}\right)^2} \quad \text{(from Eq. 44)}$$

$$= \frac{1}{0.90(50 \text{ ksi})2(8 \text{ in.})} \sqrt{\left(\frac{222 \text{ kips}}{0.6}\right)^2 + \left(|202 \text{ kips}| + \frac{2|-1{,}310 \text{ kip-in.}|}{8 \text{ in.}}\right)^2}$$

$$= 0.897 \text{ in.}$$

Considering the beam side, the minimum thickness is:

$$t_g \geq \frac{1}{\phi F_y 2\bar{\alpha}} \sqrt{\left(\frac{H_{bTot}}{0.6}\right)^2 + \left(|V_{bTot}| + \frac{2|M_{bTot}|}{\bar{\alpha}}\right)^2} \quad \text{(from Eq. 45)}$$

$$= \frac{1}{0.90(50 \text{ ksi})2(11 \text{ in.})} \sqrt{\left(\frac{151 \text{ kips}}{0.6}\right)^2 + \left(|72.11 \text{ kips}| + \frac{2|577 \text{ kip-in.}|}{11 \text{ in.}}\right)^2}$$

$$= 0.311 \text{ in.}$$

The minimum thickness is taken as the maximum of Equations 44 and 45. Thus, a plate 1 in. × 17 in. high × 23 in. wide can be used. The web doubler in the beam is eliminated (as are the CJP welds of the doubler and beam web to the column) at the cost of a thicker gusset (and larger gusset-to-column welds). Alternatively, if a thinner gusset is desired, the dimension $\bar{\beta}$ could be increased beyond the original target value. Fillet welds are based on the strength of the gusset plate. The gusset design is shown in Figure 13.

3. Design Considering Haunch Force (with Bypass Method)

In this example, a design of the connection will be performed considering requirements for buckling restrained braced frames. (As discussed earlier, inelastic demands on the gusset plate due to brace buckling, as would be expected for the seismic response of other braced-frame systems, are not addressed in this design method.) The example considers seismic forces, but the method illustrated is applicable to design for wind loads as well.

For seismic design, the beam moments and shears considered correspond to the flexural yielding of the beam because the frame is expected to undergo large displacements. While the beam end moment could be resisted by the beam-to-column connection (as it was for the previous examples for wind load), there can be significant economy in utilizing the gussets as haunches and eliminating beam-flange-to-column-flange welds. In this example, the haunch method is used in conjunction with the bypass method utilized in the previous example.

The designer should consider the range of possible beam-end moments that could coincide with maximum brace forces (and vice versa), as the drift ranges for the beam and for the braces are likely to be substantially different. For this example, the range of moments is based on the beam expected moment strength in one direction (positive M_f) and zero in the opposite direction. The authors do not intend to imply that this range is adequate for all (or even most) conditions. Determination of the appropriate combinations of beam moment and brace axial forces for systems subject to inelastic drift requires further study and is outside of the scope of this paper.

Values are presented in pairs in braces ("{}"), with the first value corresponding to the inclusion of forces (both shears and moments) corresponding to moment-frame action (condition 1) and the second value without (condition 2). A separate final check is performed using only the haunch forces from beam moment with brace forces taken as zero.

Given the difference in the drift that results in yield of the braces and that corresponding to yield of the beam, it is possible for cyclic inelastic drift to result in a condition in which the value of beam moment is negative and the forces λH_c and H_{cH} (Eq. 68) are additive. Consideration of such a condition is beyond the scope of this study.

The haunch force is based on an apportionment factor $\rho = 0.0$.

$$M_f = \{7770,0\} \text{ kip-in.}$$

$$M_H = (1-\rho)\frac{M_{fi}}{2} \tag{59}$$
$$= (1-0)\frac{\{7770, 0\} \text{ kip-in.}}{2}$$
$$= \{3880,0\} \text{ kip-in.}$$

$$V_{col} = \{108,0\} \text{ kips}$$

$$V_{BMF} = \{44.9, 0\} \text{ kips}$$

$$V_{efCol} = \phi V_n - V_{col} \tag{17}$$
$$= 257 \text{ kips} - \{108, 0\} \text{ kips}$$
$$= \{149, 257\} \text{ kips}$$

$$V_{efBm} = (\phi V_n - V_g - V_{BMF})\frac{P_{1,2}\cos\theta}{P_{1,1}\cos\theta + P_{1,2}\cos\theta} \quad \text{(from Eqs. 18, 25)}$$
$$= (212 \text{ kips} - 10.0 \text{ kips} - \{44.9, 0\} \text{kips})\left(\frac{295 \text{ kips}}{352 \text{ kips} + 295 \text{ kips}}\right)$$
$$= \{71.4, 91.9\} \text{ kips}$$

$$V_{efConn} = (\phi R_n - V_g - V_{BmF})\frac{P_{1,2}\cos\theta}{P_{1,1}\cos\theta + P_{1,2}\cos\theta} \quad \text{(from Eqs. 19, 25)}$$
$$= (176 \text{ kips} - 10.0 \text{ kips} - \{44.9, 0\} \text{kips})\left(\frac{295 \text{ kips}}{352 \text{ kips} + 295 \text{ kips}}\right)$$
$$= \{54.9, 91.9\} \text{ kips}$$

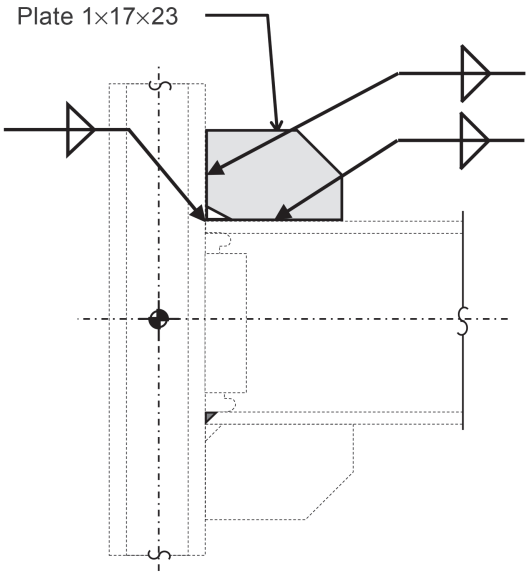

Fig. 13. Gusset design with bypass forces.

$$U_C = \frac{V_{efConn}}{V_{efBm}} \tag{20}$$
$$= \left\{\frac{57.5 \text{ kips}}{74.0 \text{ kips}}, \frac{75.4 \text{ kips}}{91.9 \text{ kips}}\right\}$$
$$= \{0.769, 0.820\}$$

The apportionment factor λ is determined for condition 2 ($M_f = 0$) using the corresponding effective beam and connection strength.

$$\lambda \le \frac{V_{efB}}{e_b \sin\theta P}\left[\bar{\alpha}\left(1+\frac{U_C}{2}\right)+e_c U_C\right] \tag{52}$$
$$= \frac{(91.9 \text{ kips})}{(9.05 \text{ in.})(0.768)(460 \text{ kips})}\left[(11 \text{ in.})\left(1+\frac{0.820}{2}\right)+(0.820)(7.25 \text{ in.})\right]$$
$$= 0.617$$

This apportionment factor based on condition 2 will be used for both conditions 1 and 2.

$$H_{cBP} = (1-\lambda)P\sin\theta \tag{48}$$
$$= (1-0.617)(460 \text{ kips})0.768$$
$$= 135 \text{ kips}$$

Determination of Minimum Virtual Gusset Dimensions

The minimum required gusset dimension, *r*, is determined for each case:

$$r_{minCol}^2\left[(V_{efC}-H_{cBP})\cos\theta\right]+r_{minCol}\left[(V_{efC}-H_{cBP})(e_c-e_b)+(1-\rho)\frac{M_f}{2}-\lambda P e_c\cos\theta\right]+\left[\lambda P e_c(e_b-e_c)\right]\ge 0 \tag{75}$$
$$r_{minCol}^2\left[(\{163, 257\}-135)0.640\right]$$
$$+r_{minCol}\left[(\{163, 257\} \text{ kips}-135 \text{ kips})(7.25 \text{ in.}-9.05 \text{ in.})+\frac{\{7765, 0\} \text{ kip-in.}}{2}-0.617(460 \text{ kips})(7.25 \text{ in.})(0.640)\right]$$
$$+\left[0.617(460 \text{ kips})(7.25 \text{ in.})(9.05 \text{ in.}-7.25 \text{ in.})\right]\ge 0$$

This is solved by the quadratic formula:

$$r_{minCol} = \{-1.50, 17.0\} \text{ in.}$$

$$r_{minBm}^2\left[\sin\theta U_c V_{efBm}\right]+r_{minBm}\left[M_H-e_c U_c V_{efBm}-PFe_b\sin\theta\right]+\left[\lambda P e_b e_c-M_H\frac{e_b}{\cos\theta}\right]\ge 0 \tag{76}$$
$$r_{minBm}^2\left[0.768\{54.9, 91.9\} \text{ kips}\right]$$
$$+r_{minBm}\left[\{3880, 0\} \text{ kip-in.}-(7.25 \text{ in.})\{54.9, 91.9\} \text{ kips}-0.617(460 \text{ kips})(9.05 \text{ in.})0.768\right]$$
$$+\left[0.617(460 \text{ kips})(9.05 \text{ in.})(7.25 \text{ in.})-\{3880, 0\} \text{ kip-in.}\left(\frac{9.05 \text{ in.}}{0.640}\right)\right]\ge 0$$

This is solved by the quadratic formula:

$$r_{minBm} = \{16.4, 34.1\} \text{ in.}$$

$$r \ge \max(r_{minCol}, r_{minBm}) \tag{29}$$
$$= \{\max(-1.50, 16.4), \max(17.0, 34.1)\} \text{ in.}$$
$$= \{16.4, 34.1\} \text{ in.}$$

As discussed in the derivation of Equations 75 and 76, for cases in which the member shear is not a governing consideration, selection of a higher value of the virtual dimension, *r*, could result in lower required gusset thickness. By trial and error, a value of the virtual dimension $r = 18.9$ in. was found to optimize the required gusset thickness for condition 1. (The same gusset-edge forces could also be obtained with $\lambda = 1.0$ and $r = 35.2$.) However, because this example also considers the zero-moment condition 2, no reduction results from such optimization, and such trial-and-error methods are generally not beneficial.

$$\alpha = r\sin\theta - e_c \tag{10}$$
$$= \{18.9, 34.1\}\text{ in.}(0.768) - 7.25\text{ in.}$$
$$= \{7.20, 18.9\}\text{ in.}$$

$$\beta = r\cos\theta - e_b \tag{11}$$
$$= \{18.9, 34.1\}\text{ in.}(0.640) - 9.05\text{ in.}$$
$$= \{3.00, 12.8\}\text{ in.}$$

Determination of Forces at Interfaces

The minimum actual gusset dimensions $\overline{\beta}$ and $\overline{\alpha}$ are functions of the UFM, bypass, and haunch forces:

$$\lambda V_c = \lambda\frac{\beta}{r}P \quad \text{(from Eq. 2)}$$
$$= 0.617\frac{\{3.00, 12.8\}\text{ in.}}{\{18.9, 34.1\}\text{ in.}}(460\text{ kips})$$
$$= \{45.5, 106\}\text{ kips}$$

$$\lambda H_c = \lambda\frac{e_c}{r}P \quad \text{(from Eq. 4)}$$
$$= 0.617\frac{7.25\text{ in.}}{\{18.9, 34.1\}\text{ in.}}(460\text{ kips})$$
$$= \{109, 60.4\}\text{ kips}$$

$$\lambda V_b = \lambda\frac{e_b}{r}P \quad \text{(from Eq. 5)}$$
$$= 0.617\frac{9.05\text{ in.}}{\{18.9, 34.1\}\text{ in.}}(460\text{ kips})$$
$$= \{136, 75.4\}\text{ kips}$$

$$\lambda H_b = \lambda\frac{\alpha}{r}P \quad \text{(from Eq. 6)}$$
$$= 0.617\frac{\{7.20, 18.9\}\text{ in.}}{\{18.9, 34.1\}\text{ in.}}(460\text{ kips})$$
$$= \{109, 158\}\text{ kips}$$

$$V_{cBP} = \frac{H_{cBP}}{\tan\theta} \tag{49}$$
$$= \frac{135\text{ kips}}{1.20}$$
$$= 113\text{ kips}$$

$$H_{cH} = H_{bH} \quad \text{(from Eqs. 62, 63)}$$
$$= \frac{M_H}{e_b + \beta}$$
$$= \frac{\{3880, 0\} \text{ kip-in.}}{9.05 \text{ in.} + \{3.00, 12.8\} \text{ in.}}$$
$$= \{322, 0\} \text{ kips}$$

$$V_{bH} = V_{cH} \quad (64)$$
$$= H_{cH} \frac{\beta}{\alpha}$$
$$= \{322, 0\} \text{ kips} \frac{\{3.00, 12.8\} \text{ in.}}{\{7.20, 18.9\} \text{ in.}}$$
$$= \{134, 0\} \text{ kips}$$

Determination of Total Forces and Member Shear Checks (at Connection)

The total vertical and horizontal forces are used in the determination of minimum required gusset dimensions. (Moments cannot be computed until the actual gusset dimensions are set.) The forces on the column edge of the gusset are:

$$H_{cTot} = \lambda H_c + H_{cBP} - H_{cH} \quad (68)$$
$$= \{109, 60.4\} \text{ kips} + 135 \text{ kips} - \{322, 0\} \text{ kips}$$
$$= \{-77.1, 196\} \text{ kips} < V_{efC} = V_{efCol} \quad \textbf{o.k.}$$

$$V_{cTot} = \lambda V_c + V_{cBP} + V_{cH} \quad (69)$$
$$= \{45.5, 106\} \text{ kips} + 113 \text{ kips} - \{134, 0\} \text{ kips}$$
$$= \{293, 219\} \text{ kips}$$

The forces on the beam edge of the gusset are:

$$H_{bTot} = \lambda H_b + H_{bH} \quad (72)$$
$$= \{109, 158\} \text{ kips} + \{322, 0\} \text{ kips}$$
$$= \{431, 158\} \text{ kips}$$

$$V_{bTot} = \lambda V_b - V_{bH} \quad (73)$$
$$= \{136, 75.4\} \text{ kips} - \{134, 0\} \text{ kips}$$
$$= \{1.90, 75.4\} \text{ kips} < U_C V_{efB} \quad \textbf{o.k.}$$

Determination of Minimum Actual Gusset Dimensions

$$\overline{\beta} \geq \frac{\beta H_{cTot} - H_{cBP}\left(\beta + e_b - \frac{e_c}{\tan\theta}\right)}{V_{efC} + \frac{1}{2} H_{cTot}} \quad (77)$$
$$= \frac{\left(\{3.00, 12.8\} \text{in.}\right)\left(\{-77.1, 196\} \text{kips}\right) - 135 \text{ kips}\left(\{3.00, 12.8\} \text{in.} + 9.05 \text{ in.} - \frac{7.25 \text{ in.}}{1.20}\right)}{\{149, 257\} \text{ kips} + \frac{1}{2}\{-77.1, 196\} \text{ kips}}$$
$$= \{5.60, 1.00\} \text{ in.}$$

$$\bar{\alpha} \geq \frac{\alpha}{\left|\frac{V_{efB}}{V_{bTot}}\right| + \frac{1}{2}} \tag{78}$$

$$= \frac{\{7.20, 18.9\}\text{ in.}}{\left|\frac{\{71.4, 91.9\}\text{ kips}}{\{1.90, 75.4\}\text{ kips}}\right| + \frac{1}{2}}$$

$$= \{0.200,\ 11.0\}\text{ in.}$$

The following values will be used for the actual gusset:

$\bar{\beta} = 8$ in.

$\bar{\alpha} = 11$ in.

It should be noted that condition 2 (which does not include the beam moment) is the governing condition. This is because the beam shear is the governing consideration in selecting the gusset size, and beam shear induced by the haunch forces counteracts that due to the brace force. This highlights the need to consider the minimum value of the beam moment in design. It also shows that in some cases the gussets can provide flexural resistance at essentially no cost.

Determination of Moments at Interfaces and Member Shear Checks (at Mid-Length of Gusset)

The moments on the column edge of the gusset are:

$$\lambda M_c = \lambda H_c(\beta - \bar{\beta}) \quad \text{(from Eq. 30)}$$

$$= \{109, 60.4\}\text{ kips}(\{3.00, 12.8\}\text{ in.} - 8\text{ in.})$$

$$= \{-543, 288\}\text{ kip-in.}$$

$$M_{cBP} = H_{cBP}(e_b + \bar{\beta}) - V_{cBP}e_c \tag{50}$$

$$= 135\text{ kips}(7.25\text{ in.} + 8\text{ in.}) - 113\text{ kips}(7.25\text{ in.})$$

$$= \{1490, 1490\}\text{ kip-in.}$$

$$M_{cH} = (\beta - \bar{\beta})H_{cH} \tag{65}$$

$$= (\{3.00, 12.8\}\text{ in.} - 8\text{ in.})\{32.6, 0\}\text{ kips}$$

$$= \{-1600, 0\}\text{ kip-in.}$$

$$M_{cTot} = \lambda M_c - M_{cBP} - M_{cH} \tag{70}$$

$$= \{-543, 288\}\text{ kip-in.} - \{1490, 1490\}\text{ kip-in.} - \{-1600, 0\}\text{ kip-in.}$$

$$= \{-433,\ -1200\}\text{ kip-in.}$$

The moments on the beam edge of the gusset are:

$$\lambda M_b = \lambda V_b(\alpha - \bar{\alpha}) \quad \text{(from Eq. 36)}$$

$$= \{136, 75.4\}\text{ kips}(\{7.2, 18.9\}\text{ in.} - 11\text{ in.})$$

$$= \{-512, 597\}\text{ kip-in.}$$

$$M_{bH} = (\alpha - \bar{\alpha})V_{bH} \tag{66}$$

$$= (\{7.20, 18.9\}\text{ in.} - 11\text{ in.})\{134, 0\}\text{ kips}$$

$$= \{-505, 0\}\text{ kip-in.}$$

$$M_{bTot} = \lambda M_b - M_{bH} \tag{74}$$

$$= \{-512, 597\}\text{ kip-in.} - \{-505, 0\}\text{ kip-in.}$$

$$= \{-7.00, 597\}\text{ kip-in.}$$

Check column shear:

$$V_{mid} = \frac{H_{cTot}}{2} + \frac{M_{cTot}}{\bar{\beta}} \quad \text{(from Eq. 31)}$$
$$= \frac{\{-77.1, 196\}\text{ kips}}{2} + \frac{\{-433, -1200\}\text{ kip-in.}}{8\text{ in.}}$$
$$= \{-92.6, -52.4\}\text{ kips} < V_{efC} \quad \textbf{o.k.}$$

Check beam shear:

$$V_{mid} = \frac{V_{bTot}}{2} + \frac{M_{bTot}}{\bar{\alpha}} \quad \text{(from Eq. 37)}$$
$$= \frac{\{1.90, 75.4\}\text{ kips}}{2} + \frac{\{-7.00, 597\}\text{ kip-in.}}{11\text{ in.}}$$
$$= \{0.300, 91.9\}\text{ kips} < V_{efB} \quad \textbf{o.k.}$$

Determination of Required Gusset Thickness

Considering the column side, the minimum thickness is:

$$t_g \geq \frac{1}{\phi F_y 2\bar{\beta}}\sqrt{\left(\frac{V_{cTot}}{0.6}\right)^2 + \left(|H_{cTot}| + \frac{2|M_{cTot}|}{\bar{\beta}}\right)^2} \quad \text{(from Eq. 44)}$$
$$= \frac{1}{0.90(50\text{ ksi})2(8\text{ in.})}\sqrt{\left(\frac{\{293, 219\}\text{ kips}}{0.6}\right)^2 + \left(|\{-77.1, 196\}\text{ kips}| + \frac{2|\{-433, -1200\}\text{ kip-in.}|}{8\text{ in.}}\right)^2}$$
$$= \{0.725, 0.856\}\text{ in.}$$

Considering the beam side, the minimum thickness is:

$$t_g \geq \frac{1}{\phi F_y 2\bar{\alpha}}\sqrt{\left(\frac{H_{bTot}}{0.6}\right)^2 + \left(|V_{bTot}| + \frac{2|M_{bTot}|}{\bar{\alpha}}\right)^2} \quad \text{(from Eq. 45)}$$
$$= \frac{1}{0.90(50\text{ ksi})2(11\text{ in.})}\sqrt{\left(\frac{\{431, 158\}\text{ kips}}{0.6}\right)^2 + \left(|\{1.90, 75.4\}\text{ kips}| + \frac{2|\{-7.00, 597\}\text{ kip-in.}|}{11\text{ in.}}\right)^2}$$
$$= \{0.725, 0.324\}\text{ in.}$$

The minimum thickness is taken as the maximum of Equations 44 and 45.

Evaluation of Connection for Moment Only

As discussed earlier, the connection should have sufficient strength to resist the required moment without the offsetting effects of the brace forces.

The effective column shear strength in this case is increased due to the column shear (similar to column shear in a moment frame being in the opposite direction from the beam flange force and thus reducing the panel-zone shear demand).

$$V_{efCol} = \phi V_n + V_{col}$$
$$= 257\text{ kips} + 108\text{ kips}$$
$$= 365\text{ kips}$$

Similarly, the shear in the beam due to moment-frame behavior, V_{BMF}, is in the opposite direction from the shear induced by the haunch force, effectively increasing the effective beam shear:

$$V_{efBm} = (\phi V_n - V_g + V_{BMF}) \frac{P_{1,2} \cos\theta}{P_{1,1} \cos\theta + P_{1,2} \cos\theta} \quad \text{(from Eqs. 18, 25)}$$

$$= (212 \text{ kips} - 10.0 \text{ kips} + 44.9 \text{ kips})(0.455)$$

$$= 112 \text{ kips}$$

The forces on the column edge of the gusset are:

$$H_{cTot} = H_{cH} \quad \text{(from Eq. 68)}$$

$$= 322 \text{ kips} < V_{efCol} \quad \textbf{o.k.}$$

$$V_{cTot} = V_{cH} \quad \text{(from Eq. 69)}$$

$$= 134 \text{ kips}$$

The forces on the beam edge of the gusset are:

$$H_{bTot} = H_{bH} \quad \text{(from Eq. 72)}$$

$$= 322 \text{ kips}$$

$$V_{bTot} = V_{bH} \quad \text{(from Eq. 73)}$$

$$= 134 \text{ kips}$$

Because $V_{bTot} > U_C V_{efB}$, reinforcement is required.

The moments on the column edge of the gusset are:

$$M_{cTot} = M_{cH} \quad \text{(from Eq. 70)}$$

$$= 1{,}600 \text{ kip-in.}$$

The moments on the beam edge of the gusset are:

$$M_{bTot} = M_{bH} \quad \text{(from Eq. 74)}$$

$$= 505 \text{ kip-in.}$$

Check column shear:

$$V_{mid} = \frac{H_{cTot}}{2} + \frac{M_{cTot}}{\bar{\beta}} \quad \text{(from Eq. 31)}$$

$$= \frac{322 \text{ kips}}{2} + \frac{1{,}600 \text{ kip-in.}}{8 \text{ in.}}$$

$$= 361 \text{ kips} < V_{efC} \quad \textbf{o.k.}$$

Check beam shear:

$$V_{mid} = \frac{V_{bTot}}{2} + \frac{M_{bTot}}{\bar{\alpha}} \quad \text{(from Eq. 37)}$$

$$= \frac{134 \text{ kips}}{2} + \frac{505 \text{ kip-in.}}{11 \text{ in.}}$$

$$= 113 \text{ kips} \approx V_{efB} \quad \textbf{o.k.}$$

Check gusset on column edge:

$$t_g \geq \frac{1}{\phi F_y 2\bar{\beta}}\sqrt{\left(\frac{V_{cTot}}{0.6}\right)^2+\left(|H_{cTot}|+\frac{2|M_{cTot}|}{\bar{\beta}}\right)^2} \quad \text{(from Eq. 44)}$$

$$= \frac{1}{0.90(50\text{ ksi})2(8\text{ in.})}\sqrt{\left(\frac{134\text{ kips}}{0.6}\right)^2+\left(|322\text{ kips}|+\frac{2|1{,}600\text{ kip-in.}|}{8\text{ in.}}\right)^2}$$

$$= 1.05\text{ in.}$$

Considering the beam side, the minimum thickness is:

$$t_g \geq \frac{1}{\phi F_y 2\bar{\alpha}}\sqrt{\left(\frac{H_{bTot}}{0.6}\right)^2+\left(|V_{bTot}|+\frac{2|M_{bTot}|}{\bar{\alpha}}\right)^2} \quad \text{(from Eq. 45)}$$

$$= \frac{1}{0.90(50\text{ ksi})2(11\text{ in.})}\sqrt{\left(\frac{322\text{ kips}}{0.6}\right)^2+\left(|134\text{ kips}|+\frac{2|505\text{ kip-in.}|}{11\text{ in.}}\right)^2}$$

$$= 0.588\text{ in.}$$

The use of the gusset plates as haunches, in the absence of the offsetting brace forces, requires increasing the gusset thickness and providing modest beam reinforcement. Alternatively, the gusset could be enlarged. For wind loading, it may be possible to rely on the offsetting effects of the beam moment and brace forces to be in phase; for seismic loading consideration of out-of-phase behavior is prudent.

The design is shown in Figure 14. Note that beam-flange-to-column-flange welds are not required due to the entire beam-end moment being resisted by the gussets. As with the previous example, fillet welds are based on the strength of the gusset plate.

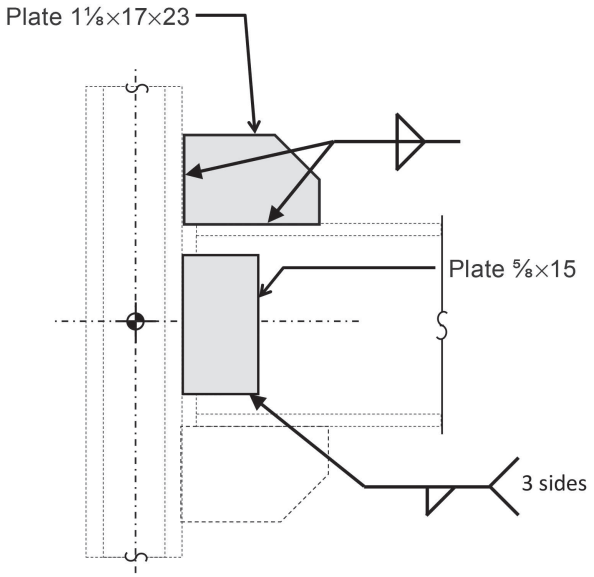

Fig. 14. Gusset design considering haunch forces.

VALIDATION

In order to demonstrate that the design methods presented in this study produce adequate designs, finite element analyses were conducted on two models representing the design in Example 3. The analyses corresponded to both the condition with the full expected beam moment (condition 1) and the condition with zero moment (condition 2), which governed the design.

The two analysis models were constructed using Abaqus software. Flanges, webs, and gussets were meshed with shell elements in the connection region. Columns were meshed from the connection region to the column mid-height. Beams were meshed from the connection region to the beam quarter-length for condition 1. Frame members were used for columns and beams outside these regions. The models use an expected material strength of 55 ksi for all elements, moderately higher than the design strength employed in the design model (ϕF_y = 45 ksi). Consistent with the design, beam flanges are not connected to the column flange and are separated by a small gap. A web-connection plate is joined to the beam web with a vertical line of tie elements and two 2-in. returns.

The analysis for condition 1 is displacement controlled, with the displacements at the two levels constrained to a proportion of 2:1. Brace axial post-elastic stiffness in the model is tuned such that the brace axial forces used in design from Table 2 develop at a drift of 2.46%, which is the drift that results in the design moment from beam plastic hinging from Table 3. Thus, brace and beam forces transmitted to the connection area closely match those used in Example 3.

For condition 2, no lateral drift is imposed, and the analysis is force controlled. The design forces (brace axial forces from Table 2 and beam shear from Table 3) are imposed on a constrained section of the beam at the connection boundary. Figure 15 shows diagrams of the models for conditions 1 and 2.

Figure 16 shows the von Mises stresses and equivalent plastic strains in the connection region, with gusset interface forces determined by stress integration. The analysis for condition 1 shows the formation of a beam plastic hinge close to the edge of the gusset. With the exception of the plastic hinge region, the stress in the beam web is low, consistent with the low forces indicated at section B2 in the design calculations (Equation 37, which indicates 1.2 kips of beam shear from the top gusset).

The analysis confirms that the connection can resist the design forces, including the beam plastic-hinge moment.

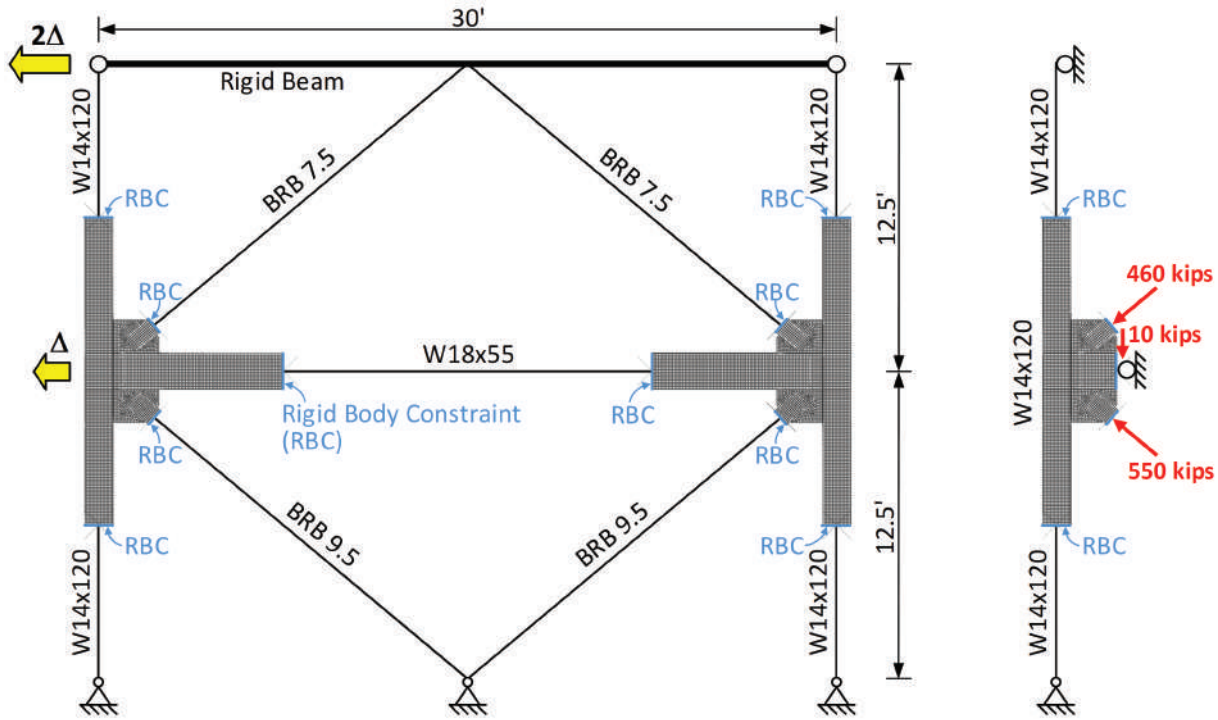

Fig. 15. Diagrams of finite element models for condition 1 (a) and condition 2 (b).

This supports the validity of the haunch method, which utilizes the gussets to transmit the beam moment to the column (rather than beam flange welds). As the plastic strain is limited to the beam plastic hinge, the analysis confirms that the design resistance can be achieved without excessive ductility demand in any part of the gusset connection.

While an accurate design model is not required by the lower-bound theorem, the forces at the interfaces are reasonably close to those in the design example: the difference between the design and analysis model values is small compared to the vertical or horizontal component of the brace force, as shown in Tables 5 and 6.

Table 5 shows that the apportionment of vertical and horizontal forces between the beam and column is roughly consistent between the design and the analysis. Table 6 includes normal, shear, and flexural force at the gusset edge at the column and at the gusset edge at the beam, for both the example calculation and from the finite element analysis. For both, stresses are calculated using the conventional plastic method utilizing the plastic section modulus and computing a vector sum of normal and shear stress. (Stresses listed for the finite element analysis are computed from total forces on the gusset edges; the stresses are not those directly reported from the analysis. These stresses are only presented as a means of quantifying the combined effect of shear, normal, and flexural force at the gusset edge.) The comparison shows that design gusset-edge stresses so calculated also correspond roughly. Nevertheless, the difference is large enough in the case of the vertical force to the beam to warrant caution in reliance on small values obtained from the difference of large forces, and the peak design stress is below the peak stress shown in Figure 16, suggesting that providing for the full gusset yield strength is prudent. Note that the edge forces from the finite element analysis are computed in the deformed condition, and thus are slightly out of alignment with the design calculations.

It should be noted, however, that the values determined by the haunch design method are moderately influenced by some of the simplifying assumptions. First, the value of the virtual dimension, r, was taken as the optimum value using trial and error; the method allows for other values to be used. Second, the haunch forces are set to the same locations as the UFM forces, as shown in Figure 10. Third, the apportionment factor, λ, employed for condition 1 is for convenience set equal to that for condition 2. Changes to any of these assumptions would result in somewhat different design forces, and possibly greater difference between calculated and analyzed values.

In contrast to condition 1, the finite element analysis of condition 2 (Figure 17) shows high beam shear in the connection region with substantial yielding both in the beam web (section B2) and in the connection plate (approximately at section B1). In the design method (with the virtual

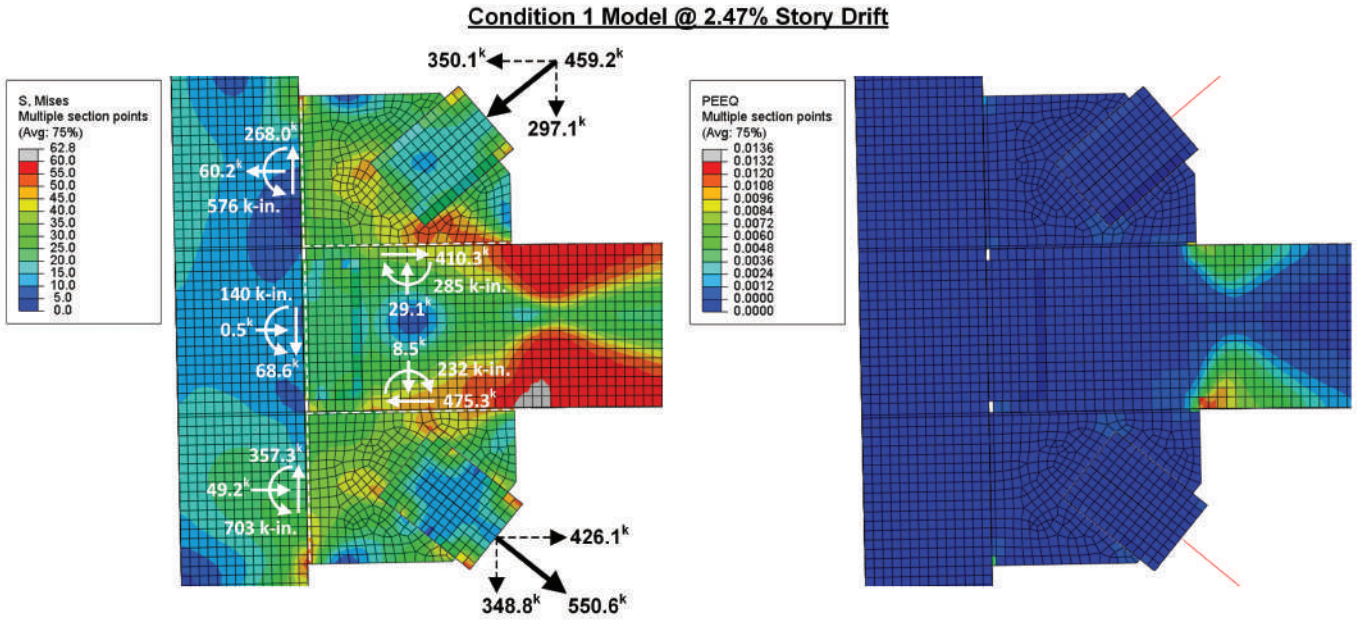

(a) Von Mises stress contour *(b) Equivalent plastic stain contour*

Fig. 16. Finite element analysis results of Example 3, condition 1.

Table 5. Comparison of Analysis and Design Vertical and Horizontal Forces for Condition 1					
Horizontal Forces	H_{cTot} (kips)	H_{bTot} (kips)	Sum (kips)	% Column	% Beam
Example 3 calculation	–77.1	431	353	–22%	122%
Finite element analysis	–60.2	410	350	–17%	117%
Vertical Forces	V_{cTot} (kips)	V_{bTot} (kips)	Sum (kips)	% Column	% Beam
Example 3 calculation	292	2.70	295	99%	1%
Finite element analysis	268	29.1	297	90%	10%

Table 6. Comparison of Analysis and Design Gusset-Edge Forces for Condition 1							
Forces at Column	H_{cTot} (kips)	V_{cTot} (kips)	M_{cTot} (kip-in.)	Normal Stress (ksi)	Shear Stress (ksi)	Resultant Stress (ksi)	Angle (deg)
Example 3 calculation	–77.1	292	–459	13.7	20.8	24.9	33.3
Finite element analysis	–60.2	268	–576				
Stress calculated from finite element analysis forces				14.6	19.1	24.1	37.3
Forces at Beam	V_{bTot} (kips)	H_{bTot} (kips)	M_{bot} (kip-in.)	Normal Stress (ksi)	Shear Stress (ksi)	Resultant Stress (ksi)	Angle (deg)
Example 3 calculation	2.70	431	0.0	0.100	22.4	22.4	0.40
Finite element analysis	29.1	410	–285				
Stress calculated from finite element analysis forces				4.20	21.3	21.7	11.2

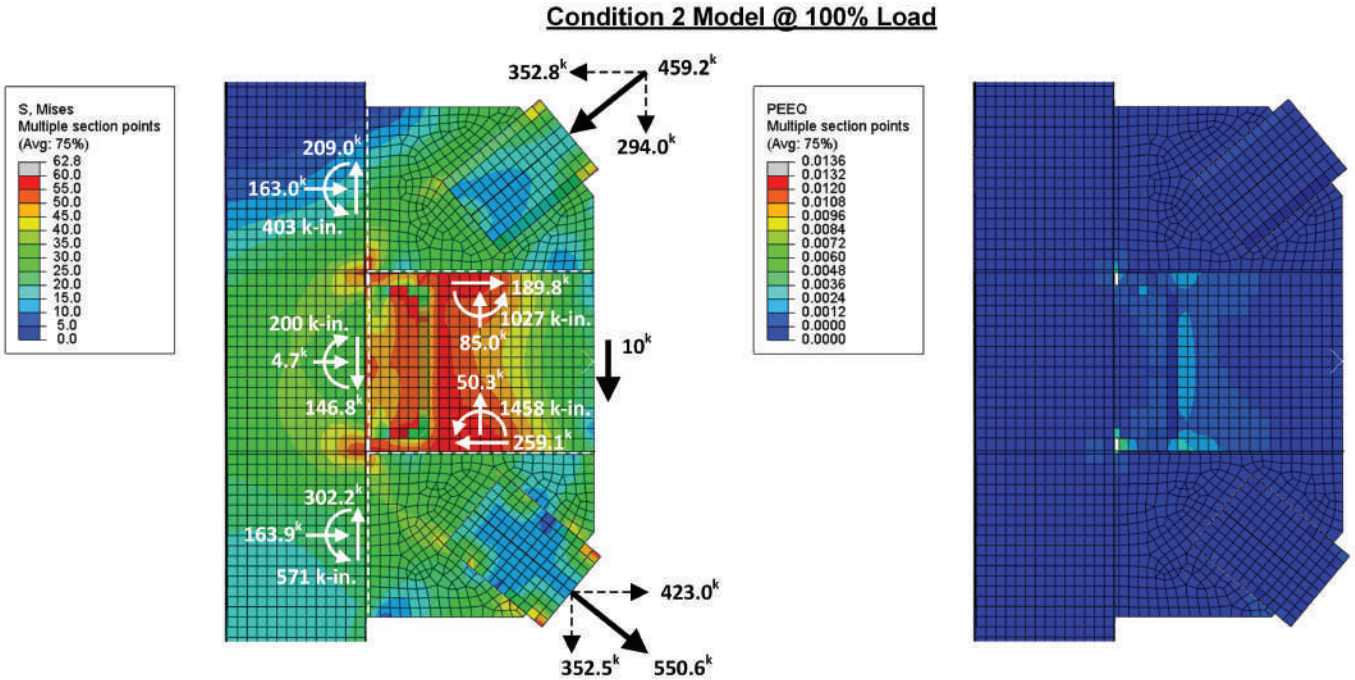

(a) Von Mises stress contour *(b) Equivalent plastic stain conto*

Fig. 17. Finite element analysis results of Example 3, condition 2.

Table 7. Comparison of Analysis and Design Vertical and Horizontal Forces for Condition 2					
Horizontal Forces	**H_{cTot} (kips)**	**H_{bTot} (kips)**	**Sum (kips)**	**% Column**	**% Beam**
Example 3 calculation	196	158	354	55%	45%
Calculation with $\phi F_y = 55$ ksi	159	194	353	45%	55%
Finite element analysis	163	190	353	46%	54%
Vertical Forces	**V_{cTot} (kips)**	**V_{bTot} (kips)**	**Sum (kips)**	**% Column**	**% Beam**
Example 3 calculation	219	75.4	294	74%	26%
Calculation with $\phi F_y = 55$ ksi	201	93.1	294	68%	32%
Finite element analysis	209	85.0	294	71%	29%

Table 8. Comparison of Analysis and Design Gusset-Edge Forces for Condition 2							
Forces at Column	**H_{cTot} (kips)**	**V_{cTot} (kips)**	**M_{cTot} (kip-in.)**	**Normal Stress (ksi)**	**Shear Stress (ksi)**	**Resultant Stress (ksi)**	**Angle (deg)**
Example 3 calculation	196	219	–1200	35.4	15.7	38.7	66.2
Calculation with $\phi F_y = 55$ ksi	159	201	–583	21.8	14.4	26.1	56.6
Finite element analysis	140	181	–403				
Stress calculated from finite element analysis forces				17.2	13.0	21.5	53.0
Forces at Beam	**V_{bTot} (kips)**	**H_{bTot} (kips)**	**M_{bot} (kip-in.)**	**Normal Stress (ksi)**	**Shear Stress (ksi)**	**Resultant Stress (ksi)**	**Angle (deg)**
Example 3 calculation	75.4	158	597	9.6	8.2	12.6	49.4
Calculation with $\phi F_y = 55$ ksi	93.1	194	731	11.7	10.1	15.5	49.4
Finite element analysis	107	203	1030				
Stress calculated from finite element analysis forces				15.3	10.5	18.6	55.4

dimension, r, set equal to r_{minBm}), section B1 is constrained to have a demand-to-capacity ratio of 1.0. Section B2 (using Equation 37) has a calculated demand of 91.9 kips, equal to the effective capacity of the beam (Equation 18). Thus, the analysis and design are consistent on a fundamental point: As the beam yields at these sections, the column can still continue to resist higher forces. Of note is that while the beam web and its connection to the column reach yield stress, the plastic strains remain low due to the redistribution of the forces in the connection to the column, consistent with the bypass design method.

The analysis confirms that the connection can support the design loads for condition 2. This supports the use of the bypass method. It should be noted that the Uniform Force Method without the bypass modification would indicate that this connection was inadequate. The plastic strains in the beam web are small, confirming that after beam-web yielding, the bypass mechanism provides sufficient strength and stiffness to preclude significant ductility demands. The analysis also confirms that condition 2 is more critical than condition 1 for this design.

The comparison of design forces from Example 3 to the analysis forces for condition 2 shows that the design model (which utilizes a specified minimum yield stress and a resistance factor) requires a greater portion of the brace force to bypass the beam. The more accurate finite element analysis shows a distribution closer to the Uniform Force method, with somewhat less force bypassing the beam than in the calculations, as shown in Tables 7 and 8. This difference is due in part to the disparity between the stresses permitted in the design model and the greater expected strength used in the analysis. For comparison, design calculations were performed using $\phi F_y = 55$ ksi (which required a bypass factor, λ, of 0.76, as compared to the value of 0.617 from the design example, corresponding to $\phi F_y = 50$ ksi). Forces corresponding to that analysis are also in Tables 7 and 8.

CONCLUSIONS AND RECOMMENDATIONS

This study provides design equations that can be used in the design of gussets in braced frames to minimize the required shear strength of the beams and columns in order to avoid the need for reinforcement. The design method allows engineers to select the proportion of the load that will contribute to beam or column shear and to redistribute the load between beam and column. Additionally, equations are provided that allow the gussets to be used to resist beam-connection moment, which potentially allows for a very economical design by eliminating the need for beam-flange-to-column-flange welds.

The authors recommend this modified implementation of the Uniform Force Method, especially for conditions in which web doublers would otherwise be required. The use of the bypass method provides additional economy, but engineers should be cognizant of the limited study performed to date. Without additional study, the authors do not recommend bypass factors λ less than 0.6. The use of the haunch method (with or without the bypass method) similarly provides for greater economy for connections with beam fixity. Based on the limited study performed to date, the authors recommend that the haunch method be implemented considering both the upper and lower bounds of beam moment (conditions 1 and 2). Further study is required to establish the lower bound of this moment, especially for systems with cyclic inelastic drift, for which the brace forces may reverse within the elastic drift range of the beam.

SYMBOLS

F_y Material specified minimum yield stress, ksi

H_b Horizontal force transferred to beam by gusset (from Uniform Force Method analysis), kips

H_{bH} Horizontal force transferred to beam due to haunch force, kips

H_{bW} Horizontal force at beam-web-to-column connection, kips

H_{bTot} Total horizontal force transferred to beam, kips

H_c Horizontal force transferred to column by gusset (from Uniform Force Method analysis), kips

H_{cBP} Horizontal force transferred to column by gusset from bypass force, kips

H_{cH} Horizontal force transferred to column by gusset to resist beam moment, kips

H_{cTot} Total horizontal force transferred to column by gusset, kips

M_{BC} Moment at column face resisted by beam-to-column connection, kip-in.

M_b Moment at gusset–beam interface (from Uniform Force Method analysis), kip-in.

M_{bH} Moment at gusset–beam interface from haunch force, kip-in.

M_{bTot} Total moment at gusset–beam interface, kip-in.

M_{BM} Moment at a beam section aligned with the gusset edge face, kip-in.

M_c Moment at gusset–column interface (from Uniform Force Method analysis), kip-in.

M_{cBP} Moment at gusset–column interface from bypass force, kip-in.

M_{cH} Moment at gusset–column interface from haunch force, kip-in.

M_{cTot} Total moment at gusset–column interface, kip-in.

M_f Moment at column face (from beam), kip-in.

M_H Moment at column face resisted by gusset, kip-in.

N Normal force on beam or column flange, kips

N_B Beam axial force delivered to the connection, kips

N_H Horizontal force at beam-to-column web connection due to haunch forces, kips

P_f Beam flange force at connection to column, kips

$P_{i,j}$ Brace axial force for brace j connecting to gusset i; sign conventions are per the figures, kips

R_n Nominal strength (of beam-to-column connection), kips

R_u Required strength, kips

U_C Ratio of connection effective strength, V_{efConn}, to beam effective strength, V_{efBm}

V_b Vertical force transferred to beam by gusset (from Uniform Force Method analysis), kips

V_{bH} Vertical force transferred to beam by gusset to resist beam moment, kips

V_{BMF} Beam shear due to moment-frame behavior, kips

V_{bW} Vertical force at beam-web-to-column connection, kips

V_g Beam shear due to gravity, kips

V_c Vertical force transferred to column by gusset (from Uniform Force Method analysis), kips

V_{cH} Vertical force transferred to column by gusset to resist beam moment, kips

V_{Col} Column shear due to moment-frame behavior, kips

V_{cBP} Vertical force transferred to column by gusset from bypass force, kips

V_{cTot} Total vertical force transferred to column by gusset, kips

V_{efBm} Effective beam shear strength, kips

$V_{efBi,j}$ Apportioned effective beam shear strength that can be used to resist the force for brace *j* connecting to gusset *i*; sign conventions are per the figures, kips

V_{efCol} Effective column shear strength, kips

$V_{efCi,j}$ Apportioned effective column shear strength that can be used to resist the force for brace *j* connecting to gusset *i*; sign conventions are per the figures, kips

V_{efConn} Effective beam-to-column connection shear strength, kips

V_{mid} Shear in beam or column at mid-length or mid-height of gusset, kips

V_n Nominal member shear strength, kips

d_b Beam depth, in.

e_b Eccentricity from beam flange to beam centerline, equal to half the beam depth, in.

e_c Eccentricity from column flange to column centerline, equal to half the column depth, in.

h_o Distance between beam flange centroids, in.

r Gusset centroid offset (dimension from workpoint to brace control point in Uniform Force Method), in.

r_{minBm} Minimum dimension *r* based on beam shear yielding, in.

r_{minCol} Minimum dimension *r* based on column shear yielding, in.

t_g Gusset thickness, in.

α Distance from column face to centroid of Uniform Force Method force acting on beam flange, in.

$\overline{\alpha}$ Half of gusset horizontal dimension (centroid of gusset–beam interface), in.

β Distance from beam flange to centroid of Uniform Force Method force acting on column face, in.

$\overline{\beta}$ Half of gusset vertical dimension (centroid of gusset–column interface), in.

ϕ Resistance factor

λ Brace force apportionment factor (between Uniform Force Method and "bypass force")

ρ Beam moment apportionment factor (between beam flange and haunch force in gusset)

θ Brace angle from vertical, deg

REFERENCES

AISC (2016), *Seismic Provisions for Structural Steel Buildings*, ANSI/AISC 341-16, American Institute of Steel Construction, Chicago, Ill.

AISC (2017), *Manual of Steel Construction*, 15th Ed., American Institute of Steel Construction, Chicago, Ill.

Euler, L. (translated by Hewlett, J.) [published 1765; 1822 translation], "Of a New Method of Resolving Equations of the Fourth Degree," *Elements of Algebra*, Longman, Hurst, Rees, Orme, and Company, London.

Fortney, P.J. and Thornton, W.A. (2015), "The Chevron Effect—Not an Isolated Problem," *Engineering Journal*, AISC, Vol. 52, No. 2, pp. 125–164.

Muir, L.S. and Thornton, W.A. (2014), *Vertical Bracing Connections: Analysis and Design,* Design Guide 29, AISC, Chicago, Ill.

Richards, P., Miller, B., and Linford, J. (2018), *Finite Element Evaluation of the Chevron Effect in Braced Frames*. Brigham Young University Report No. SSRP-2018/02.

Sabelli, R. and Arber, L. (2017), "Design of Chevron Gusset Plates," 2017 SEAOC Convention Proceedings.

Sabelli, R., and Saxey, B., (2021), "Design for Local Member Shear at Brace Connections: Full-Height and Chevron Gussets," *Engineering Journal*, AISC, Vol. 58, No. 1, pp. 45–78.

Thornton, W.A. (1984). "Bracing Connections for Heavy Construction," *Engineering Journal*, AISC, Vol. 21, No. 3, pp. 139–148.

Thornton, W.A. (1991), "On the Analysis and Design of Bracing Connections," *Proceedings of the AISC National Steel Construction Conference,* Washington, D.C.

Interaction Strength of Steel-Concrete Composite Beam-Columns Including the Balance Point

Mark D. Denavit

Note: A version of this paper appears in the proceedings of the 2020 Structural Stability Research Council (SSRC) Annual Stability Conference

ABSTRACT

The maximum bending moment capacity of steel-concrete composite column cross sections occurs with concurrently applied axial compression. This is seen in the shape of the interaction diagram, where the bending moment capacity increases with increasing axial compression before reaching the balance point. The size of this bulged region of the interaction diagram can be significant, especially for concrete-dominant sections. However, it is often neglected in design because of two stability-related concerns. First, the simple transformations that are recommended to convert cross-section strength to member strength produce illogical results near the balance point, with member strength exceeding cross-section strength. Second, research has shown that the stiffness reductions used in elastic analyses are not sufficient for highly slender concrete-dominant composite members subjected to high bending moments. This work seeks to address these issues through the development of more advanced transformations and stiffness reductions. These new recommendations will more accurately capture the strength of composite members and allow for more efficient designs.

Keywords: composite construction, interaction strength, balance point, stiffness reduction.

INTRODUCTION

Steel-concrete composite frames are an effective alternative to structural steel or reinforced concrete frames for use as the primary lateral-force-resisting system of building structures. However, they have not yet been as widely adopted in United States practice as they have in other parts of the world, notably East Asia. There are several barriers to the broader use of composite structures. Sequencing issues in construction, which can lead to complications such as difficult coordination of trades, can be a barrier. On the other hand, innovative composite construction methods that resolve the sequencing issues can be highly efficient and can reduce construction time (Griffis, 1992; Traut-Todaro, 2019). Current design provisions are another barrier to the wider adoption of composite construction. Despite recent advances (e.g., Lai et al., 2015; Denavit et al., 2016; Bruneau et al., 2018), design provisions for composite frames are not yet as comprehensive as those for the more traditional systems, nor do they consistently reflect the advantages of composite framing.

Composite columns were introduced to the AISC *Specification for Structural Steel Buildings*, hereafter referred to as the AISC *Specification*, in the 1986 edition (AISC, 1986). From that time until major revisions were made in the 2005 edition (AISC, 2005), the axial and flexural strengths of composite beam-columns were based on calculations that determined an equivalent steel section. This approach had limitations in that it was not applicable to columns with steel ratios below 4%, and it often underestimated the contribution of the concrete, particularly for concrete-dominant composite beam-columns with low steel ratios (Griffis, 2005). The current beam-column strength interaction provisions (AISC, 2016) are based more directly on mechanics principles. The cross-section strength may now be determined using one of several methods; the two most commonly used are the plastic stress distribution method, which is applicable to most common composite column cross sections, and the more general strain-compatibility method, which is comparable to approaches often taken to compute reinforced concrete section strength. The plastic stress distribution method is the primary method for assessing steel-concrete composite columns in the AISC *Specification* (AISC, 2016) and other standards worldwide (CEN, 2004; SAC, 2014). It is accurate over a wide range of materials, cross-sectional geometries, and loading conditions, but the method does result in significant unconservative error for some cases. Cases of unconservative error include encased composite members, also known as steel-reinforced concrete (SRC) members, with high steel ratio, high steel yield stress, or both (Behnam and Denavit, 2020). The strain-compatibility method is conservative in nearly all cases but can be overly conservative in many cases. The

Mark D. Denavit, Assistant Professor, The University of Tennessee, Knoxville, Knoxville, Tenn. Email: mdenavit@utk.edu

Paper No. 2020-11

revisions in the 2005 edition also included an expansion of the range of applicability of the provisions to members with steel ratios as low as 1%.

Using the plastic stress distribution method, pairs of axial compression and bending moment strength are computed based on assumed plastic neutral axis locations. Selecting many possible locations for the plastic neutral axis results in an essentially continuous curve for the interaction diagram. For example, the interaction diagram for the SRC cross section shown in Figure 1 for bending about the major axis of the steel shape is shown in Figure 2(a). This cross section has outside dimensions of 28 in. × 28 in., a W10×49 wide-flange steel shape, and four #8 reinforcing steel bars. The steel ratio (i.e., the ratio of area of steel to gross area of the cross section) for this cross section is $\rho_s = A_s/A_g$ = 1.81% (note that, for simplicity, the fillets between the web and the flange are neglected in this work). The reinforcing ratio (i.e., the ratio of area of reinforcing steel to gross area of the cross section) for this cross section is $\rho_{sr} = A_{sr}/A_g$ = 0.40%. The concrete compressive strength is f'_c = 8 ksi, the steel yield stress is F_y = 50 ksi, and reinforcing steel yield strength is F_{yr} = 60 ksi. The longitudinal reinforcing has a cover of 1⅞ in. from the edge of the concrete to the edge of the bar.

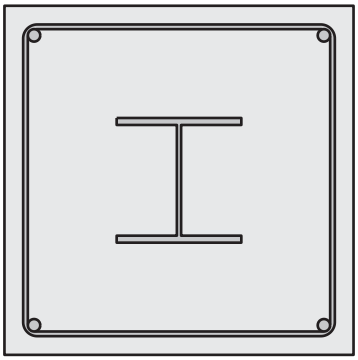

Fig. 1. Example SRC cross section.

The example cross section shown in Figure 1 was selected to have low steel ratios, near the lower limits given in the AISC *Specification* (AISC, 2016) since neglecting the balance point reduces the available strength for concrete-dominant members more than it does for steel-dominant members. This cross section is used in example analyses described throughout this paper.

While the plastic stress distribution method can be used to compute a continuous cross-section interaction diagram by selecting many different plastic neutral axis locations, doing so is burdensome by hand or spreadsheet. A set of closed-form equations (AISC, 2017) has been developed to compute key points on the curve which can then be used to construct a multilinear interaction diagram. The points are labeled A, C, D, and B as shown in Figure 2(a). Point A represents the pure axial strength; point B represents the pure bending strength; point C has the same bending moment as point B, but with axial compression; point D represents the balance point, the point of maximum bending moment.

Computing the cross-section interaction strength is relatively straightforward; however, it is not directly used in

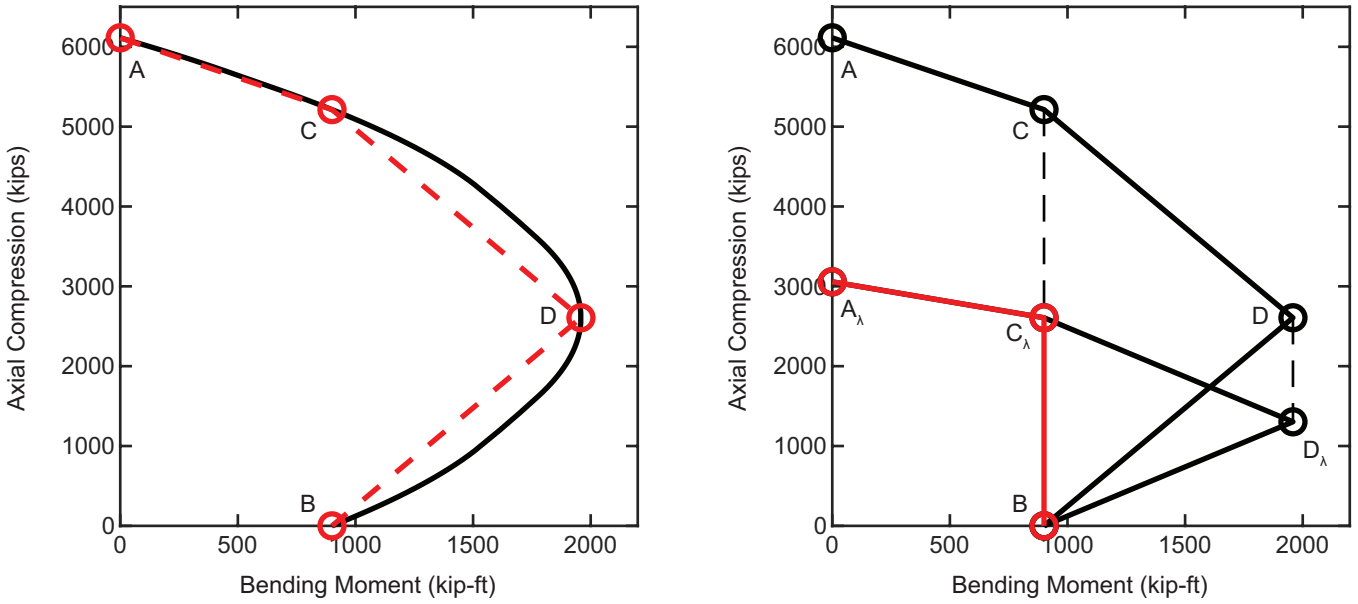

(a) Continuous vs. discrete (ACDB)

(b) Cross-section strength vs. beam-column strength

Fig. 2. Interaction strength diagrams for the example SRC cross section.

design. As described in the AISC *Specification* Commentary (AISC, 2016), two reductions are applied to the nominal cross-section interaction strength to obtain the available beam-column interaction strength.

The first is a stability reduction, where a factor equal to the ratio of the nominal axial compression strength with and without length effects ($\chi = P_n/P_{no}$) is applied to the ordinate (i.e., axial compression) of each point on the interaction diagram, leaving the abscissa (i.e., bending moment) unchanged. This method is logical in that it yields the proper results for pure axial compression (point A) and for pure bending moment (point B), but illogical and potentially unconservative results arise in the intermediate points, particularly the balance point (point D). The balance point is the point of maximum moment and it occurs for a nonzero axial compression. When the stability reduction is applied in this simple manner, the resulting beam-column interaction point D lies outside of the cross-section interaction diagram, as shown in Figure 2(b). Note that the beam-column strength interaction diagram shown in Figure 2(b) was constructed with $\chi = 0.5$, which corresponds to $L_c/H = 18.6$ for the example cross section.

The second reduction is to apply the resistance factors. The resistance factors for composite columns are defined as $\phi_c = 0.75$ for axial compression and $\phi_b = 0.90$ for flexure in AISC *Specification* Chapter I (AISC, 2016). For combined bending and axial load, the AISC *Specification* Commentary recommends that axial compression of each point be multiplied by ϕ_c and the bending moment of each point be multiplied by ϕ_b. This simple procedure may be unconservative because it can lead to strength reductions which imply resistance factors greater than 0.90 for the intermediate points (Denavit, 2017).

Furthermore, when evaluated against advanced second-order inelastic analyses, current design provisions can result in unconservative errors for highly slender, concrete-dominant composite members subject to low axial loads and high bending moments (Denavit et al., 2016). Concerns resulting from the simple reductions and potential unconservative error have led to the recommendation in the AISC *Specification* Commentary to neglect point D in the strength interaction diagram and to only consider points A, C, and B (AISC, 2016).

Neglecting the balance point can be highly conservative, especially for stocky concrete-dominant columns. Improved methods of determining interaction strength of steel-concrete composite beam-columns would have the potential of unlocking large amounts of strength and allowing composite columns to fulfil more of their potential. This work explores potential alternative approaches for including the balance point within the interaction strength of steel-concrete composite beam-columns. This work has two complimentary goals. The first goal is to reduce conservative error introduced by neglecting the balance point. The second goal is to reduce the unconservative error observed for highly slender, concrete-dominant composite members, which may be exacerbated by the inclusion of the balance point. To accomplish these goals, an alternative stability reduction for interaction diagrams and an alternative stiffness reduction to be used with the direct analysis method are evaluated.

ALTERNATIVE STABILITY REDUCTION FOR INTERACTION DIAGRAMS

As described in the previous section, the method for computing the interaction strength of steel-concrete composite columns, which is referred to as Simplified Method 2 in the AISC *Specification* Commentary (AISC, 2016), neglects the balance point (point D). While any number of points on the cross-section interaction diagram can be computed, only three points, A, C, and B are utilized for the available strength of composite beam-columns. Interaction diagrams computed following these recommendations for the example SRC cross section and for a variety of effective lengths are shown in Figure 3(a). The conservativeness of neglecting point D can be seen by comparing the interaction diagrams in Figure 3(a) to the cross-section interaction diagram shown in Figure 2(a). The example SRC cross section is concrete-dominant, so the moment strength at point D is significantly greater than that at point B.

Interaction diagrams using an alternative method of applying the stability reduction are shown in Figure 3(b). In this alternative method, points A, C, and B are computed and reduced as before (i.e., factoring the ordinate by $\chi = P_n/P_{no}$). Noting that factoring just the ordinate for point D gives the illogical result of a point on the beam-column interaction strength diagram outside of the cross-section interaction strength diagram, both the ordinate and the abscissa of point D are reduced. The ordinate of point D is reduced by the same factor as the other points. The abscissa is reduced such that the reduced point D remains on the line between point B and the original point D, thus ensuring that the beam-column interaction strength does not exceed the cross-section interaction strength. A summary of the reduction applied to each point is presented in Table 1.

The interaction diagram including point D and constructed using the alternative stability reduction (denoted as the ACDB interaction) provides a plausible alternative to the interaction diagram currently recommended in the AISC *Specification* Commentary (AISC, 2016) (denoted as the ACB interaction). However, the new interaction diagram must be rigorously evaluated to ensure that it results in safe designs.

When evaluating design provisions for beam-column interaction strength, simply comparing available strengths

Table 1. Points on the Interaction Diagram				
	Cross-Section Strength		Beam-Column Strength	
Point	***M***	***P***	***M***	***P***
A	0	P_A	0	χP_A
C	M_C	P_C	M_C	χP_C
D[a]	M_D	P_D	$(1-\chi)M_B + \chi M_D$	χP_D
B	M_B	0	M_B	0

[a] Point D is not included with the ACB interaction diagram.

computed per design equations to the results of physical experiments or advanced inelastic analyses can be misleading. In practice, available strengths are evaluated against required strengths and required strengths are computed following particular rules (e.g., specific type of analysis, defined stiffness). The provisions for an entire method of design, encompassing both the available and required strengths, must be considered in the evaluation.

Many notable studies have been conducted in this way, including for structural steel columns and the development of the interaction equations in use today (Kanchanalai, 1977), for reinforced concrete columns (Hage and MacGregor, 1974), for the development of the direct analysis method (Surovek-Maleck and White, 2004), and for the extension of the direct analysis method to composite frames (Denavit et al., 2016). Each of these studies duly considered both the calculation of available strength and required strength in their evaluations, albeit using somewhat different approaches. This work expands upon the results presented by Denavit et al. (2016). The approach taken is to compare, for many different individual cases, the maximum applied loads permitted by the design methodology to the applied loads at which failure occurs according to second-order inelastic analyses.

Benchmark Frames

The cases investigated are small frames that consist of a single composite column as shown in Figure 4. The same broad range of cross-section and frame parameters investigated by Denavit et al. (2016) were used in this work.

Four categories of cross section were investigated: (1) circular concrete-filled steel tubes (CCFT), (2) rectangular concrete-filled steel tubes (RCFT), (3) SRC subjected to major-axis bending, and (4) SRC subjected to minor-axis bending. Within these groups, sections were selected to

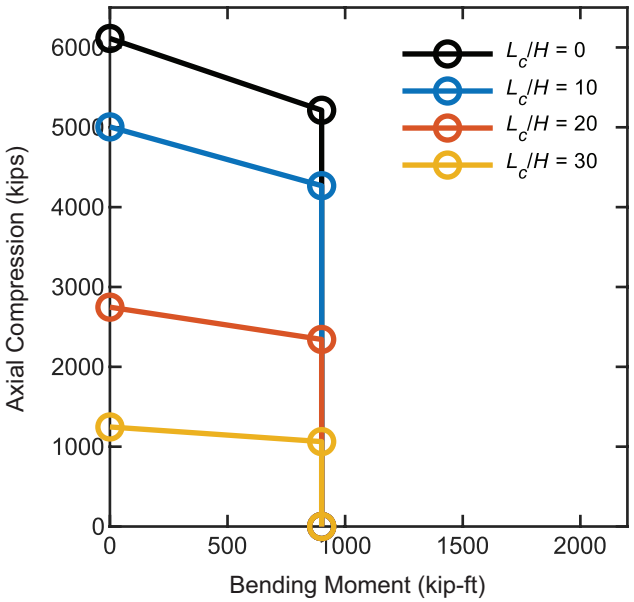

(a) Simplified method 2 (ACB)

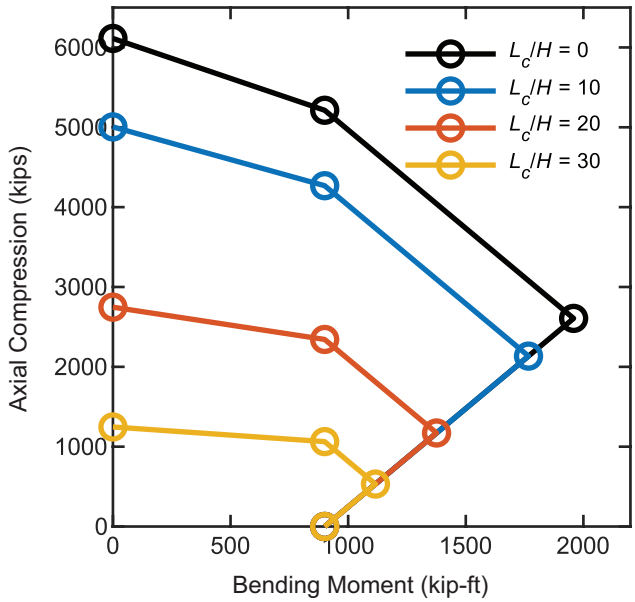

(b) Proposed method (ACDB)

Fig. 3. Interaction strength diagrams for beam-columns with the example SRC cross section.

span practical ranges of concrete strength; steel ratio; and, for the SRC sections, reinforcing ratio. Steel yield strengths were selected as F_y = 50 ksi for wide-flange shapes, F_y = 42 ksi for round HSS shapes, F_y = 46 ksi for rectangular HSS shapes, and F_{ysr} = 60 ksi for reinforcing bars. Three concrete strengths were selected: f'_c = 4, 8, and 16 ksi. Note that the AISC *Specification* (AISC, 2016) limits concrete strength to a maximum of 10 ksi. Concrete exceeding this limit was included to investigate an extreme case and because the limits may be revised in future editions.

With the selected CFT sections, the full range of permitted steel ratios is examined, including those associated with noncompact and slender sections. However, local buckling is neglected in this study, both by not modeling it in the inelastic analyses and by not including the strength reductions in the design strength calculations. The effects of local buckling on the interaction strength of filled composite members can be captured in design through the use of the effective stress-strain method defined in AISC *Specification* Section I1.2 (AISC, 2016) and in analysis through the use of beam elements with specialized constitutive relations or shell elements (Lai and Varma, 2016). Nonetheless, local buckling remains a complicated issue that was excluded from this work for simplicity. Thus, the results of this study are only strictly applicable to compact sections.

As shown in Figure 4, both sidesway inhibited and sidesway uninhibited cases were investigated. The frames are based on and expanded from those used in previous studies (Kanchanalai, 1977; Surovek-Maleck and White, 2004). For the sidesway inhibited frames, a range of column lengths, L, and end moment ratios, β, were investigated. For the sidesway uninhibited frames, a range of column lengths, L, leaning column load ratios, γ, and end restraints (rotational spring stiffnesses, $k_{\theta,top}$ and $k_{\theta,bot}$) were investigated. Each cross section was run with each frame resulting in 1,200 individual cases for each of the CCFT and RCFT groups and 2,880 individual cases for each of the SRC groups. Full details of the selected benchmark frames are reported by Denavit et al. (2016).

Second-Order Inelastic Analysis

Geometric and material nonlinear analyses using fiber-based beam finite elements were used to obtain results against which the design methodologies are benchmarked. These analyses represent the "best guess" of the true behavior of the frames. The uniaxial constitutive relations defined within the fiber representations of the cross sections were calibrated specifically for composite columns. As noted previously, local buckling of the steel tube and other steel components was neglected. Initial system and member geometric imperfections were directly modeled. Full details of the analyses, including validation against the results of hundreds of physical experiments are reported by Denavit et al. (2016) and Denavit and Hajjar (2014).

A sample of analysis results is presented in Figure 5 for various lengths of the sidesway inhibited frame with β = 1 and with the example SRC cross section shown in Figure 1 and described previously. A series of analyses was performed to obtain the results for each individual case shown in Figure 5. First, an analysis applying only vertical load (i.e., M = 0; see Figure 4) was performed to determine the peak load. In this analysis, load was applied and increased in displacement control until a limit point was determined. The limit point was defined as when the lowest eigenvalue

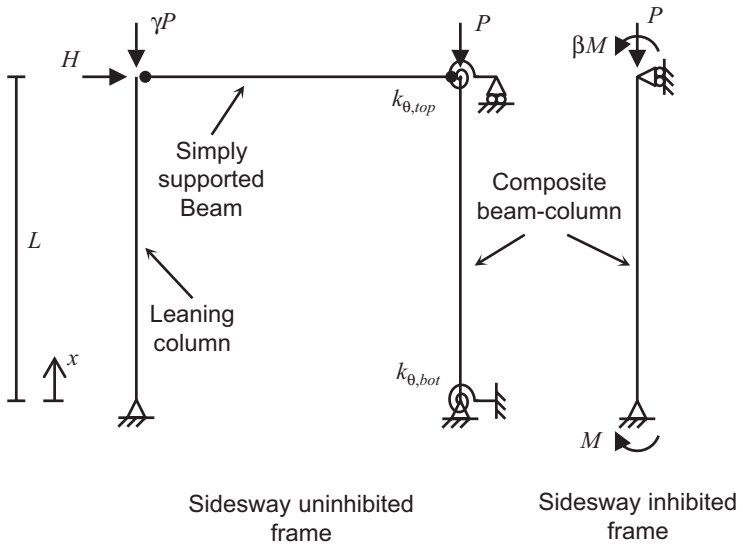

Fig. 4. Benchmark frames.

of the stiffness matrix was equal to zero. This coincides with the maximum applied axial compression. Then, eight separate nonproportional analyses were performed with different values of axial compression equally spaced from zero to the maximum applied axial compression from the axial-only analysis. In each of these nonproportional analyses, the specified level of axial compression is applied in load control then held constant. Subsequently, the lateral load is applied and increased in displacement control until a limit point was determined. The limit point was defined as when the lowest eigenvalue of the stiffness matrix was equal to zero. This coincides with the maximum applied moment. In each analysis, the applied loads and maximum internal forces at the limit point are recorded. These are the values shown in Figure 5. The same process was used for all other interaction diagrams developed using second-order inelastic analyses in this work.

Design Methodology

The maximum applied loads permitted by the design methodology are obtained from an automated iterative process as the applied loads that produce maximum internal forces from an elastic analysis that lay directly on the design interaction diagram [either the ACB such as shown in Figure 3(a) or the ACDB interaction such as shown in Figure 3(b)]. The elastic analyses are performed by evaluating closed-form solutions to the governing differential equation for the benchmark frames obtained from a computer algebra system. Only flexural deformations are considered. The nominal flexural stiffness of the composite columns is taken as EI_{eff} as defined in the AISC *Specification* (AISC, 2016). All stiffnesses are reduced by 0.8, and the flexural stiffness of the composite column is reduced by an additional factor $\tau_b = 0.8$. A notional lateral load of 0.002 times the vertical load was included. The notional load was taken as an additive load when the ratio of second-order drift to first-order drift was greater than or equal to 1.7. It was taken as a minimum lateral load otherwise. A sample of results is presented in Figure 6(a) for the example SRC cross section and the same frames investigated in Figure 5.

Results

The key result from these analyses is the error measured along a radial line from the origin between the interaction diagrams constructed from the maximum applied loads permitted by the design methodology and the applied loads at which failure occurs according to the second-order inelastic analyses. A sample comparison is shown in Figure 6(b) for the example SRC cross section and the sidesway inhibited frame with $L/H = 40$, where H is the lateral dimension of the cross section. For higher axial loads the interaction diagram constructed from the inelastic analyses is outside the interaction diagram constructed from the design methodology, indicating conservative error of up to 70%. For higher bending moments the opposite is true, albeit to a lesser degree, with maximum unconservative error of up to 8%. In this range, the design methodology permits applied loads that the inelastic analysis indicates would result in failure.

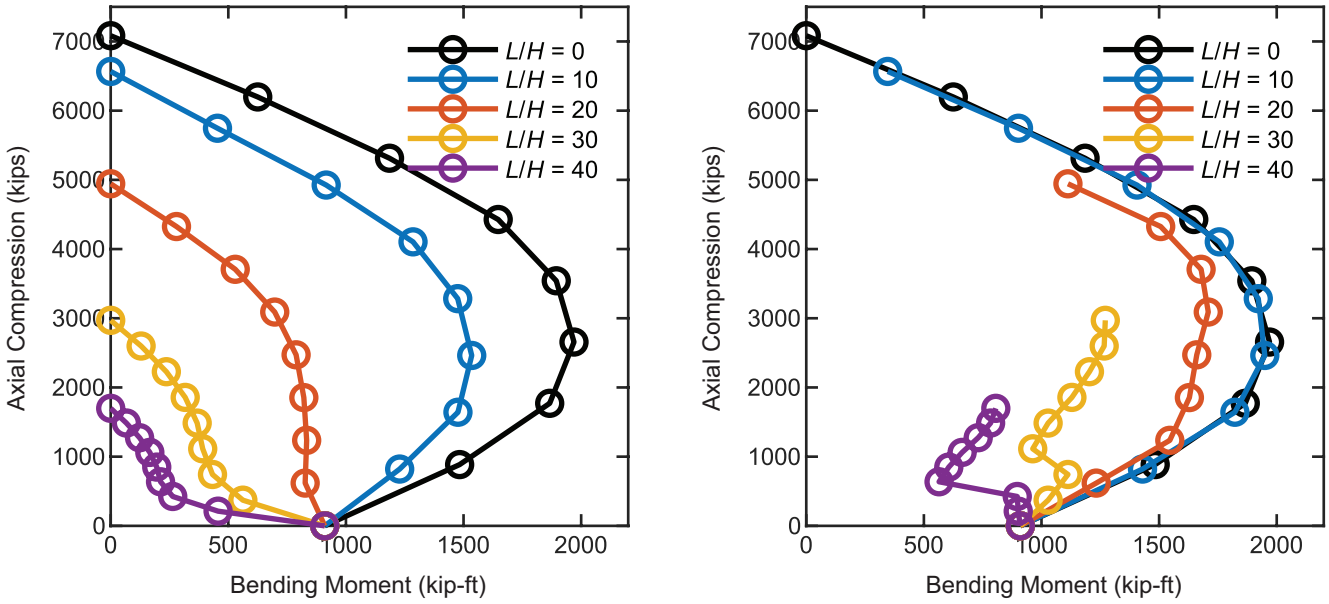

(a) Applied loads *(b) Internal forces*

Fig. 5. Second-order inelastic analysis results for frames with the example SRC cross section.

The error was evaluated for all benchmark frames, at many angles within the *M-P* plane, and for both the ACB and ACDB interaction diagrams. While the selected cross sections and frame parameters can be considered to span the practical range, the distribution of parameters within the selection may not be representative of what is expected in practice. For instance, the selected set contains a far higher proportion of very slender frames than would be expected in typical construction. Accordingly, maximum and minimum error values are more meaningful than median or average error values. Two of the most influential parameters within the set are the steel ratio, ρ_s, and the slenderness. Slenderness is defined by the parameter λ_{oe} (Equation 1) which is proportional to the effective length of the columns. An effective length factor was computed and used for determining λ_{oe} (note, however, that the available strength was computed with an effective length factor of unity in accordance with the direct analysis method). The frames were separated into bins based on ranges of steel ratio and slenderness to better understand the error. The ranges used to separate the frames based on slenderness are shown in Table 2. The maximum unconservative error for each of the bins for the ACDB interaction is shown in Table 3.

$$\lambda_{oe} = \sqrt{\frac{P_{no}}{P_e}} \tag{1}$$

$$P_e = \frac{\pi^2 EI_{eff}}{(KL)^2} \tag{2}$$

The maximum unconservative error varies significantly with section type, slenderness, and steel ratio. The greatest unconservative errors are seen for the slenderest and most concrete-dominant cases. There is no specified limit on the level of unconservative error that can be tolerated within a design methodology. One reference identifies a 5% unconservative error as a reasonable maximum (ASCE, 1997). Another study identified unconservative errors as large as 16% for structural steel columns designed according to the direct analysis method with direct modeling of member imperfections (Wang and Ziemian, 2019). It is important to note that large unconservative errors have been found using the ACB interaction as well (Denavit et al., 2016). Given that the ACDB interaction diagram is larger than the ACB interaction diagram, use of the ACDB interaction diagram can only increase the maximum unconservative errors. The increase in maximum unconservative error for each bin is presented in Table 4. Compared to the magnitude of error, the increase due to the inclusion of point D is modest.

The primary reason to include point D is to reduce conservative error in the evaluation of strength. The decrease in maximum conservative error by including point D for each bin is presented in Table 5. As expected, the largest decreases in conservative error occur for stockier and more concrete-dominant frames. This range is likely more practical and common in construction than the highly slender members for which the high unconservative errors are seen, indicating that the addition of point D would be highly beneficial. Nonetheless, given the increases in

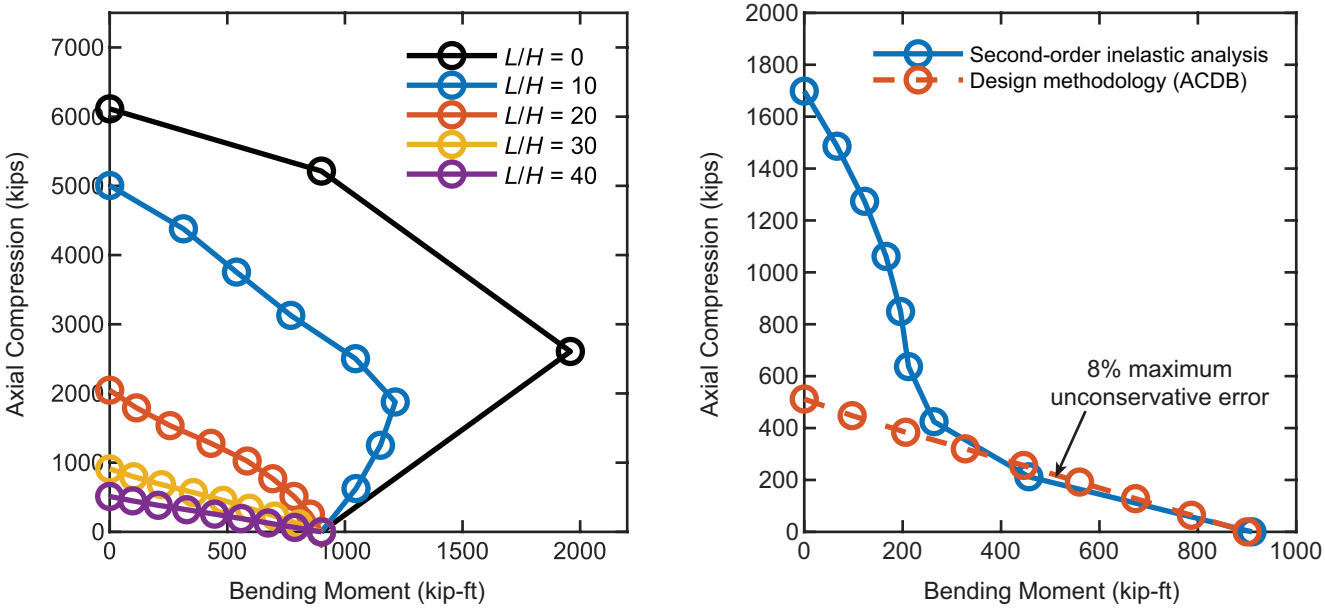

(a) Design methodology—ACDB interaction *(b) Comparison with OpenSees (L/H = 40)*

Fig. 6. Maximum permitted applied loads for frames with the example SRC cross section.

Table 2. Definition of Slenderness Ranges	
Range	**Slenderness**
I	$\lambda_{oe} \leq 0.5$
II	$0.5 < \lambda_{oe} \leq 1.0$
III	$1.0 < \lambda_{oe} \leq 1.5$
IV	$1.5 < \lambda_{oe} \leq 2.0$
V	$2.0 < \lambda_{oe} \leq 3.0$
VI	$3.0 < \lambda_{oe}$

Table 3. Maximum Unconservative Error Based on Slenderness and Steel Ratio, ACDB Interaction							
	ρ_s	I	II	III	IV	V	VI
CCFT	0.25	6.00%	14.6%	12.5%	13.7%	5.70%	5.90%
	0.18	4.40%	12.4%	14.0%	15.9%	8.60%	9.10%
	0.11	5.20%	9.50%	14.4%	17.9%	11.4%	12.8%
	0.06	6.40%	8.90%	11.7%	12.7%	19.3%	17.9%
	0.02	5.40%	6.70%	7.00%	15.6%	24.8%	36.3%
RCFT	0.28	1.70%	2.40%	1.90%	3.00%	0.00%	0.00%
	0.19	4.30%	3.60%	5.20%	7.00%	0.90%	1.30%
	0.11	4.00%	4.60%	8.20%	11.4%	6.30%	7.10%
	0.06	3.90%	4.90%	8.70%	6.20%	16.3%	15.7%
	0.03	1.60%	0.50%	4.80%	10.5%	18.7%	21.8%
SRC major-axis	0.12	6.90%	5.90%	3.60%	4.70%	6.80%	2.10%
	0.09	4.70%	3.60%	3.80%	6.70%	8.90%	4.00%
	0.04	2.00%	0.90%	2.40%	9.70%	14.3%	13.1%
	0.01	2.10%	2.10%	5.00%	7.40%	14.7%	29.2%
SRC minor-axis	0.12	17.4%	15.8%	14.9%	13.9%	14.1%	8.60%
	0.09	13.8%	14.6%	10.3%	12.8%	13.0%	6.80%
	0.04	5.50%	5.70%	8.00%	11.0%	13.8%	11.4%
	0.01	2.10%	2.10%	4.30%	7.50%	11.2%	28.1%

maximum unconservative error, this approach cannot be recommended for general use unless paired with additional changes that reduce the maximum unconservative errors.

ALTERNATIVE STIFFNESS REDUCTION

The previous section addressed the source of some of the greatest conservative errors that exist in the provisions for steel-concrete composite columns. The ACDB interaction diagram significantly reduced the level of conservative error while only modestly increasing the unconservative error. However, the unconservative error was already high in some cases. The greatest unconservative errors occur for highly slender, concrete-dominant members with large flexural demands. Cases such as these are perhaps not often seen in practice, since most engineers wisely avoid this range. However, there is no slenderness limit within the AISC *Specification* (AISC, 2016) and thus cases for which large errors are recorded are permitted. One remedy to these high errors would be to further reduce the size of the interaction diagram. However, a different remedy related to the stiffness reduction may be more appropriate.

The errors occur with low axial loads and high bending moments. High levels of concrete cracking are expected in composite columns under this loading, which is more beam-like than column-like. The flexural rigidity used for composite columns when determining required strengths within the direct analysis method is $0.8\tau_b EI_{eff}$, where

Table 4. Percentage Point Increase in Maximum Unconservative Error Based on Slenderness and Steel Ratio							
	ρ_s	I	II	III	IV	V	VI
CCFT	0.25	3.00%	0.00%	2.50%	1.50%	1.00%	0.70%
	0.18	2.00%	0.00%	3.90%	2.20%	1.30%	1.00%
	0.11	2.40%	2.70%	5.10%	4.00%	3.10%	1.70%
	0.06	0.40%	3.20%	3.20%	6.40%	6.30%	3.10%
	0.02	0.00%	0.40%	7.00%	9.20%	7.70%	7.50%
RCFT	0.28	0.00%	0.00%	1.90%	1.20%	0.00%	0.00%
	0.19	0.00%	0.00%	2.40%	1.90%	0.90%	0.90%
	0.11	0.00%	1.70%	4.00%	3.70%	2.20%	1.70%
	0.06	0.10%	2.60%	4.50%	5.50%	7.10%	3.50%
	0.03	0.00%	0.00%	4.80%	6.20%	7.70%	4.80%
SRC major-axis	0.12	0.00%	0.00%	2.20%	2.30%	2.40%	0.70%
	0.09	0.20%	0.30%	2.30%	4.80%	2.60%	1.20%
	0.04	1.00%	0.20%	1.70%	6.20%	4.70%	2.00%
	0.01	0.00%	0.00%	2.90%	3.30%	3.00%	4.80%
SRC minor-axis	0.12	0.00%	0.50%	0.20%	0.40%	0.20%	0.10%
	0.09	0.30%	0.30%	0.70%	0.40%	0.20%	0.50%
	0.04	0.00%	1.90%	1.80%	0.80%	2.70%	1.40%
	0.01	0.00%	0.00%	2.20%	3.10%	3.40%	4.50%

Table 5. Percentage Point Decrease in Maximum Conservative Error Based on Slenderness and Steel Ratio							
	ρ_s	I	II	III	IV	V	VI
CCFT	0.25	0.00%	0.00%	0.00%	0.00%	0.00%	0.00%
	0.18	0.00%	5.40%	0.00%	0.30%	0.00%	0.00%
	0.11	14.4%	16.5%	1.40%	0.60%	0.80%	0.10%
	0.06	32.4%	28.8%	11.7%	3.20%	1.10%	0.70%
	0.02	33.6%	32.3%	25.5%	9.20%	4.50%	2.10%
RCFT	0.28	0.00%	0.00%	0.00%	0.00%	0.00%	0.00%
	0.19	5.20%	0.00%	0.20%	0.40%	0.00%	0.00%
	0.11	16.9%	10.6%	1.80%	0.70%	0.80%	0.00%
	0.06	31.9%	21.1%	4.70%	2.70%	0.00%	0.70%
	0.03	34.4%	33.4%	18.2%	4.40%	1.60%	1.20%
SRC major-axis	0.12	13.7%	0.00%	0.80%	0.50%	0.30%	0.30%
	0.09	20.6%	6.20%	1.00%	0.80%	0.30%	0.30%
	0.04	30.7%	12.6%	2.20%	0.70%	1.10%	0.30%
	0.01	30.3%	29.0%	10.6%	2.40%	2.20%	0.00%
SRC minor-axis	0.12	0.00%	0.00%	0.30%	0.40%	0.00%	0.20%
	0.09	5.90%	4.10%	1.10%	0.50%	0.00%	0.10%
	0.04	28.2%	9.50%	0.90%	0.40%	0.70%	0.20%
	0.01	30.2%	28.5%	10.0%	2.20%	2.10%	0.00%

$\tau_b = 0.8$ and EI_{eff} is the flexural rigidity used within the column curve for determination of axial compression strength. Further reductions to the stiffness would help eliminate the observed unconservative errors. An example alternative stiffness reduction factor, τ_b, is shown in Equation 3:

$$\tau_b = 1.25 - \frac{M_r}{M_n}\left(1 - 3\frac{P_r}{P_{no}}\right) \leq 0.8 \quad (3)$$

This equation is based on prior work (Denavit and Hajjar, 2014). Data on the secant flexural rigidity was computed based on results from second-order inelastic analysis; an equation was then fit to the data. The variation of the τ_b described by Equation 3 with internal forces is shown in Figure 7. The reduction factor is a constant $\tau_b = 0.8$ for much of the range. Only with high bending moment and low axial loads, where high levels of cracking are expected, does τ_b become less than 0.8 and vary with the axial compression and bending moment.

Performing an elastic analysis with a stiffness reduction that varies with internal forces can be cumbersome. However, there is precedent in U.S. practice. For structural steel members, the factor τ_b varies with axial compression. For reinforced concrete members, the ACI *Building Code Requirements for Structural Concrete and Commentary* (ACI, 2019) includes provisions for an effective flexural rigidity that varies with both axial compression and bending moment.

The effect of the alternative stiffness reduction on the maximum permitted applied loads for the example SRC cross section is shown in Figure 8(a). The solid lines represent the maximum permitted applied loads using a constant $\tau_b = 0.8$; the dashed lines represent the maximum permitted applied loads using Equation 3. The percentage difference between the two is shown in Figure 8(b). The reduction is sufficient to eliminate the unconservative error [e.g., as shown in Figure 6(b).] There are also other attractive features. The alternative stiffness reduction has no effect on the pure bending strength, nor does it affect the strength when the axial compression is high. Also, as seen in Figure 8(b), it has a greater effect on more slender members, for which additional conservatism is likely warranted. The specific factors in Equation 3 should be refined and a wide ranging evaluation should be performed to ensure safety and accuracy, but these limited results show the promise of a moment-based stiffness reduction in efficiently eliminating some of the largest unconservative errors observed in the design provisions for steel-concrete composite framing systems.

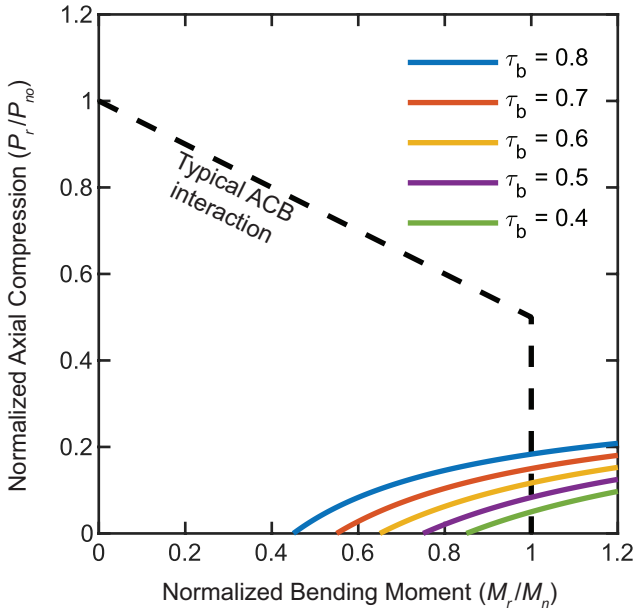

Fig. 7. Contour plot showing the variation of the alternative stiffness reduction factor.

CONCLUSIONS

This work has highlighted some of the most pressing unresolved issues in stability and strength design of steel-concrete composite framing systems: (1) the large conservative errors that result from neglecting the balance point in the calculation of available strength and (2) the large unconservative errors that result from overestimation of the stiffness for very slender concrete-dominant members subjected to high bending moments. An alternative method of computing the available strength interaction diagram was proposed and evaluated against second-order inelastic analyses for a broad range of cases. The results show that using the proposed interaction diagram reduces the largest conservative errors but worsens existing unconservative errors. To address this issue, an alternative stiffness reduction that varies with internal forces was proposed to better capture the occurrence of high levels of cracking and eliminate the unconservative errors. Initial studies with this alternative stiffness reduction showed promising results. Both alternative approaches, once fully validated, have the potential to improve the accuracy and safety of the stability design provisions for steel-concrete composite framing. They can also set the stage for future developments such as design provisions based on cross-section strength and the use of high-strength materials.

REFERENCES

ACI (2019), *Building Code Requirements for Structural Concrete and Commentary*, American Concrete Institute, Farmington Hills, Mich.

AISC (1986), *Load and Resistance Factor Design Specification for Structural Steel Buildings*, American Institute of Steel Construction, Chicago, Ill.

AISC (2005), *Specification for Structural Steel Buildings*, ANSI/AISC 360-05, American Institute of Steel Construction, Chicago, Ill.

AISC (2016), *Specification for Structural Steel Buildings*, ANSI/AISC 360-16, American Institute of Steel Construction, Chicago, Ill.

AISC (2017), *Steel Construction Manual,* 15th Ed., American Institute of Steel Construction, Chicago, Ill.

ASCE (1997), *Effective Length and Notional Load Approaches for Assessing Frame Stability: Implications for American Steel Design*, American Society of Civil Engineers, Reston, Va.

Behnam, A. and Denavit, M.D. (2020), "Plastic Stress Distribution Method for Predicting Interaction Strength of Steel-Concrete Composite Cross Sections," *Journal of Constructional Steel Research*, Vol. 170, 106092.

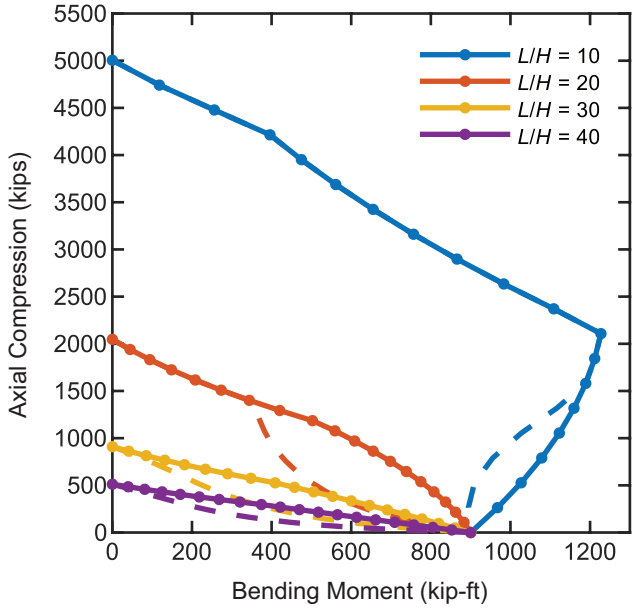

(a) Maximum permitted applied loads with and without the alternative stiffness reduction

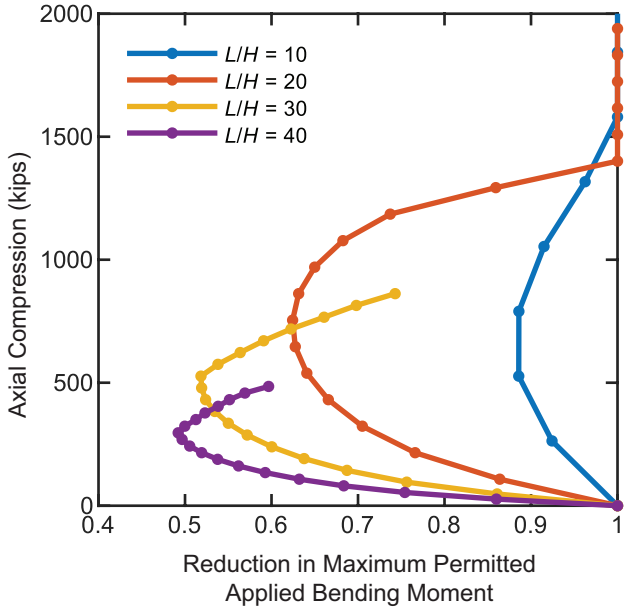

(b) Reduction in maximum permitted applied loads from use of the alternative stiffness reduction

Fig. 8. Results using the alternative stiffness reduction.

Bruneau, M., Kenarangi, H., and Murphy, T.P. (2018), *Contribution of Steel Casing to Single Shaft Foundation Structural Resistance*, NCHRP Research Report 872, The National Academies Press.

CEN (2004), *Eurocode 4: Design of Composite Steel and Concrete Structures—Part 1-1: General Rules and Rules for Buildings*, EN1994-1-1, European Committee for Standardization, Brussels, Belgium.

Denavit, M.D. (2017), "Structural Reliability of Steel-Concrete Composite Columns and Frames," *Proceedings of the 8th International Conference on Composite Construction in Steel and Concrete*, Jackson, Wyo.

Denavit, M.D. and Hajjar, J.F. (2014), *Characterization of Behavior of Steel-Concrete Composite Members and Frames with Applications for Design*, Newmark Structural Laboratory Report Series, Newmark Structural Laboratory Report NSEL-034, University of Illinois at Urbana-Champaign, Urbana, Ill.

Denavit, M.D., Hajjar, J.F., Perea, T., and Leon, R.T. (2016), "Stability Analysis and Design of Composite Structures," *Journal of Structural Engineering*, ASCE, Vol. 142, No. 3, 04015157.

Griffis, L.G. (1992), "Composite Frame Construction," *Constructional Steel Design: An International Guide*, Elsevier Applied Science, London, UK, pp. 523–553.

Griffis, L.G. (2005), "Composite Design Provisions 2005 AISC Specification for Steel Buildings," *Proceedings of the 2005 Structures Congress*, ASCE, New York, N.Y.

Hage, S.E. and MacGregor, J.G. (1974), *The Second-Order Analysis of Reinforced Concrete Frames*, Structural Engineering Report No. 49, Department of Civil Engineering, University of Alberta, Edmonton, Alberta, Canada.

Kanchanalai, T. (1977), *The Design and Behavior of Beam-Columns in Unbraced Steel Frames*, CESRL Report No. 77-2, Structures Research Laboratory, Department of Civil Engineering, The University of Texas at Austin, Austin, Tex.

Lai, Z., and Varma, A.H. (2016). "Effective Stress-Strain Relationships for Analysis of Noncompact and Slender Filled Composite (CFT) Members," *Engineering Structures*, Vol. 124, pp. 457–472.

Lai, Z., Varma, A., and Griffis, L. (2015), "Analysis and Design of Noncompact and Slender CFT Beam-Columns," *Journal of Structural Engineering*, ASCE, Vol. 142, No. 1, 04015097.

SAC (2014), *Technical Code for Concrete Filled Steel Tubular Structures*, GB 50936-2014, Standardization Administration of the People's Republic of China, Beijing, China.

Surovek-Maleck, A.E. and White, D.W. (2004), "Alternative Approaches for Elastic Analysis and Design of Steel Frames. II: Verification Studies," *Journal of Structural Engineering*, ASCE, Vol. 130, No. 8, pp. 1,197–1,205.

Traut-Todaro, J. (2019), "SpeedCore: Lateral System Innovation for Today's Construction Challenges," *Structure Magazine*, November, pp. 12–14.

Wang, Y. and Ziemian, R.D. (2019), "Design by Advanced Elastic Analysis—An Investigation of Beam-Columns Resisting Minor-Axis Bending," *Proceedings of the Annual Stability Conference*, Structural Stability Research Council, St. Louis, Mo.

Lateral-Torsional Buckling Research Needs and Validation of an Experimental Setup in the Elastic Range

RYAN SLEIN, JOSHUA S. BUTH, WAJAHAT LATIF, AJIT M. KAMATH, AMMAR A. ALSHANNAQ, RYAN J. SHERMAN, DAVID W. SCOTT, and DONALD W. WHITE

ABSTRACT

The AISC *Specification* Chapter F I-section member flexural resistance equations are a central part of structural steel design in the United States. The provisions of Sections F4 and F5 address general singly and doubly symmetric I-section members. Analytical studies and experimental tests subsequent to the implementation of these provisions within the 2005 AISC *Specification* suggest that the corresponding inelastic lateral-torsional buckling (LTB) and tension flange yielding (TFY) resistance equations can be improved, resulting in significantly larger predicted strengths in certain cases and somewhat smaller predicted strengths in other cases. Additional large-scale experimental tests, specifically pushing into the inelastic LTB range, need to be conducted to further investigate these predictions. The broad objective of the additional tests is to achieve a target reliability index of $\beta = 2.6$ for building design at a live-to-dead load ratio of 3.0 throughout the design space involving all types of statically determinate I-section flexural members.

This paper discusses the need for these tests, specifically focusing on the details of how the test fixtures and bracing systems were configured to minimize incidental restraint, which is a critical consideration when conducting flexural experimental testing. The paper discusses the validation of the testing system by comparison of elastic buckling experimental results to analytical and numerical solutions.

Keywords: lateral-torsional buckling, experimental testing, incidental restraint.

INTRODUCTION

The Chapter F equations in the AISC *Specification for Structural Steel Buildings*, hereafter referred to as the AISC *Specification* (AISC, 2016b), provide a broad characterization of the flexural resistance of all types of I-section members, including rolled and welded members; members with doubly and singly symmetric cross-section profiles; and members with compact, noncompact, or slender flanges and/or webs, failing by plastic, inelastic, or elastic lateral-torsional buckling (LTB). Closely related equations exist within the *AASHTO LRFD Bridge Design Specifications* (AASHTO, 2020).

Relatively comprehensive assessments of analytical studies and experimental test results conducted to date have raised concerns that AISC *Specification* Sections F4 and F5 flexural resistance provisions may not satisfy accepted target reliability indices in certain cases pertaining to the LTB of I-section members (Subramanian et al., 2018; Subramanian and White, 2017). However, the experimental test data are quite sparse within a number of "regions" of the corresponding design space. Additionally, AISC *Specification* Sections F4 and F5 can be enhanced by eliminating the current tension flange yielding (TFY) limit state provisions. Allowing for development of significant reserve capacity involving yielding in flexural tension by incorporating early tension yielding effects into the calculation of the cross-section yield moment to the compression flange, M_{yc} (Toğay and White, 2018).

Quality experimental data is critical for the validation of refined shell finite element analysis (FEA) procedures that can be employed to investigate the flexural resistances within the design space more comprehensively.

This paper focuses on the validation of the testing configuration used to conduct inelastic tests to achieve the above objectives. Lateral-torsional buckling experimental

Ryan Slein, Graduate Research Assistant, Georgia Institute of Technology, Atlanta, Ga. Email: ryan.slein@gatech.edu (corresponding)

Joshua S. Buth, Civil Engineer II, Georgia Department of Transportation, Atlanta Ga. Email: JButh@dot.ga.gov

Wajahat Latif, Graduate Research Assistant, Georgia Institute of Technology, Atlanta, Ga. Email: wlatif@gatech.edu

Ajit M. Kamath, Graduate Research Assistant, Georgia Institute of Technology, Atlanta, Ga. Email: ajit.kamath@gatech.edu

Ammar A. Alshannaq, Graduate Research Assistant, Georgia Institute of Technology, Atlanta, Ga. Email: aalshannaq@gatech.edu

Ryan J. Sherman, Assistant Professor, Georgia Institute of Technology, Atlanta, Ga. Email: ryan.sherman@ce.gatech.edu

David W. Scott, Professor and Chair, Department of Civil Engineering and Construction., Georgia Southern University, Statesboro, Ga. Email: dscott@georgiasouthern.edu

Donald W. White, Professor, Georgia Institute of Technology, Atlanta, Ga. Email: dwhite@ce.gatech.edu

Paper No. 2020-12

results can be sensitive to incidental restraint in the testing configuration (Ziemian, 2010). The testing configuration described in this paper utilizes polytetrafluoroethylene-(PTFE-) coated spherical bearings for multi-rotational degree-of-freedom releases, mechanical bearings for the single rotational degree-of-freedom releases (as part of a Watt's linkage bracing system), and lubricated roller packs for single translational degree-of-freedom releases. The effectiveness of these "releases" of rotational and translational constraints is evaluated directly by testing a specimen in the elastic LTB range and comparing the measured responses to various analytical and numerical solutions.

TEST CONFIGURATION

The experimental test setup was designed to minimize incidental restraint and remove load-height effects. Incidental restraint can have a measurable impact on large-scale experimental LTB beam results by increasing the capacity beyond that based on the ideal boundary conditions (Ziemian, 2010). The test configuration was designed to fully release or fix selected degrees-of-freedom at the bearing, load, and bracing points. Load-height effects at the load points can make the calibration of design equations to observed specimen behavior more complex. To eliminate load-height effects, the lateral and torsional displacements were restrained at the bearing and load points in all the experiments conducted in this research. The design of the test setup involved an extension of the concepts discussed in the Structural Stability Research Council (SSRC) Technical Memorandum No. 9 on flexural testing (Ziemian, 2010).

Figure 1 provides an elevation view of a test specimen, discussed throughout this paper, under three-point bending. The elevation view and measured section dimensions in Figure 1 are drawn to scale and show instrumentation locations and the corresponding moment diagram.

Figure 2 is a photograph of the test specimen within testing frame. The white member is the test specimen, the blue members are the bracing reaction system, and the gray members are the load frame. The loading and support fixtures and bracing details are discussed in the following sections.

Load and Bearing Fixtures

Roller boundary conditions were provided at the bearing locations. The overall boundary conditions were symmetric about the mid-length of the test specimens. Longitudinal translation was permitted via a lubricated roller pack composed of four 2.5-in.-diameter solid steel rods. A 100-kip load cell was located above each roller pack. Transverse displacement was restrained at the bearing locations via Watt's linkage braces discussed in the following section. The three rotational degrees-of-freedom at the supports were released via PTFE-lined spherical thrust bearings. The PTFE thrust bearings allowed free in-plane rotation due to the major-axis bending of the specimens and free out-of-plane rotation associated with flange warping and/or lateral bending. The spherical bearing was seated in a counter-bored plate on top of the load cell. Weld beads were placed on the flange of the specimen to securely seat the opposite side of the spherical bearing on the specimen. Figure 3 provides a conceptual drawing of the bearing detail used for all tests as well as a photograph of the final bearing detail prior to placing the spherical thrust bearing at the top.

In addition, a PTFE spherical thrust bearing was located at the point of load application (e.g., at the midspan of the three-point bending test specimens). Load-point bracing was provided via a Watt's linkage system. Figure 4 shows the conceptual and implemented boundary condition at the point of load application.

Bracing

The bracing system was designed using a mechanical system known as a Watt's linkage. The Watt's linkage restrains displacement perpendicular to the girder web, while allowing

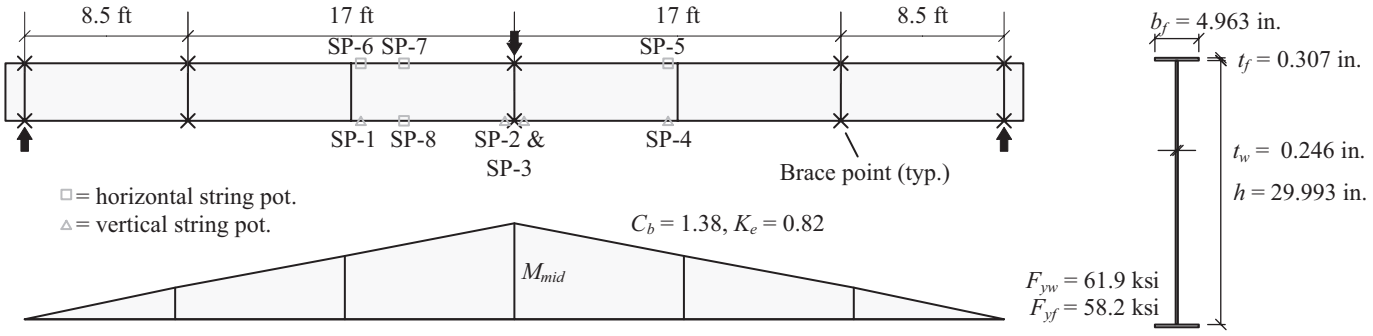

Fig. 1. South-facing elevation view of the elastic test specimen showing the instrumentation locations, corresponding moment diagram, measured section dimensions and properties, and key design parameters C_b *and* K_e.

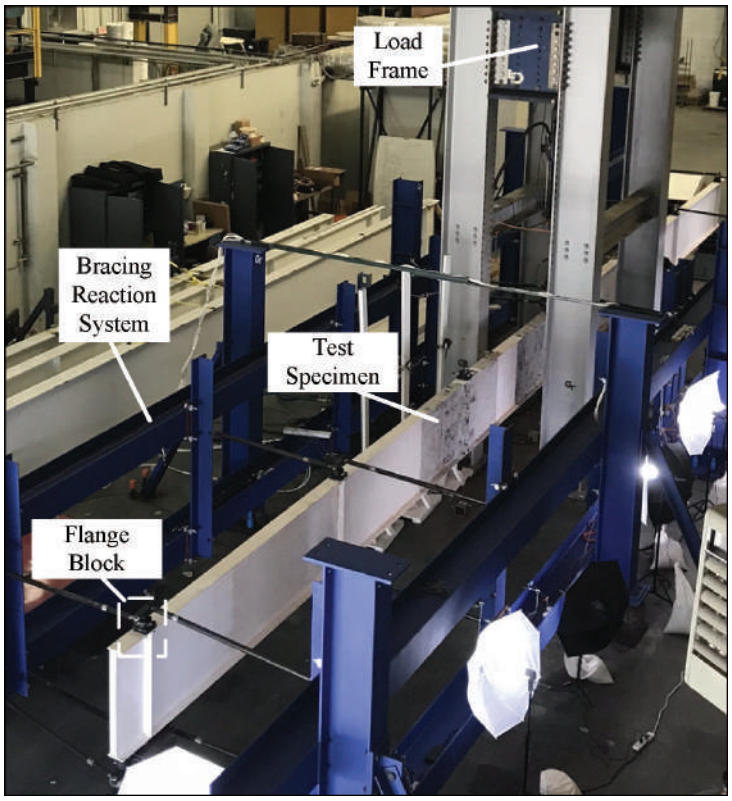

Fig. 2. Perspective view of the test configuration.

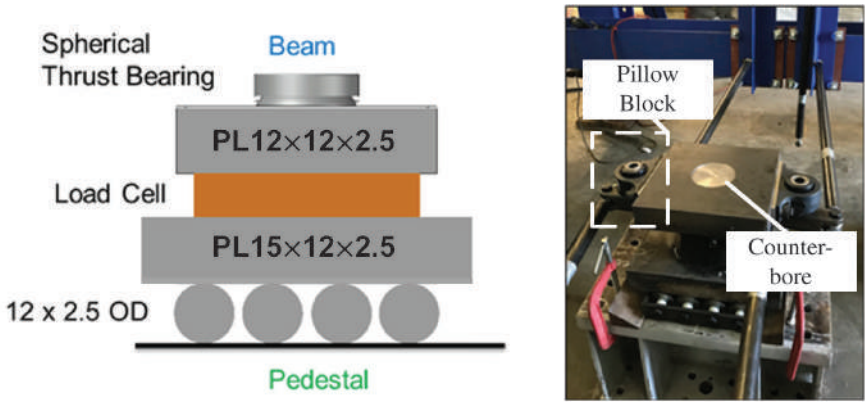

Fig. 3. Bearing boundary condition detail: schematic (left) and implementation (right). The spherical bearing was excluded in the photo to show the counter-bore. The roller pack was chocked in the photo to prevent incidental movement during installation of the test specimen.

free translation in the longitudinal and vertical directions. Watt's linkage bracing has been used previously by Yarimci et al. (1967), Smith et al. (2013), and others. For the current study, the system was comprised of two 4-ft-long tie rods with ball joint rod ends attached to the stiff reaction frames (painted blue in Figure 2) and a 6.5-in.-long center link. The center link is free to rotate about a vertical axis and transfers lateral forces to the girder through a cylindrical mechanical bearing referred to as a flange block. The center link is attached at its mid-length to a pillow block on each side of the 2.5-in.-thick plate containing the counterbore at the load and support points and to a flange block at the other brace points. Figure 5 illustrates the ability of the linkage system to prevent deflections in the direction perpendicular to the girder webs (i.e., the horizontal direction in the figure) under large longitudinal displacements (i.e., displacements in the vertical direction in the figure). In addition, girder vertical deflections (i.e., deflections into and out of the page in the figure) are accommodated by the rotation of the center link about a vertical axis.

The Watt's linkage system does an excellent job of releasing incidental constraint. Annotated photos describing the system are provided in Figure 6 and 7. Several additional unique features added to the design of the bracing system include the following:

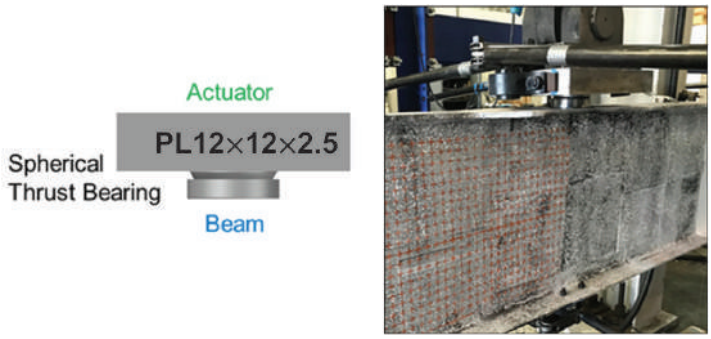

Fig. 4. Load point boundary condition detail: schematic (left) and implementation (right).

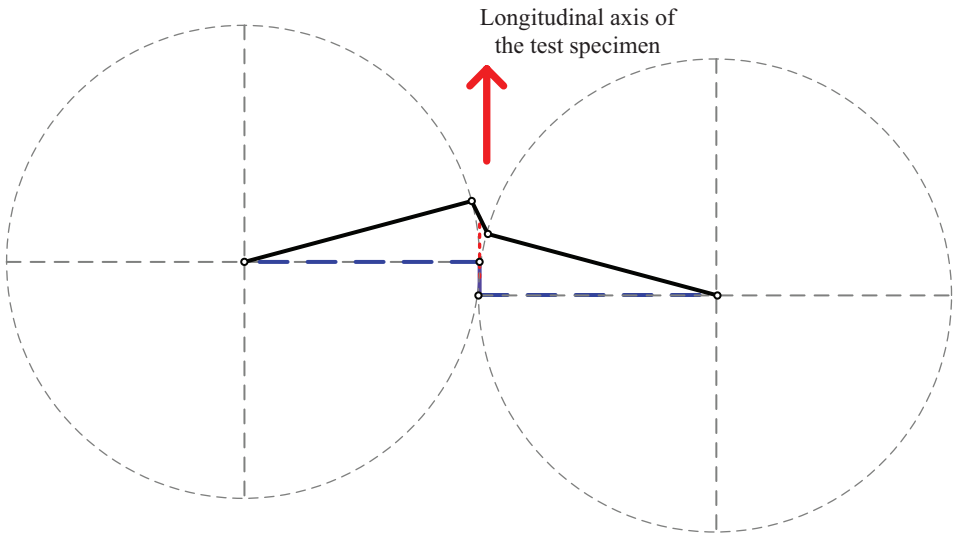

Fig. 5. Plan view illustration of a Watt's linkage movement under a large deflection along the axis of the test specimen. The heavy dashed blue lines represent the initial geometry of the linkage, the solid black lines represent a deformed geometry of the linkage, and the red dashed line illustrates the path of the brace point (i.e., the middle of the center link) between the two geometries.

- Each end of the tie rods was threaded—left-hand threads on one end and right-hand threads on the other. The opposing threads allowed for quick length adjustments via rotation of the rod about its axis, without having to unbolt the ends, allowing for fine adjustments to ensure the test specimen was plumb at each brace point.
- Jam nuts were used to ensure the tie rod length did not change during the loading of the test specimens.
- A rail system was implemented for rapid reconfiguration between different unbraced lengths and bracing configurations. The tie rods were bolted to vertical WT members containing a series of holes accommodating varying specimen heights. The bracing reaction frame was composed of wide flange rails that extended the entire length of the test setup. Friction-based connections by Lindapter (2019) were used to connect the vertical WT sections to the wide flange rails. Each WT slid along the rails to accommodate a range of specimen unbraced lengths.
- Each brace point, including the Lindapter friction-based connection, was designed to accommodate a transverse force of 20 kips. A flange block (a housed cylindrical bearing) was used to release the rotation about the vertical axis at the girder flanges for the Watt's linkage system. At the load application and bearing locations, pillow blocks, with a different housing but the same internal cylindrical bearing, were selected. To prevent pull-out, the outside diameter of the stem connecting the center link to the pillow block was match-machined to the inside diameter of the bearing for a press-fit connection. Additionally, four set screws bear on flats on the center-link stem.

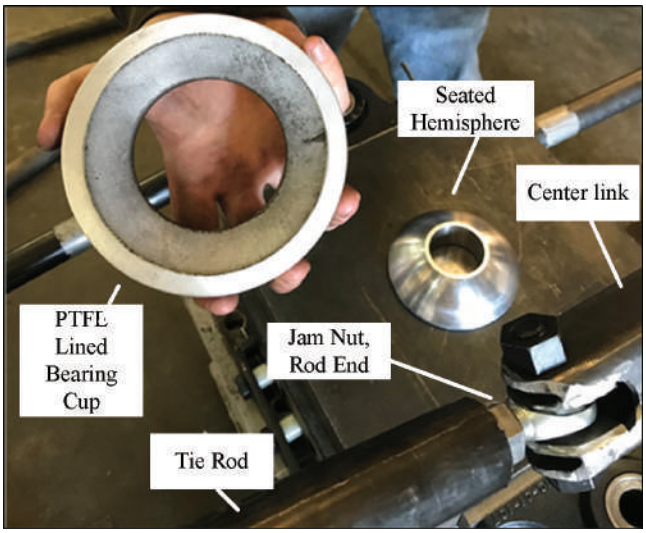

Fig. 6. Components of the boundary conditions.

NUMERICAL MODELING

Finite element methods can predict incipient buckling (bifurcation) by calculating the lowest eigenvalue using the equation

$$\left[K_{e.ff}\right]\left\{\Delta_f\right\} = \lambda\left[-K_{g.ff}\right]\left\{\Delta_f\right\} \quad (1)$$

where $K_{e.ff}$ is the elastic stiffness matrix only considering free degrees of freedom, $K_{g.ff}$ is the geometric stiffness matrix calculated from element forces (or stresses) from a linear elastic analysis for a known reference load P_{ref}, Δ_f is the displacement vector associated with the free degrees of freedom, and λ is the lowest eigenvalue representing the ratio of the elastic critical load to P_{ref} (McGuire et al., 2000).

Iterating P_{ref} until λ goes to 1.0 results in a predicted elastic linear buckling strength. For the test specimens, self-weight and the weight of the bracing components are a constant value, so it is inappropriate to scale a constant reference applied load, P_{ref}, solely by λ. That is, the loading on the system includes a constant load due to the initial self-weight of the specimen and bracing attachments to the specimen, plus the reference load multiplied by the applied load parameter, λ. Once the initial load due to the self-weight is established, then either P_{ref} can be varied and an eigenvalue solution sought such that $\lambda = 1.0$, or a constant applied reference load can be specified and an eigenvalue multiple of this reference load sought corresponding to the buckling of the specimen. In either case, the internal forces are the sum of the constant forces due to the initial

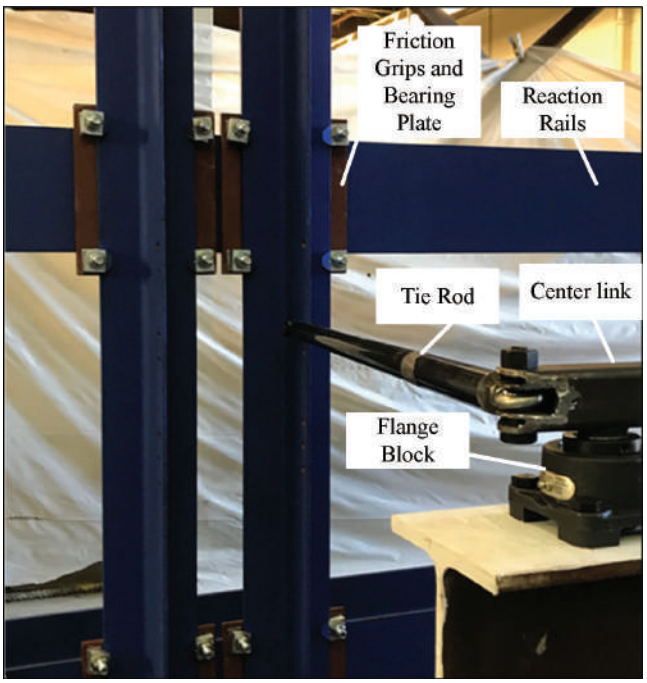

Fig. 7. Components of the bracing system.

self-weight plus the forces due to the additional applied load at buckling. In this research, these elastic buckling calculations were conducted using the finite element software system SABRE2 (White et al., 2020) based on thin-walled open-section (TWOS) beam theory considering warping torsion.

The elastic effective length factor, K_e, is back-calculated by equating the maximum internal moment within the critical unbraced length, at the elastic buckling load level determined by the computational solution, to the equation for the elastic critical moment, M_{cr}, from recommended and AISC *Specification* (2016b) provisions:

$$M_{cr} = \frac{C_b S_{xc} \pi^2 E}{\left(K_e L_b / r_t\right)^2} \sqrt{1 + 0.078 \frac{J}{S_{xc} h_o} \left(\frac{K_e L_b}{r_t}\right)^2} \qquad (2)$$

An expedient process to determine K_e is to employ the goal-seek root-finding capability in Excel to iteratively solve for the value of K_e that satisfies the equality.

In Equation 2, C_b is the moment gradient factor, E is the elastic modulus, S_{xc} is the section modulus, L_b is the unbraced length of the critical section, r_t is the radius of gyration for LTB, J is the St. Venant torsion constant, and h_o is the distance between the flange centroids. For the slender-web members, J was taken equal to zero in Equation 2, as well as in the calculation of the buckling load from SABRE2. The calculated value of K_e is used in all recommended and AISC *Specification* strength calculations of this research to directly account for the end restraint from adjacent less-critical unbraced lengths due to continuity effects. An alternative means of calculating K_e is to use an approximate method such as that proposed by Nethercot and Trahair (1976). However, with the increased availability of software capable of conducting basic elastic linear buckling analysis (ELBA), the "exact" calculation of K_e is the more appropriate solution for research evaluations.

ABAQUS Version 6.13 (Simulia, 2021) finite element analysis software was employed for developing GMNIA (geometric nonlinear material linear-elastic analysis with imperfections) finite element simulations in this research. The finite element mesh consisted of B31 beam elements for transverse stiffeners and S4R nonlinear shell elements for all other components. The B31 is a two-node, three-dimensional beam element that allows for transverse shear deformation. The B31 element is based on linear-order displacement interpolation and is compatible with the S4R shell element. The S4R is a four-node, quadrilateral displacement-based shell element with reduced integration. Both the B31 and the S4R elements are based on large-strain formulations. The shell finite element mesh for the I-section specimens was generated using 12 elements across the flange width and a minimum of 16 elements through the web depth. The dimension of the shell elements along the length of the members was selected such that the aspect ratio of the web elements was close to 1.0. This mesh density has been determined to be sufficient for convergence of full nonlinear FEA solutions of various I-section members in prior research—for example, Prado and White (2015)—as well as in these research studies.

The nonlinear shell FEA solutions in ABAQUS were implemented through a modified RIKS arc length procedure. The modified RIKS algorithm is particularly useful in obtaining the post-buckling response for cases where the loading is proportional—that is, where the load magnitudes are governed by a single parameter (Simulia, 2021). The modified RIKS algorithm conducts a load-deflection analysis where the load is incremented by scaling the reference load, or a set of applied reference loads, by the load parameter. The definition of initial residual stresses, and the application of the applied loads to the test specimens starting from their loaded state under their self-weight, was accomplished by subdividing the analysis into multiple steps. Note that the residual stress pattern follows half the magnitude of the best-fit Prawel pattern based on recommendations from Subramanian and White (2017), who state that this provides reasonable correlation with the mean results from experimental tests. A first step was employed to solve for the equilibration of the initial residual stresses on the geometrically imperfect model (the initial residual stress pattern generally does not satisfy equilibrium on the imperfect structure geometry, nor at free-ends of the specimens). A second step was then employed to apply the constant self-weight loads. Finally, the modified RIKS algorithm was applied in a third step to place the applied load incrementally on the model.

VALIDATION OF THE TEST SETUP THROUGH AN ELASTIC LTB TEST

A benchmark elastic LTB experiment was conducted to evaluate the effectiveness of the translation and rotational releases in the test setup. Figure 1 provides an elevation view of the test specimen as well as the moment diagram. The elevation view and measured section dimensions in Figure 1 is drawn to scale and shows instrumentation locations. For the critical unbraced lengths adjacent to the mid-span, C_b = 1.38 from AISC *Specification* Commentary Equation C-F1-2b (AISC, 2016b) and K_e = 0.82 for the critical unbraced lengths adjacent to the mid-span (back-calculated from an elastic buckling analysis conducted using SABRE2). The resulting configuration slenderness was well within the elastic LTB range.

It is important to note that due to stable elastic post-buckling response in the governing LTB mode, the specimen potentially can develop a maximum load capacity larger than the elastic critical load, due to the large LTB

slenderness for the elastic LTB testing arrangements. Any actual post-buckling strength is directly dependent upon the extent of early yielding due to the combined effects of the girder loads, the initial geometric imperfections, the initial residual stresses, and the amplified lateral bending of the compression flange as the theoretical elastic critical load is approached. The peak load at which the elastic LTB test reached is compared directly to the theoretical elastic LTB resistance and to the capacity predicted from shell FEA test simulation. The FEA simulation models included the evaluation of the post-peak response. Additionally, plots of the horizontal displacement of the flanges versus the load were employed to estimate the theoretical elastic LTB moments via Southwell, Meck, and Massey plots (Mandal and Calladine, 2002).

The test specimen was fabricated by a prominent metal building manufacturer and is representative of main frame members in typical metal building frames. The web-to-flange welds are minimum size single-sided fillet welds. Both flanges are fabricated from rolled bar stock, while the web was cut from a coil. In addition, the specimen has double-sided stiffener plates at all the brace points, including load and bearing locations, to control cross-sectional distortion.

Measured compression flange sweep and web out-of-flatness of the test specimen are shown in Figures 8 and 9, respectively. Geometric imperfection measurements were taken after the beam was installed and plumbed. Allowable tolerances of $L_b/480$ for compression flange sweep and $h/72$ for web out-of-flatness are specified in the *Metal Building*

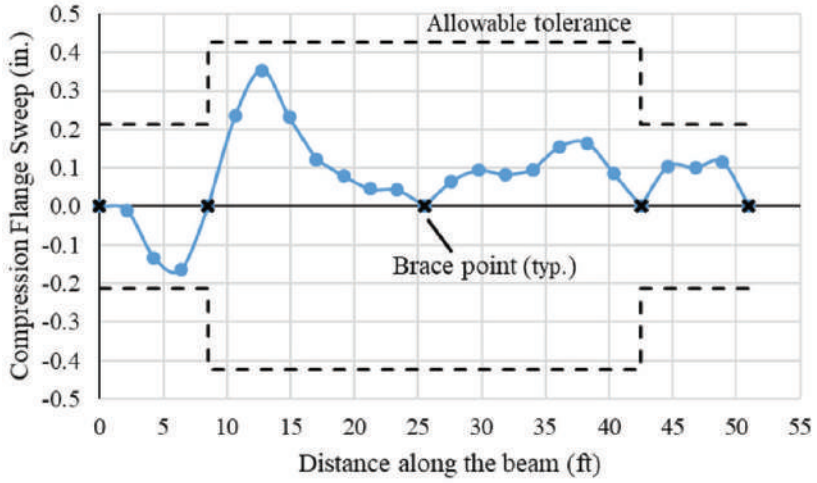

Fig. 8. Measured compression flange sweep.

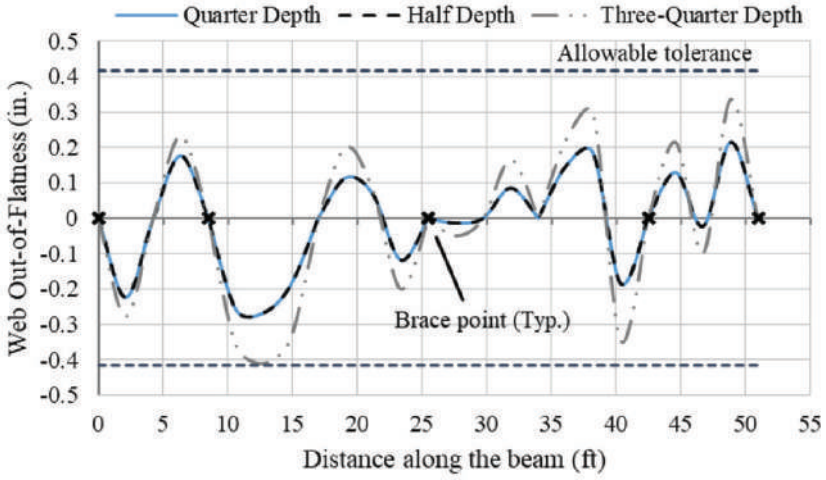

Fig. 9. Measured web out-of-flatness.

Table 1. Peak Moment Contributions		
Maximum Moment at Mid-Span Due to Dead Loads		
Dead Load	**Calculation**	**Moment kip-ft (kip-in.)**
Girder self-weight	(0.036 klf) (51 ft)^2/8	11.6 (139)
Mid-span attachments	(0.38 kip) (51 ft)/4	4.95 (59.4)
Bracing attachments	(0.07 kip) (8 ft)	0.540 (6.50)
Maximum Moment at Mid-Span Due to Applied Loads		
Applied Load	**Calculation**	**Moment kip-ft (kip-in.)**
Initial seating preload	(0.50 kip) (51 ft)/4	6.38 (76.5)
Actuator load at failure	(8.51 kips) (51 ft)/4	109 (1300)
	Maximum moment at mid-span	133 (1600)

Systems Manual (MBMA, 2018). These tolerances are approximately double the imperfection limits given by the AISC *Code of Standard Practice* (AISC, 2016a). The other measured imperfections—that is, tension flange sweep, combined flange warpage and tilt, and web off-center—were documented but are not specified in this paper. A detailed force and moment tabulation is summarized in Table 1, including the influence of all self-weights of the testing specimen and bracing components, load applied prior to zeroing the load cells at the start of the experiment, and the measured peak load during the experiment.

The experimental strength of 1,600 kip-in. is normalized by the moment corresponding to compression flange yielding, M_{yc}, of 4,760 kip-in. and plotted in Figure 10 at the effective length, K_eL_b = 13.9 ft. Furthermore, Figure 10 shows numerical strength predictions from an ABAQUS nonlinear shell FEA test simulation and from a thin-walled open-section (TWOS) beam theory inelastic buckling analysis using SABRE2, as well as estimates of the theoretical elastic buckling load from a Southwell plot based on the measured experimental displacements.

In addition, Figure 10 shows the normalized theoretical elastic buckling curve from Equation 2 for a range of members having the same configuration as in Figure 1 but with different effective unbraced lengths, using the calculated finite J for the specific specimen. This is the dashed black curve in the figure. Also shown in light gray is the LTB strength curve from the recommended provisions presented in Slein et al. (2021). This curve is based on $J = 0$ since the web for this cross section classifies as slender using

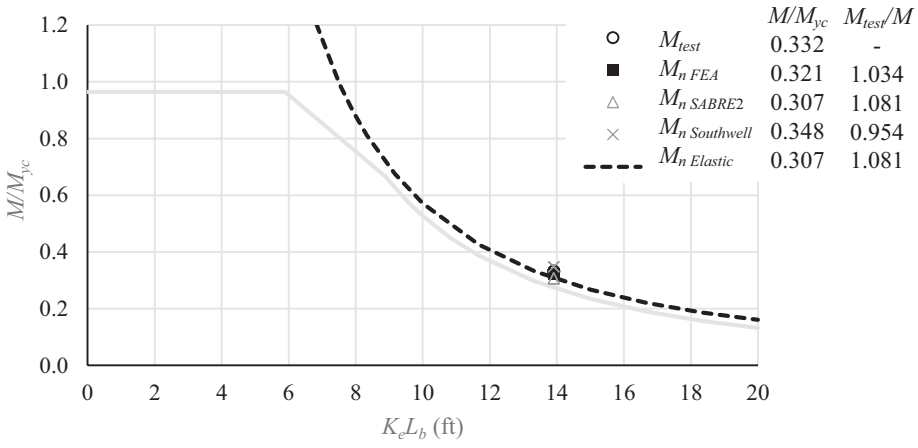

Fig. 10. Comparison of experimental test results to numerical results from ABAQUS and SABRE2 to a Southwell plot estimate of the elastic buckling load and to elastic LTB and design strength curves.

the recommended provisions. The "exact" elastic critical moment for the specimen is determined using SABRE2, and the K_e value is determined using Equation 2 (using the solution based on $J = 0$ for this member because its web is classified as slender in the recommended provisions).

Figure 11 shows the measured moment versus vertical displacement for SP-2, overlaying the predicted moment-maximum vertical displacement from the shell FEA. Figure 12 shows the measured moment versus lateral displacements for SP-7 and SP-8, overlaying the predicted moment-maximum horizontal displacement of the compression flange and the corresponding horizontal displacement of the tension flange from the shell FEA. Figure 13 shows the measured moment versus section twist at the cross section where SP-7 and SP-8 are attached, overlaying the predicted moment-twist from the shell FEA.

The GMNIA solution from ABAQUS is capable of capturing a capacity in the elastic test that is larger than the theoretical elastic LTB strength due to the stable elastic post-buckling response of the member. The contributions from elastic post-buckling strength are negligible for most practical LTB slenderness values; however, given the large slenderness in this elastic LTB test, strengths larger than the theoretical elastic LTB resistance are possible. Figure 14 shows the midspan moment versus the compression flange lateral deflection from the GMNIA solution, a shell

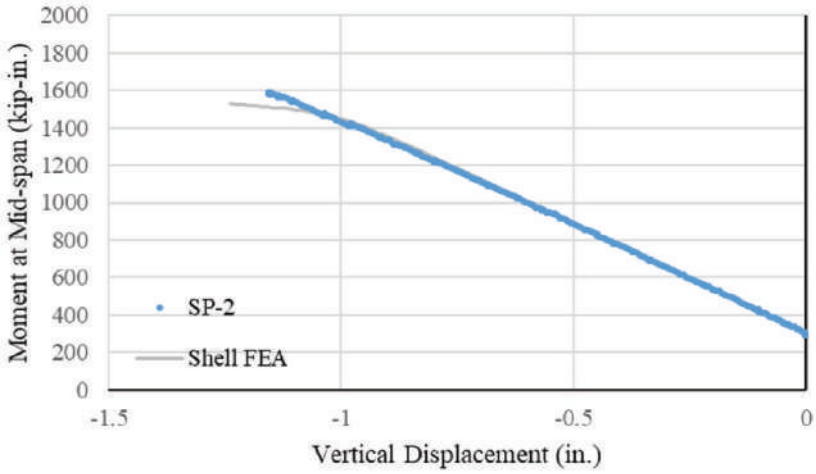

Fig. 11. Moment-vertical deflection.

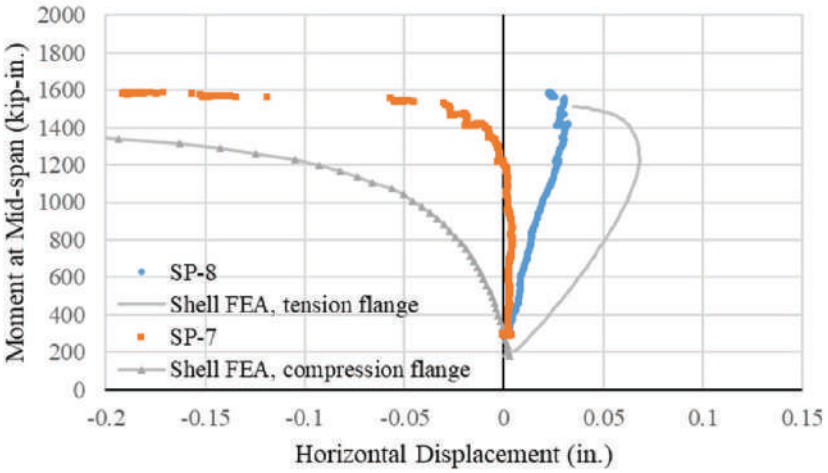

Fig. 12. Moment-horizontal deflection of both flanges.

FEA geometric nonlinear (material linear-elastic) analysis with imperfections using the same model as in the GMNIA solution (referred to in the literature as a GNIA solution), and the ELBA solution obtained from SABRE2.

As the theoretical elastic critical moment is approached, the compression flange lateral displacement increases rapidly, both in the full nonlinear (GMNIA) and the geometrically nonlinear (GNIA) shell FEA solutions. The corresponding rapid increase in the compression flange lateral bending strains induces the onset of yielding within the compression flange, resulting in a limit load in the GMNIA solution. This behavior was observed during the experiment, that when the rate of change of the compression flange lateral displacements increases abruptly, the member was very close to maximum capacity. The second-order amplifications of the girder lateral displacements and twists in the experiment matched well with the theory.

Experimental Estimation of Elastic Buckling Load by Southwell, Meck, and Massey Plots

As a final evaluation of the test setup effectiveness—specifically the minimization of incidental restraint—measured displacements and loads were used to generate Southwell, Meck, and Massey plots for the elastic tests. These plots allow estimation of the elastic critical moment

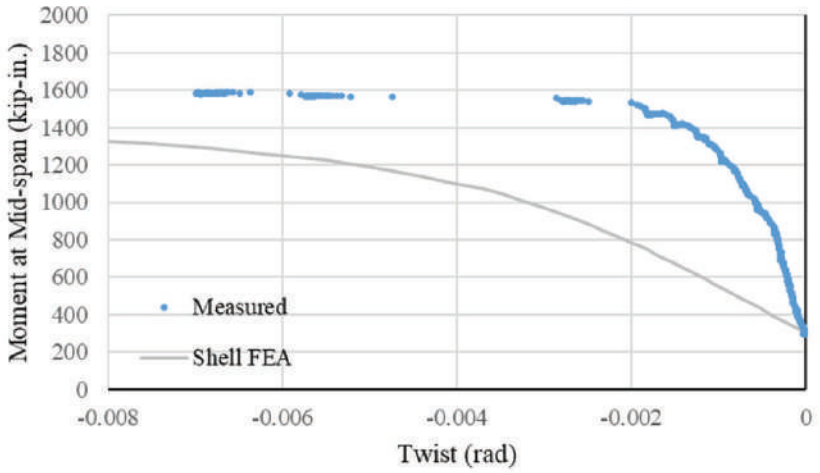

Fig. 13. Moment-twist of the section.

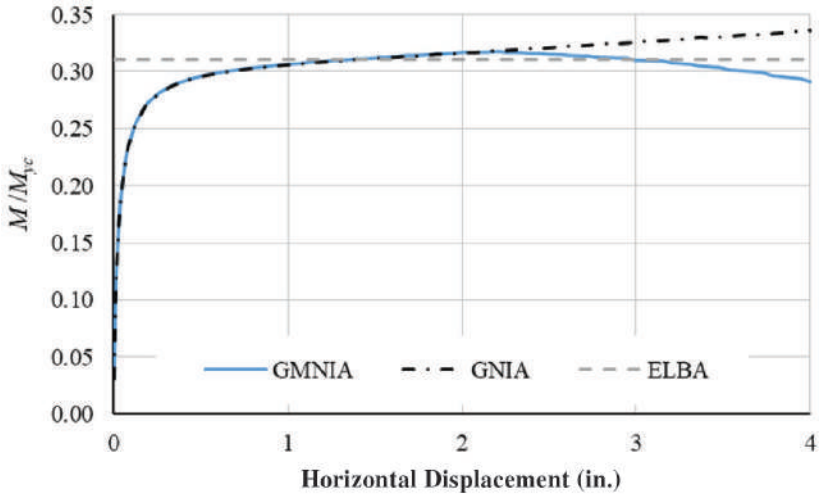

Fig. 14. Load-horizontal displacement curves from ABAQUS GMNIA and GNIA solutions compared to the ELBA solution from SABRE2.

of the specimen, M_{cr}. Mandal and Calladine (2002) discuss the effectiveness and theoretical underpinnings of these plots for LTB problems. Each of the methods plot a variation of a displacement divided by a load term versus displacement, then use the inverse of the slope of this curve to estimate M_{cr}. The authors interpreted the application of the different estimation methods as described in the following discussion.

The Southwell plot for LTB was generated using the lateral displacement of the compression flange, u, as the abscissa versus u/M as the ordinate. The lateral displacement was measured using a linear string potentiometer, located at the expected position of the maximum compression flange lateral displacement. The estimate is not sensitive to the specific selected location as long as the magnitude of the instrumentation noise is low compared to the magnitude of the measurement. The maximum moment at mid-span was calculated as

$$M = \frac{PL}{4} + M_o \tag{4}$$

where P is the summation of load cell measurements at the end supports, L is the distance between the end supports, and M_o is the mid-span dead load moment. Figure 15 shows the resulting Southwell plot for the elastic test.

The Meck plot was similar to the Southwell plot, but it also considers the twist of the cross section, φ. During the elastic test the tension flange had negligible out-of-plane motion, as shown in Figure 12; therefore, the twist of the cross section is directly proportional to the lateral displacement of the compression flange. The Meck plot takes M_{cr} as the square root of the product of α (the inverse slope of φ/M versus u) and β (the inverse slope of u/M versus φ)—that is, the geometric mean of α and β,

$$M_{cr} = \sqrt{\alpha\beta} \tag{5}$$

The Massey plot takes M_{cr} as the geometric mean of α (taken as the inverse slope of φ/M^2 versus φ), and β (taken as the inverse slope of u/M^2 versus u). The values of α and β for the Meck and Massey plots are defined by the slope of the corresponding plots, similar to M_{cr} on the Southwell plot. There is some complexity that is not captured by these methods since the critical unbraced lengths of the specimen are not flexurally and torsionally simply supported. As such, the second-order amplifications of the compression flange lateral deflection, u, and the twist, φ, do not have the same mathematical form as that of a simply supported column (for that matter, they do not have the same form when the LTB specimen is torsionally and simply supported, which leads to the consideration of the alternative estimation procedures other than the basic Southwell plot). However, the methods agree reasonably well with each other for the elastic test. In the limit that the moment approaches the theoretical elastic buckling moment, it appears that the simple assumptions for the form of the second-order amplification of the displacements, embedded within the Southwell, Meck, and Massey plots, apply reasonably well. The calculated maximum moments are 1,660 kip-in. ($0.348M_{yc}$), 1,640 kip-in. ($0.344M_{yc}$), and 1,570 kip-in. ($0.329M_{yc}$) from the Southwell, Meck, and Massey procedures, respectively. These theoretical estimates show good agreement with the maximum moment of 1,600 kip-in. measured in the experiment.

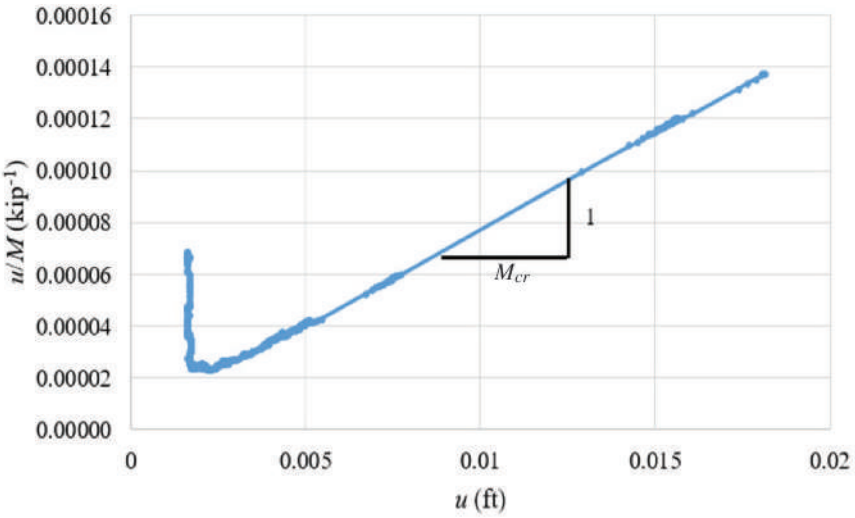

Fig. 15. Southwell plot.

QUANTIFICATION OF INCIDENTAL RESTRAINT

To quantify the ability of the testing system to minimize incidental restraint, the buckling load solutions from Southwell, Meck, and Massey are compared with the result from an elastic linear buckling analysis (ELBA). The effective length in the theoretical elastic buckling solution is back-calculated directly from an ELBA in SABRE2, so the theoretical elastic buckling solution from Equation 2 and the SABRE2 ELBA are the same. The reported SABRE2 solutions are from an inelastic nonlinear buckling analysis (INBA). Note that K_eL_b in the elastic test is much larger than L_r; therefore, the major-axis bending moment is at a level where there is not a significant onset of yielding prior to reaching the maximum capacity, resulting in a similar INBA solution as ELBA. Structural steels such as ASTM A572 Grade 55 generally have a mean elastic modulus close to 29,500 ksi with a small coefficient of variation (Hartmann, 2005). Using this larger elastic modulus in the ELBA solution gives a more accurate representation of the physical response. The elastic critical moment scales by 29,500/29,000 given this change.

For the elastic test, the Southwell, Meck, and Massey estimates give M_{cr}/M_{yc} ranging from 0.329 to 0.348. The ELBA eigenvalue result from SABRE2, with E = 29,500 ksi, gives M_{cr}/M_{yc} of 0.312. Therefore, in terms of elastic buckling load, the test shows an influence of incidental constraint of 5 to 12%, depending on which estimates are used for determining the elastic critical moment experimentally.

To a lesser extent, the ability of the testing system to minimize incidental restraint can be quantified by comparing the experimental load to the shell FEA load-deflection solution. The M_{test}/M_{nFEA} value was 1.03 for the elastic test. However, the elastic test was halted prior to reaching the limit load (when the compression flange lateral bending started to increase significantly) to ensure that no significant yielding occurred, since the specimen is subsequently used for an inelastic LTB test, resulting in slightly low measured experimental strengths. This is more of a problem when KL_b is in the proximity to L_r, due to the greater propensity for the onset of yielding due to the addition of amplified flange lateral bending stresses as the theoretical elastic buckling load was approached. Additionally, potential overprediction of M_{nFEA} can be a source of error. The shell FEA test simulation potentially could have overpredicted the strength, for example, by its use of one-half of the best-fit Prawel residual stress profile (i.e., by assuming residual stresses that are relatively small and symmetric about the mid-width of the flanges), as well as by excluding the web off-center imperfections in the modeling of the specimen geometry, in this test. The maximum strength obtained in the FEA solution can be sensitive to variations in the residual stresses and geometric imperfections when the compression flange major-axis bending stress is relatively large at the LTB strength condition. The expected sensitivities of M_{test} and M_{nFEA} to the residual stresses and geometric imperfections when KL_b is close to L_r, and the uncertainties in the precise values of these quantities, makes the use of M_{test}/M_{nFEA} less of a useful measure of incidental constraint within the testing system.

CONCLUSIONS

Incidental restraint can have a measurable impact on experimental LTB test results. Substantial attention was given to minimizing the constraint in the experimental setup described in this paper. The setup design consists of ideally released degrees of freedom, while restraining specified degrees of freedom, using mechanical bearings in a Watt's linkage bracing system. PTFE spherical thrust bearing allowed for free flange lateral bending and major-axis and weak-axis rotation. Complications of load height were bypassed with placing stiffeners at points of load application and bearing, along with a lateral brace of both flanges. For an accurate comparison to strength predictions, numerical solutions were modeled to be representative of the physical specimen and manual predictions utilized a rigorously calculated effective length factor.

To validate the effectiveness of the testing setup, an elastic LTB test was conducted and compared to analytical and numerical predictions, as well as to theoretical elastic critical moment estimates. The most direct prediction of the effectiveness of the setup is believed to be the comparison of the buckling load solutions from Southwell, Meck, and Massey to an elastic linear buckling analysis. Resulting data indicated an influence from incidental restraint on the LTB strength ranging between 5 and 12%, depending on the methodology. The nominal difference can be attributed to the small amount of remaining restraint as well as other factors influencing the predictions, such as discrete measurements of plate dimensions, material properties, and geometric imperfections. Ultimately, the results demonstrate the designed test configuration minimizes incidental constraint, resulting in accurate experimental LTB test data.

ACKNOWLEDGMENTS

The authors would like to acknowledge MBMA, AISC, and AISI for their generous support of this research; American Buildings Company, BlueScope Buildings North America, and Schulte Building Systems for their generous donations

of the test specimens; AISC and NUCOR Fastener Division for material and fastener donations; and Thomas Murray of Virginia Tech for acting as the MBMA senior advisor to the project. They would also like to thank the Georgia Tech Structural Engineering Laboratory staff and other GT personnel for their many contributions to the project.

REFERENCES

AASHTO (2020), *AASHTO LRFD Bridge Design Specifications*, 8th Ed., American Association of State and Highway Transportation Officials, Washington, D.C.

AISC (2005), *Specification for Structural Steel Buildings*, ANSI/AISC 360-05, American Institute of Steel Construction, Chicago, Ill.

AISC (2016a), *Code of Standard Practice for Steel Buildings and Bridges*, ANSI/AISC 303-16, American Institute of Steel Construction, Chicago, Ill.

AISC (2016b), *Specification for Structural Steel Buildings*, ANSI/AISC 360-16, American Institute of Steel Construction, Chicago, Ill.

Hartmann, J.L. (2005), "An Experimental Investigation of the Flexural Resistance of Horizontally Curved Steel I-Girder Systems," Doctoral Dissertation, University of Maryland, College Park, Md.

Lindapter (2019), *Steel Connections Catalog*, Lindapter USA, http://www.lindapter.com/ (April 22).

Mandal, P. and Calladine, C.R. (2002), "Lateral-Torsional Buckling of Beams and the Southwell Plot," *International Journal of Mechanical Sciences*, Vol. 44, No. 12, pp. 2,557–2,571.

MBMA (2018), *Metal Building Systems Manual*, Metal Building Manufacturers Association, Cleveland, Ohio.

McGuire, W., Gallagher, R., and Ziemian, R.D. (2000), *Matrix Structural Analysis*, 2nd Ed., Wiley, New York, N.Y.

Nethercot, D.A. and Trahair, N.S. (1976), "Lateral Buckling Approximations for Elastic Beams," *Structural Engineering*, Vol. 54, No. 6, pp. 197–204.

Prado, E.P. and White, D.W. (2015), "Assessment of Basic Steel I-Section Beam Bracing Requirements by Test Simulation," Structural Engineering, Mechanics and Materials Report, School of Civil and Environmental Engineering, Georgia Institute of Technology, Atlanta, Ga.

Simulia (2021), Abaqus 6.13, Dassault Systems, https://www.3ds.com/products-services/simulia/services-support/support/documentation/ (February 22).

Slein, R., Kamath, A.M., Latif, W., Phillips, M.L., Sherman, R.J., Scott, D.W., and White, D.W. (2021), "Enhanced Characterization of the Flexural Resistance of Built-up I-Section Members," SEMM Research Report 21-01, School of Civil and Environmental Engineering, Georgia Institute of Technology, Atlanta, Ga.

Smith, M.D., Turner, A.K., and Uang, C.-M. (2013), "Experimental Study of Cyclic Lateral-Torsional Buckling of Web-Tapered I-Beams," Department of Structural Engineering University of California, San Diego, Calif.

Subramanian, L., Jeong, W.Y., Yellepeddi, R., and White, D.W. (2018), "Assessment of I-Section Member LTB Resistances Considering Experimental Tests and Practical Inelastic Buckling Design Calculations," *Engineering Journal,* AISC, Vol. 55, No. 1, pp. 15–44.

Subramanian, L. and White, D.W. (2017), "Resolving the Disconnect between Lateral Torsional Buckling Experimental Tests, Test Simulations and Design Strength Equations," *Journal of Constructional Steel Research*, Vol. 128, pp. 321–334.

Toğay, O. and White, D.W. (2018), "Toward the Recognition of Unaccounted for Flange Local Buckling and Tension Flange Yielding Resistances in the ANSI/AISC 360 Specification," *Proceedings of the SSRC Annual Stability Conference*, Baltimore, Md.

White, D.W., Toğay, O., Slein, R., and Jeong, W.Y. (2020), "SABRE2-V2," white.ce.gatech.edu/sabre (January 17).

Yarimci, E., Yura, J.A., and Lu, L.W. (1967), "Techniques for Testing Structures Permitted to Sway," *Experimental Mechanics*, Vol. 7, No. 8, Reprint, Fritz Laboratory Reports, Paper 112, http://preserve.lehigh.edu/engr-civil-environmental-fritz-lab-reports/112.

Ziemian, R.D. (Ed.) (2010), *Guide to Stability Design Criteria for Metal Structures*, 6th Ed., John Wiley & Sons, Inc., Hoboken, N.J.

Steel Structures Research Update

Structural Fire Engineering

JUDY LIU

INTRODUCTION

Across the United States, researchers are making exciting discoveries and advances in structural fire engineering. Eleven of the leading scholars in the field are featured. Brief research highlights are organized by the topic areas of behavior and design of steel and composite structures for fire, fire following earthquakes, and performance-based fire engineering. For each individual, related steel and fire research is also noted. Meanwhile, due to timing and circumstances, there are structural fire engineering researchers who do not appear in this article. You may find some of their structural steel research in past articles or perhaps a future research update.

BEHAVIOR AND DESIGN OF STEEL AND COMPOSITE STRUCTURES FOR FIRE

Dr. Lisa Choe, Dr. Venkatesh Kodur, Dr. M.Z. Naser, Dr. Erica Fischer, and Dr. Amit Varma are contributing in various ways to the behavior and design of steel and composite structures for fire. A two-story steel framed building specimen is used for fire tests of full-scale composite floor assemblies. System behavior and onset of collapse are investigated in a numerical study of braced frame buildings. Machine learning is used for autonomous evaluation of fire resistance. Validated modeling techniques are used to study fire and fire following earthquake behavior of steel moment-resisting frames. Comprehensive design procedures are developed for a new concrete-filled steel plate shear wall system.

Fire Resistance of a Full-Scale Composite Floor Assembly

Under way at the National Institute of Standards and Technology (NIST) is a series of four compartment fire experiments on a full-scale two-story steel-framed building with composite floor slabs. Research structural engineer Dr. Lisa Choe is leading the team: Matthew Hoehler (associate project leader), Matthew Bundy, Brian Story, Anthony Chakalis, Philip Deardorff, Selvarajah Ramesh, Xu Dai, and William Grosshandler. Team members Choe, Ramesh, Dai, Hoehler, and Bundy won the Best Paper Award at the 11th International Conference on Structures in Fire (SiF2020) for their paper, "Experimental Study on Fire Resistance of a Full-Scale Composite Floor Assembly in a Two-Story Steel Framed Building" (Choe et al., 2020b). Dr. Choe's honors also include the Department of Commerce Gold Medal in 2019, a group award for development of unique measurement capabilities for research at NIST's National Fire Research Laboratory (NFRL).

The research seeks to fill gaps in knowledge in the behavior of steel-concrete composite floors and beams with simple shear connections subjected to fire. Previous studies were limited with regard to beam span, boundary conditions for the concrete on metal deck slabs, and other details for the composite system (Choe et al. 2020a). Four 42-ft partially composite beam specimens were explored in the first phase of the work. Type of shear connection (welded-bolted double angle or shear tab) and slab continuity over the girder were the main parameters. The double angles had greater rotational ductility than the shear tabs in fire but could fail due to axial restraints in the cooling phase. The shear tabs were sensitive to the slab continuity in both the heating and cooling phases (Choe et al. 2020a). In the second phase, 20-ft × 30-ft composite floor assemblies are exposed to natural gas-fueled compartment fires simulating standard fire environments [Figure 1(a)]. Gravity loads are applied by frames connected to hydraulic actuators in the basement; adjacent bays are loaded with water-filled drums [Figure 1(b)]. Test variables include area and type of steel reinforcement in composite floor slabs; fire protection on exposed beams; and thermal restraints provided by the adjacent bays, such as bay beam framing, beam-end connections, and slab continuity. In the first experiment, the fire test compartment represented an edge bay on the first floor of the building. Prescriptive details of the floor specimen complied with a 2-hr fire resistance rating. Connections were shear tabs, and the minimum shrinkage reinforcement was used in the floor slab. The reinforcement ruptured before any membrane action could be developed, leading to integrity failure of the floor slab prior to the specified rating period (Choe et al., 2020b). Slab reinforcement and fire performance of composite floor systems were explored further with the second test in 2021 (Choe et al., 2021).

Judy Liu, PhD, Research Editor of the AISC *Engineering Journal*, Professor, Oregon State University, School of Civil and Construction Engineering, Corvallis, Ore. Email: judy.liu@oregonstate.edu

Design and Construction of Fire-Resistant Structures

Dr. Venkatesh Kodur contributes practical structural fire engineering tools and strategies founded on comprehensive numerical simulations and case studies. Dr. Kodur, University Distinguished Professor in Civil and Environmental Engineering at Michigan State University, also serves as the Director of the Centre on Structural Fire Engineering and Diagnostics. Dr. Kodur's research includes mitigation of fire-induced collapse of steel framed structures, utilizing comprehensive numerical models, and incorporating the development of temperature-induced strength degradation and instability in critical structural members with the progression of horizontal and vertical fire spread in different compartments and stories. One example is a simplified approach for evaluating shear degradation in fire-exposed steel and composite beams (Kodur and Naser, 2018). Fire safety of steel and composite bridges is another focus area; a specific aim is to develop practical tools for identifying vulnerable bridges and developing mitigation strategies. Honors include a 2018 Literati Award for Best Research Paper, "Effect of Local Instability on Fire Response of Steel Girders" (Kodur and Naser, 2017) and a 2019 Outstanding Paper Award at the 6th International Conference on Applications in Structural Fire Engineering, Singapore, for "Evaluating Fire Resistance of Composite Box Bridge Girders" (Zhang and Kodur, 2019). Dr. Kodur has also co-authored a textbook, *Structural Fire Engineering.* This comprehensive book explains codes and standards; high-temperature material properties; and behavior and strategies for enhancing fire resistance of steel, concrete, composite, and timber structures (Kodur and Naser, 2020).

The work on steel and composite structures includes system-level response of braced frame structures in fire scenarios (Venkatachari and Kodur, 2020). This work sought to fill knowledge gaps with respect to system behavior and the onset of collapse (Figure 2). The literature shows that "limited attention is given to the effect of parameters such as realistic loading, restraint and fire exposure scenarios which can significantly influence the onset of instability in the structure" (Venkatachari and Kodur, 2020). The analysis of a 10-story braced frame building was conducted for different fire scenarios. The likelihood of collapse was examined for parameters including fire location, temperature and duration of the fire exposure, and number of compartments with fire exposure. Additional details can be found in Venkatachari and Kodur (2020).

Autonomous Evaluation of Concrete-Filled Tube Columns

Performance of structures under extreme conditions, artificial intelligence, and smart materials and structures are core interests for Dr. M.Z. Naser, an Assistant Professor in Civil Engineering at Clemson University. Investigation into temperature-induced moment-shear interaction (Naser and Kodur, 2020) and performance evaluation of concrete-filled tubes through machine learning (Naser et al., 2021) are just some of Dr. Naser's recent works. Honors include the 2018 Literati Award for Best Research Paper with Dr. Kodur. Dr. Naser has published extensively in structural fire engineering and machine learning, with a focus on "intelligent tools that can accurately evaluate fire resistance and identify damage mechanisms in structures" and an eye toward "technologies to realize autonomous and self-diagnosing structures that can facilitate safe post-fire inspections and timely repairs" (Naser, 2020). His publications include the *Structural Fire Engineering* textbook co-authored with Dr. Kodur (Kodur and Naser, 2020) and the *Handbook of Cognitive and Autonomous Systems for Fire Resilient Infrastructures* (Naser and Corbett, 2022).

Briefly highlighted here is Dr. Naser's work on the structural response evaluation of concrete-filled tube (CFT) columns using machine learning (Naser et al., 2021). Dr. Naser and collaborators noted the benefits of CFTs for building design and construction, including strength, ductility, and

Fig. 1. (a) Compartment fires with natural gas burners and (b) floor loading.

inherent fire resistance. They also noted that the adoption of high-strength materials might be inhibited by the range of applicability of current code provisions and supporting test data. The researchers used artificial intelligence (AI) to analyze a database of 3103 CFT columns tested under different loading conditions and with a range of material and geometric properties. Circular and square or rectangular cross sections, with a maximum outside dimension of 40 in., had been tested under concentric and eccentric loading. The research team used genetic algorithms (GA) and gene expression programming (GEP) to develop models capable of predicting the CFT column load capacities. "These algorithms incorporate a supervised learning process that mimics the natural selection process (i.e., Darwinian evolution) to express hidden relations between a number of factors … The main advantage of these approaches over traditional soft computing techniques is their capability to produce predictive expressions without relying on past formula or relationship" (Naser et al. 2021). As shown in the measured versus predicted capacity graphs in Figure 3, the predictions were generally better than those obtained using AISC 360 (AISC, 2016), Eurocode 4 (CEN, 2009), and AS 2327 (ASI, 2017). Additional details of this study can be found in Naser et al. (2021).

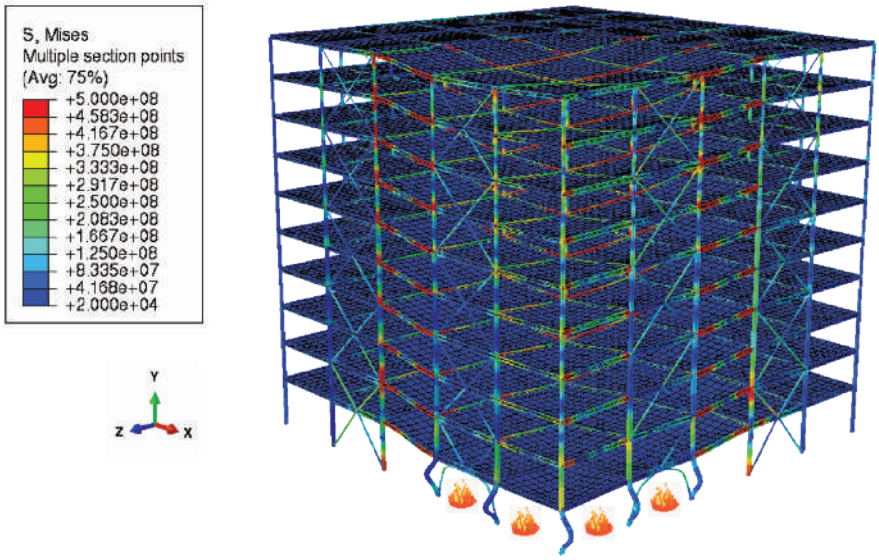

Fig. 2. Deformed configuration of the building at the onset of fire-induced progressive collapse (time = 154 min).

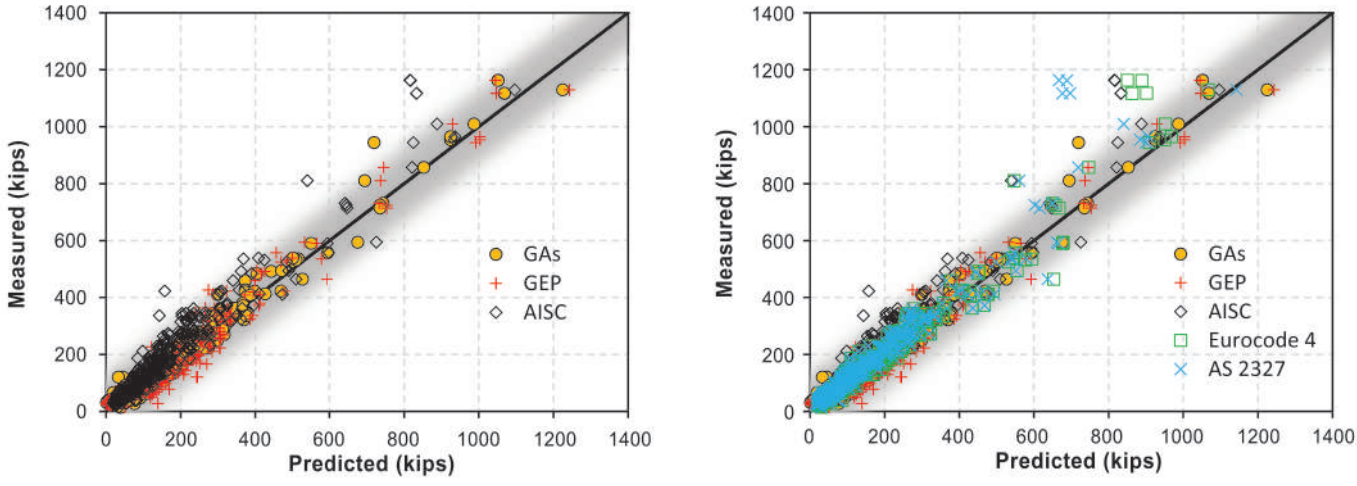

(a) AISC 360

(b) AISC 360, Eurocode 4, and AS 2327

Fig. 3. Measured versus predicted capacities for circular CFT columns under eccentric loading; genetic algorithms (GA) and genetic expression programming (GEP) predictions.

Development of Fire Modeling Capabilities in OpenSees

Simulating the behavior of steel and composite structures in fire, educating the next generation of structural engineers, and designing simple connections for fire conditions are three primary themes for Dr. Erica Fischer. Dr. Fischer is an Assistant Professor in the School of Civil and Construction Engineering at Oregon State University. Recognized locally and nationally for research and teaching excellence, Dr. Fischer's awards include AISC's Terry Peshia Early Career Faculty Award (2021). The American Society of Civil Engineers (ASCE) honored Dr. Fischer with the 2019 Collingwood Prize for her paper, "Experimental Evaluation of Single-Bolted Lap Joints at Elevated Temperatures" (Fischer and Varma, 2018). Her more recent work on connections includes advanced connection modeling, leading a working group within one of AISC's technical committees to synthesize numerical and experimental data on connection performance in fires and developing design provisions for connections exposed to various fire conditions. Dr. Fischer also led a collaborative research review on the fire behavior of steel simple connections, identifying gaps in knowledge and inconsistencies in testing methodologies and reporting of results (Fischer et al., 2021). Education on structural fire engineering extends past Dr. Fischer's classroom and to development of teaching modules with the support of AISC and the Structural Engineering Institute (SEI). The scope ranges from prescriptive fire protection design to structural fire engineering, and the modules are designed to be integrated into courses across civil engineering undergraduate curricula.

Simulation of fire performance of steel-frame buildings is a theme area with multiple facets. Dr. Fischer's research includes simulation of post-earthquake fire behavior of industrial facilities, benchmarking of structural fire engineering modeling to large-scale experimental tests, and development of OpenSees capabilities to simulate steel gravity framing systems in fire. Some work to date includes use of validated OpenSees modeling techniques to investigate fire and fire following earthquake behavior of a three-story, three-bay moment-resisting frame (Maddalozzo and Fischer, 2020). Five validation studies were used to test component and system behavior, considering temperature, forces, and displacements. Parameters for the fire and fire following earthquake investigations included locations of the compartment fire and the fuel load (Figure 4). Additional details can be found in Maddalozzo and Fischer (2020).

SpeedCore—Concrete-Filled Composite Steel Plate Shear Wall (CF-CPSW) Core

Dr. Amit Varma is well known for research on the behavior and analysis of steel and composite structures under fire loading and the development of design provisions for fire and collapse resistance. Dr. Varma is the Karl H. Kettelhut Professor in the Lyles School of Civil Engineering at

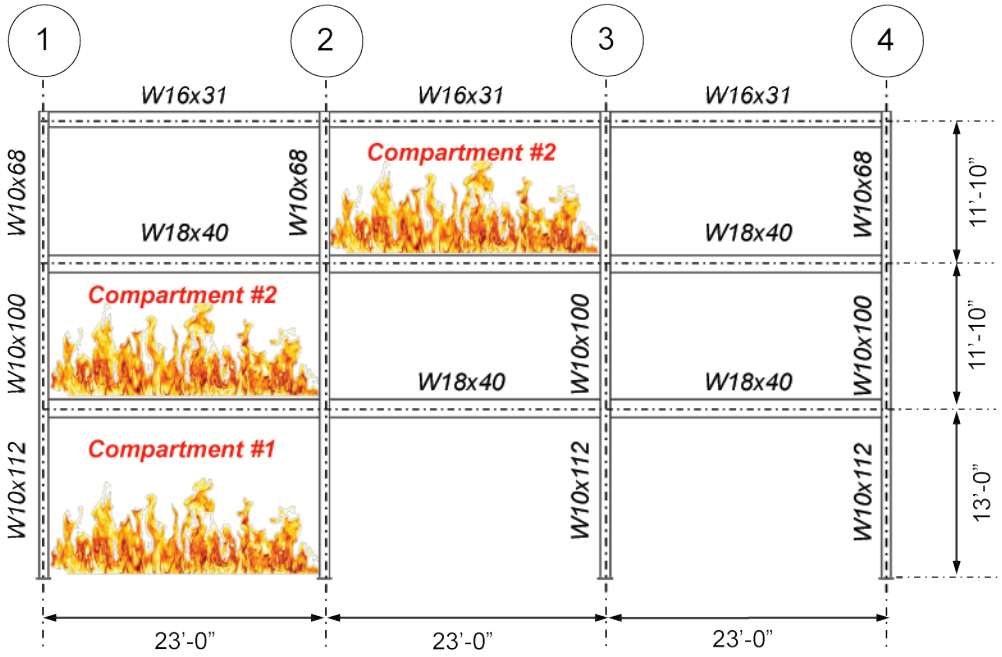

Fig. 4. Locations of compartment fires for moment-resisting frame study.

Purdue University and the Director of the Bowen Laboratory for Large-Scale Civil Engineering Research. While seeking to fill knowledge gaps in the fundamental behavior of structural steel components and assemblies, Dr. Varma pioneered an innovative method for realistic structural fire tests without the traditional gas furnace. Replication of this unique test method at several structural engineering laboratories across the world is just one indicator of Dr. Varma's global impact in this field. His research group has produced numerous works advancing the state of the art in behavior, analysis, and design for fire. Their achievements include publications on the fire behavior of steel and composite columns, composite floor assemblies, composite beams, and steel connections (e.g., Hong and Varma, 2010; Wellman et al., 2011; Selden et al., 2016; Fischer and Varma, 2018). Dr. Varma's group has also developed and benchmarked detailed 3D nonlinear finite element models for predicting the observed experimental behavior of steel connections and of steel and composite columns, floor assemblies, and beams (e.g., Agarwal and Varma, 2011; Selden and Varma, 2016; Choe et al., 2017; Fischer and Varma, 2017). The benchmarked modeling approaches have been used to investigate the fire behavior, resistance, and overall collapse of 3D steel and composite building structures (e.g., Agarwal and Varma, 2014; Agarwal et al., 2014; Fischer et al., 2019). The work has also been extended to evaluation of multi-hazard behavior and design of steel building structures under post-earthquake fire loading (e.g., Bhardwaj et al., 2019; Alasiri et al., 2020).

Dr. Varma's most recent accolades recognize his achievements in developing SpeedCore, a concrete-filled steel plate shear wall system with cost, safety, and construction schedule benefits, among others. An increased speed of construction is partly because no fireproofing is required for SpeedCore walls at least 18 in. thick (AISC, 2021). Dr. Varma's selections for 2017 and 2020 AISC Special Achievement Awards and the 2021 AISC T.R. Higgins Lectureship Award were based on his collection of work on the composite shear walls. More information about this hybrid core system, how it is designed and built, and how it works in fire can be found at AISC's SpeedCore webpage (AISC, 2021). Those looking for more information on the structural fire engineering and design of SpeedCore walls can view a series of recorded presentations on the "SpeedCore-Fire-Research" YouTube playlist (Figure 5; Varma, 2021). Computer programs to analyze and design SpeedCore walls for fire are available through an online repository (Varma and Anvari, 2020).

FIRE FOLLOWING EARTHQUAKES

Dr. Rachel Chicchi, Dr. Hussam Mahmoud, and Dr. Maria Garlock are advancing methods for fire following earthquake (FFE) evaluations. Three-dimensional nonlinear finite element building models explicitly include details of the gravity framing system and are used to compare different seismic damage–fire scenarios. A hybrid simulation framework incorporates thermal loads and seismic damage in the physical substructure. The seismic performance of nonstructural components (e.g., sprinklers) is incorporated into post-earthquake fire evaluations of steel frames.

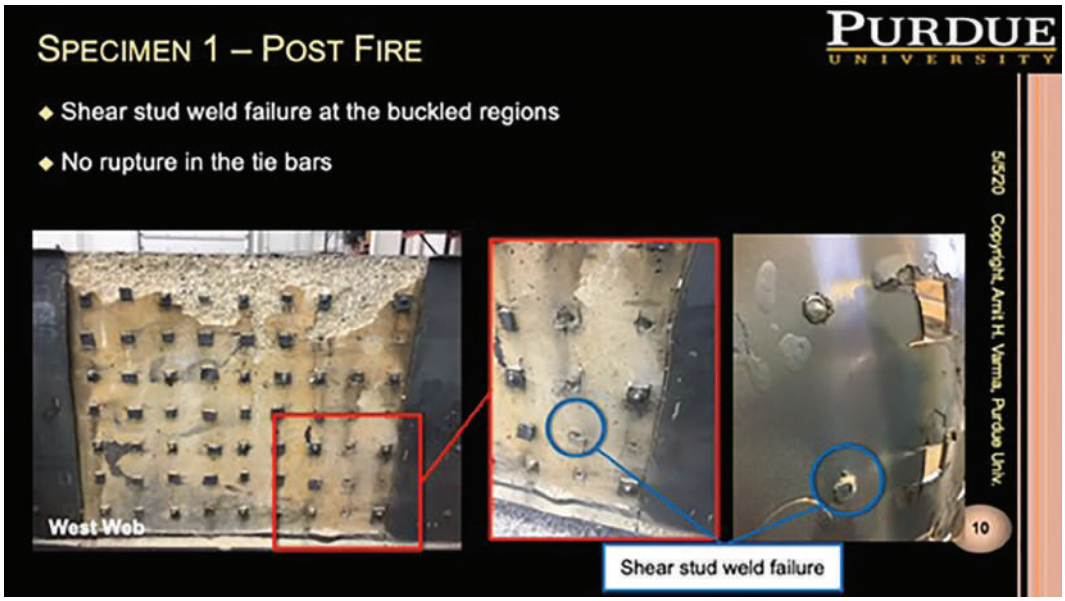

Fig. 5. Screenshot of video presentation on SpeedCore fire resistance experiments (Varma, 2021).

Post-Earthquake Fire Assessment

Post-earthquake fire assessment, critical temperature, simple methods of analysis for fire-resistant design, and connections are among Dr. Rachel Chicchi's topics of study. Dr. Chicchi is an Assistant Professor in the University of Cincinnati's Civil and Architectural Engineering and Construction Management department. She has collaborated with Dr. Fischer and Dr. Choe on a research review for fire behavior of simple shear connections (Fischer et al., 2021). Analysis of single-angle connections by her research group will address one of the knowledge gaps identified in the review. Work continues on simple methods of analysis to determine demands on the structure at elevated temperatures (Chicchi and Varma, 2021). One extension of the work is incorporation of local buckling for wide-flange columns into the simple equations. Another is an investigation into the applicability of the column flexural buckling equation for high-strength steel. In a separate study, important parameters affecting the critical temperatures of axially loaded wide-flange columns were identified and a closed-form equation proposed (Sauca et al., 2021). Meanwhile, post-earthquake fire assessment has evolved past an initial research review (Chicchi and Varma, 2017) into detailed studies and methods (e.g., Chicchi and Varma, 2018).

Dr. Chicchi's post-earthquake fire research includes methods for post-earthquake fire assessment of steel moment frame buildings (Alasiri et al. 2020). A detailed numerical methodology has been proposed and illustrated with a 10-story perimeter steel moment frame building case study. The nonlinear finite element model of the 3D building structure explicitly included the gravity framing system, including connections and composite slabs. "The model accounted for various limit states and failure modes resulting from inelastic deformations, local and global instability, and connection damage/failure at elevated temperatures, while incorporating the effects of temperature on steel and concrete material properties" (Alasiri et al., 2020). Buildings with different levels of seismic damage were subjected to various fire scenarios. Shown in Figure 6 is a fifth-story interior compartment fire and plots of the vertical deformation and temperature versus time for the failed interior gravity column. The researchers discovered that the seismic and fire behaviors were largely decoupled; the gravity columns were the most critical components in the post-earthquake fire. Additional details and design recommendations can be found in Alasiri et al. (2020).

Multi-Hazard Simulation and Testing

A primary research thrust for Dr. Hussam Mahmoud is the assessment and development of resilient and sustainable structural systems subjected to multiple hazards such as fire, blasts, earthquakes, and/or wind loading. Dr. Mahmoud is the George T. Abell Professor of Infrastructure in the Department of Civil Engineering at Colorado State University. He is also Director of the Structural Laboratory at Colorado State. Among his numerous recognitions and honors is the 2017 Terry Peshia Early Career Faculty Award from AISC. Dr. Mahmoud's contributions include new structural systems as well as new performance-based design and life-cycle analysis frameworks. Methods proposed include an approach for assessing steel column response under fire loads considering with various boundary conditions and temperature profiles (Memari and Mahmoud, 2018a). Also considered are factors such as second-order effects and

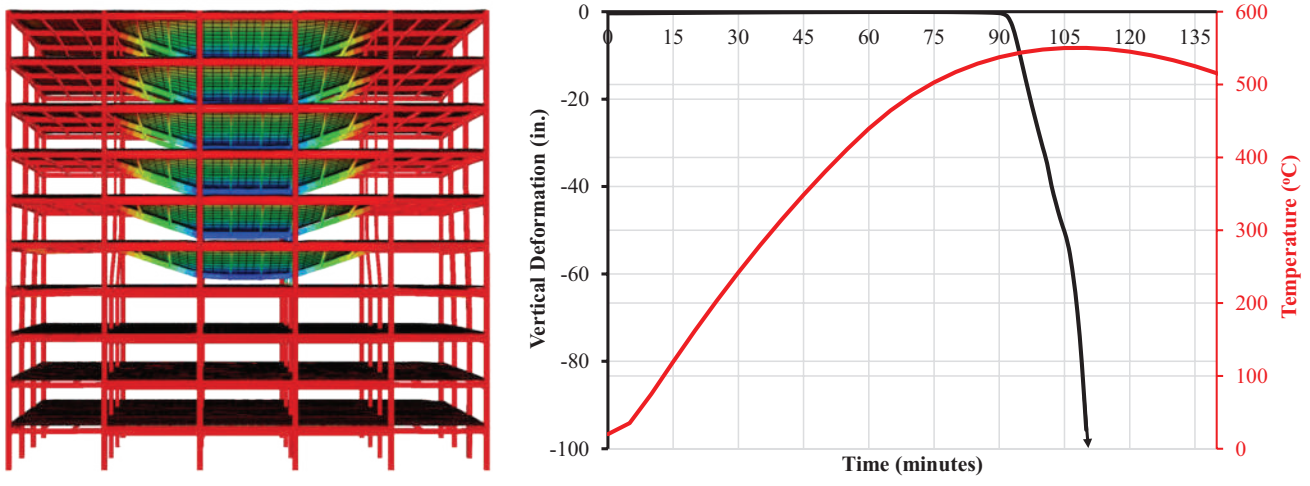

(a) *(b)*

Fig. 6. (a) Response of building to fifth-story interior compartment fire and (b) vertical deformation and temperature versus time for failed interior gravity column.

residual stresses. A proposed framework for performance-based analysis of fires following earthquakes incorporates uncertainties associated with fire hazard, gravity loads, passive fire protection, and earthquake intensity (Memari and Mahmoud, 2018b).

A hybrid simulation framework was developed and illustrated with a test of a small-scale specimen (Memari et al., 2020). The four-story special concentrically braced frame (SCBF) building was 5 ft × 5 ft in plan, with four bays in each direction. A first story column was the physical test specimen, the substructure model. The rest of the planar frame was the numerical integration model (Figure 7). Leaning columns in the model represented the gravity frames. The framework was first tested using a numerical substructure-numerical integration model. For the physical substructure model, a small fire furnace with four radiative heaters and a self-reacting steel frame was used for thermal loads, and residual interstory drifts were used to represent different seismic damage levels in the frame. The level of residual interstory drift proved to be a significant factor in the fire performance of the column. Additional details and commentary on future studies can be found in Memari et al. (2020).

Community Level Studies and Nonstructural Components

From steel connections for fire to community resilience to the Creative Art of Structural and Civil Engineering (CASCE, https://casce.princeton.edu/), Dr. Maria Garlock is advancing structural engineering design and the education of future engineers. Dr. Garlock is a Professor of Civil and Environmental Engineering at Princeton University. She also serves as the program director of the Architecture and Engineering Program, is the Head of Forbes College at Princeton University, and is Associated Faculty in both the School of Architecture and the Program in Latin American Studies. Of her many accolades, perhaps the most notable in structural steel is the 2016 T.R. Higgins Lectureship Award for her steel structure-fire interaction research (Garlock, 2016). Other awards include the Bronze Award for the Advancement of Arc Welded Design, Engineering and Fabrication, given by The James Lincoln Arc Welding Foundation (2003) and a first-place poster in the category of Steel Structures, Composite Structures, and Connections in the 5th International Conference for Structures in Fire in East Lansing, Michigan, in 2010. The poster, co-authored with former student Spencer Quiel, was titled "Stress-Based Equations for Predicting the Buckling Capacity of Steel Plates Exposed to Fire" (Quiel and Garlock, 2010).

Dr. Garlock notes that her research on fire has evolved into fire following earthquake (FFE) community-level studies, specifically considering deep-basin seismic effects such as those found in Seattle. A paper on FFE scenario studies in Seattle is forthcoming (Coar et al. 2021). Not published, but in preparation, is a paper that examines the effects of different earthquake types on passive and active fire protection systems, and consequential structural-fire interaction performance. Meanwhile, an archetype nine-story steel moment-resisting frame (MRF) structure is modeled using OpenSees finite element analysis software and subjected to a suite of basin (Seattle) and non-basin (Los Angeles) earthquake records as developed by the University of Washington M9 Project (Frankel et al., 2018). The resulting peak floor accelerations and interstory drift

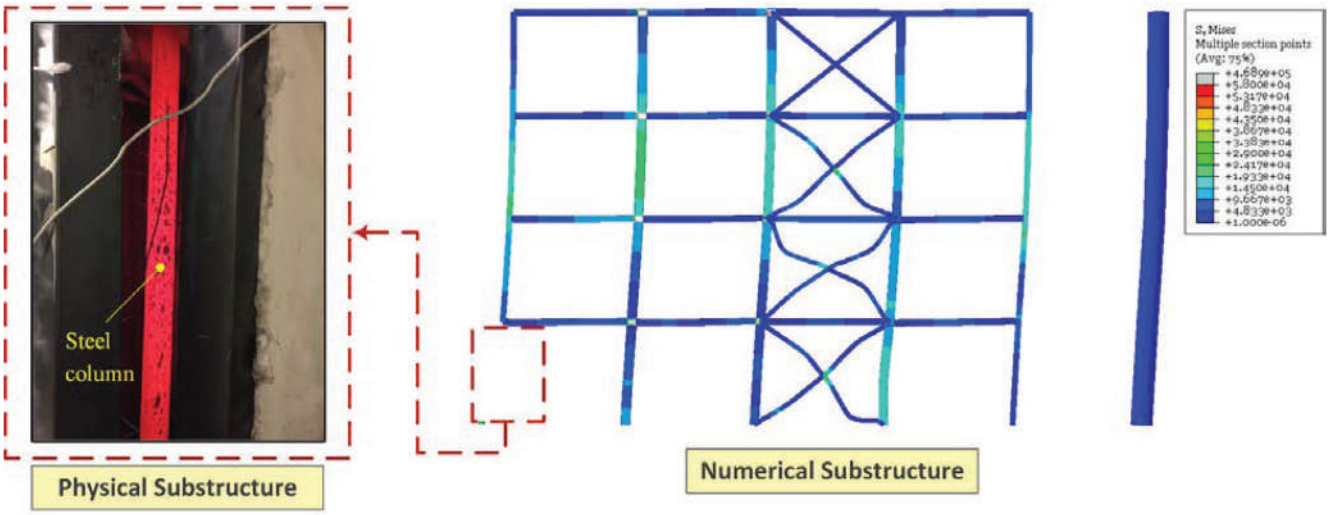

Fig. 7. Physical and numerical substructure, residual damage state.

ratios are used as intensity measures for existing component fragility curves of the active (sprinkler) and passive (compartment divider) fire protection systems (Pali et al., 2018; Soroushian et al., 2014). The seismic performance of these nonstructural components modifies the single-structure fire spread model based on the University of Delaware Disaster Research Center (Lee and Davidson 2010a, 2010b; Li and Davidson, 2013). The results of the fire spread model are used to apply time-dependent thermal loads to the seismically damaged OpenSees finite element structural model for structural performance evaluation of the steel frame (Figure 8).

PERFORMANCE-BASED FIRE ENGINEERING (PBFE)

Dr. Spencer Quiel, Dr. Negar Elhami-Khorasani, and Dr. Thomas Gernay are improving simulations for performance-based fire engineering (PBFE). A coordinated computational-experimental investigation supports a framework for realistic models of composite floor systems with different fire ratings. A cost-effective hybrid simulation incorporates realistic boundary conditions and system as well as element level response. Experimental characterization of advanced high-strength steels tests the range of applicability of current provisions.

Performance-Based Design of Passive Fire Protection for Floor Systems

Dr. Spencer Quiel is known for his research on buildings subjected to extreme loads such as fire, blast, and progressive collapse. Dr. Quiel is an Associate Professor in Civil and Environmental Engineering at Lehigh University. His experience in analysis and design of structures to resist extreme loads includes four years at Hinman Consulting Engineers. As a Department of Homeland Security Graduate Fellow, Dr. Quiel also spent two months of his doctoral studies at the Building and Fire Research Laboratory (BFRL) at the National Institute of Standards and Technology (NIST). Dr. Quiel was the 2016 recipient of AISC's Milek Fellowship for his research on "Performance-Based Design of Passive Fire Protection for Floor Systems in Steel-Framed Buildings."

For the Milek Fellowship, Dr. Quiel's research group is building a framework for performance-based design and analysis of steel-concrete composite floor systems to resist fire. The development of this framework for steel-framed buildings, motivated by the lack of design and analysis guidance, is founded on a coordinated computational-experimental investigation. Methods for quantifying realistic restraint of floor systems and modeling tools are being produced. The laboratory experiments include five large-scale structural-fire tests of partially restrained, partially

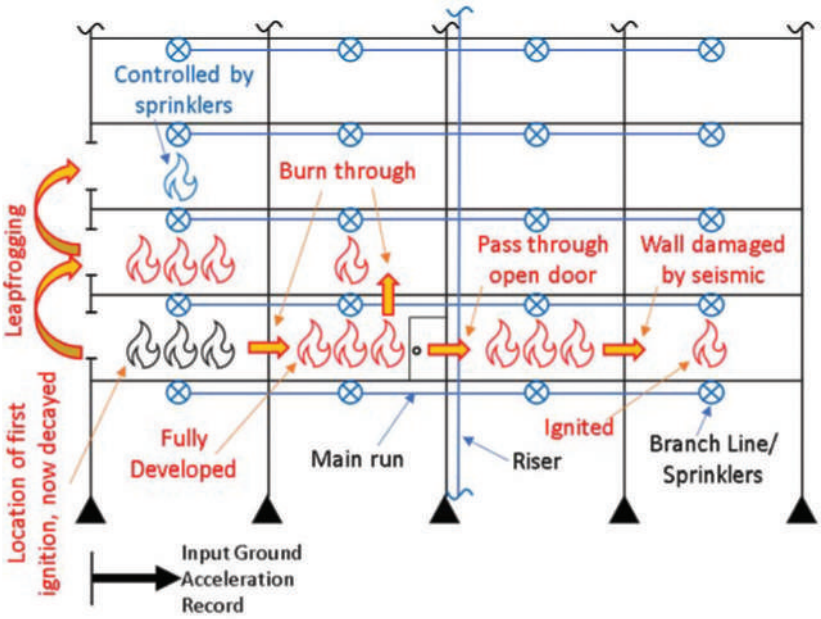

Fig. 8. Fire spread model for structural performance evaluation of steel frame.

composite steel floor beam assemblies and a number of small-scale, spray-applied fire resistive material (SFRM) tests. Parameters for the large-scale tests included passive fire protection (i.e., unprotected, coated with SFRM) and level of axial restraint (Kordosky et al. 2020). The experimental results have been used for validation of "thermal and structural analysis methods of varying complexity to capture the flexural response and failure of the fire-exposed composite floor beam specimens. The goal of this modeling effort is to develop accurate, conservative predictions of fire-induced mechanics and limit states at reduced computational cost, thus increasing the accessibility of these methods to practicing engineers" (Drury et al., 2020). A major outcome of the research will be tools for translating fire resistance ratings into realistic models of composite floor systems for performance-based design of steel buildings. Results have been promising, as demonstrated by comparisons of the final deflected shapes of the modeled and tested floor beam assemblies (Figure 9). Additional details of the experiments and modeling efforts can be found in Kordosky et al. (2020) and Drury et al. (2020).

Methods and Models to Advance Performance-Based Fire Engineering

Fire and elevated temperatures on steel structures is a primary focus for Dr. Negar Elhami-Khorasani, whose research encompasses resilient communities, performance-based design, reliability, and multi-hazard analysis. Dr. Elhami-Khorasani is an Assistant Professor in the Department of Civil, Structural and Environmental Engineering at the University at Buffalo. In Dr. Elhami-Khorasani's portfolio of work are topics such as parametric studies for performance-based fire design of composite floor systems and fire fragility functions for steel frame buildings (Elhami-Khorasani et al., 2019; Gernay et al., 2018). More recent research includes "Probabilistic Models for Temperature Dependent Strength of Steel and Concrete" and "Developing Real-Time Hybrid Simulation to Capture Column Buckling in a Steel Frame under Fire" (Qureshi et al., 2020a, 2020b). Qureshi et al. (2020b) received the best student paper award at the International Structures in Fire Conference in 2020. Dr. Elhami-Khorasani was also honored in 2020 with AISC's Terry Peshia Early Career Faculty Award, recognizing her structural steel research, teaching, technical service, and community outreach.

Dr. Elhami-Khorasani seeks to advance performance-based fire engineering (PBFE) through the development of methods and models for explicit evaluation of reliability and fire safety. Probabilistic material models for steel and concrete incorporate uncertainties in material behavior at elevated temperatures (Qureshi et al. 2020a). Qureshi et al. (2020a) also studied the influence of model choice on structural failure assessment of steel and concrete columns exposed to fire. This work was in collaboration with Dr. Thomas Gernay from Johns Hopkins University, Dr. Ruben Van Coile from Ghent University in Belgium, and Dr. Danny Hopkin from Olsson Fire & Risk and the University of Sheffield in the UK. Meanwhile, Dr. Elhami-Khorasani's work on real-time hybrid simulation provides a cost-effective method for obtaining realistic element-level response of the physical substructure by properly incorporating system-level response and interfacing boundary conditions during the fire event through a numerical substructure (Qureshi et al., 2020b). The proposed method was successfully applied to a benchmark study of a large-scale moment frame with buckling of one tube column subjected

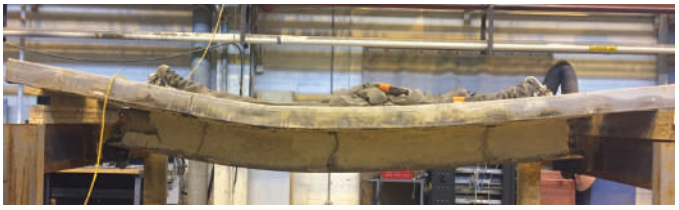

(a) Post-test photo

(b) Model at failure: S-TT

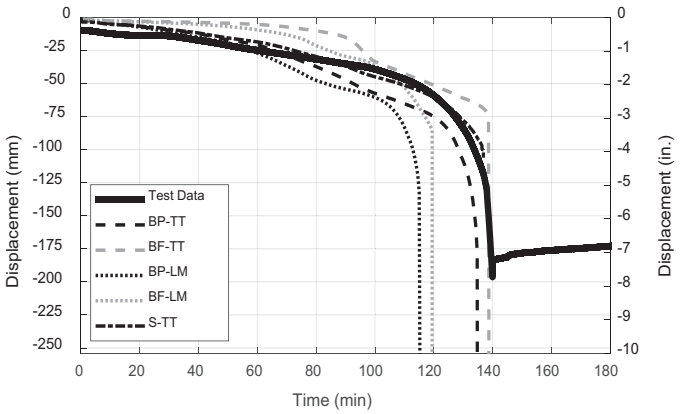

(c) Vertical displacement time histories: Test vs. all model iterations

Fig. 9. Results of testing and modeling for a protected W12×26 *composite beam.*

to fire and subsequent frame collapse (Figure 10). "The real-time hybrid fire simulation is able to capture the dynamic behavior at the time of column failure, for which the obtained result is also applicable to progressive collapse applications in general" (Qureshi, 2021).

Characterization of New Steels at Elevated Temperatures

Risk-based methodologies, numerical modeling, and characterization of materials at elevated temperatures form the core of Dr. Thomas Gernay's contributions to performance-based fire engineering (PBFE). Dr. Gernay is an Assistant Professor in the Department of Civil and Systems Engineering at Johns Hopkins University. The founder and principal investigator for Johns Hopkins' Multi-Hazard Resilient Structures research group, Dr. Gernay actively develops SAFIR, a nonlinear finite element software for modeling the behavior of structures in fire, and conducts research on topics ranging from properties of advanced high-strength steels at elevated temperatures (Yan et al., 2020, 2021a, 2021b) to behavior of cold-formed steel structures during and after fire exposure (Batista Abreu et al., 2020, 2021). Dr. Gernay's research portfolio also includes fire fragility functions, probabilistic material models, and performance-based fire design and tensile membrane action in composite structures (Qureshi et al., 2020a; Gernay et al., 2018; Gernay and Khorasani, 2020).

Dr. Gernay's experimental materials characterization at elevated temperatures continues to strengthen computer simulation capabilities, especially with respect to behavior of new steels. This includes steels more commonly found in the automotive industry. Yan et al. (2020) investigated advanced high-strength steels (AHSS), taking the recent demand for high-performance steels in the major projects such One World Trade Center as a harbinger of the adoption of "next-generation" materials for economy, safety, and construction efficiency. Dual-phase (DP) and martensitic (MS) steels were tested at elevated temperatures and under steady-state (66 specimens) and transient-state conditions (22 specimens). Steady-state tests began with heating to a target temperature and then loading until fracture. Transient-state conditions involved loading to target stress levels and then heating at a constant rate. Several materials and a half a dozen different grades of steel were evaluated for strength, ductility, and stress-strain behavior under temperatures ranging from ambient to 1290°F. Figure 11 shows the test set-up and a set of AHSS specimens after the steady-state tests. "With increasing temperature, the specimens became softer and showed more ductile failures, with increasing fracture strain and clear necking phenomena" (Yan et al., 2020). Retention factors and predictive models were developed for the different materials. At elevated temperatures, the tested AHSS showed larger reductions in properties than their lower-grade counterparts. Revisions are needed to expand the applicability of current provisions to AHSS. Additional details can be found in Yan et al. (2020).

SUMMARY

Structural fire engineering researchers are making advances in the broad topic areas of behavior and design of steel and composite structures for fire, fire following earthquakes, and performance-based fire engineering. Specific topics include behavior of full-scale composite floor assemblies in fire, system behavior and onset of collapse of braced frame buildings, and machine learning for autonomous evaluation of fire resistance. Comprehensive design procedures are developed for composite core wall systems. Hybrid simulation frameworks incorporate thermal loads,

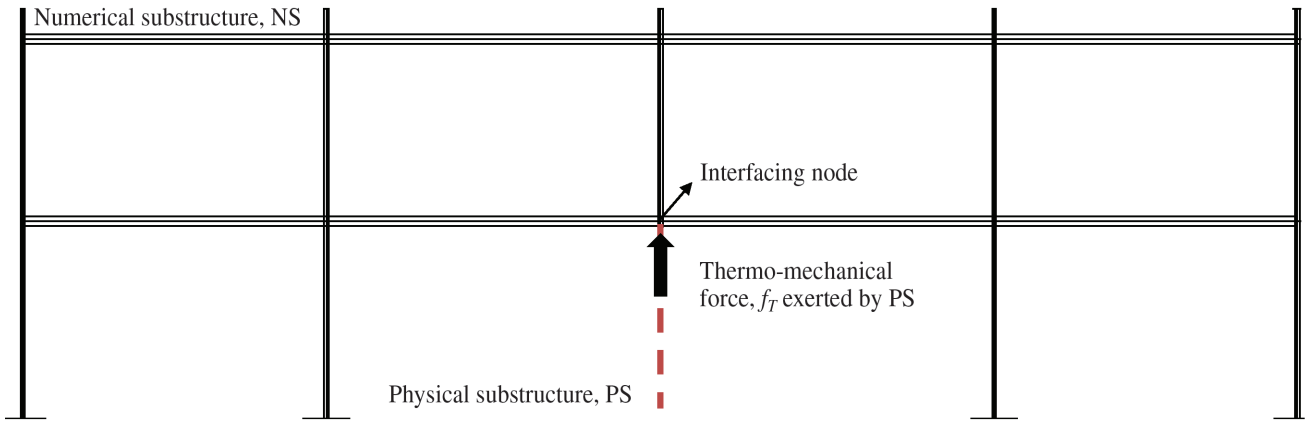

Fig. 10. Substructuring configuration for the benchmark study.

seismic damage, and realistic boundary conditions. Validated modeling techniques are being used to study fire and fire following earthquake behavior of steel frames; realistic models of composite floor systems are developed, and different seismic damage–fire scenarios are explored. Materials characterization expands modeling capabilities to new steels. The seismic performance of nonstructural components (e.g., sprinklers) is incorporated into post-earthquake fire evaluations of steel frames, and fire following earthquake is investigated at a community level.

ACKNOWLEDGMENTS

Many thanks to the featured researchers for their contributions. A very special thank you to Dr. Erica Fischer whose excellent suggestion and coordination made this article possible. Any findings or recommendations are those of the researchers and do not necessarily reflect the views of the sponsors.

REFERENCES

AISC (2016), *Specification for Structural Steel Buildings*, ANSI/AISC 360-16, American Institute of Steel Construction, Chicago, Ill.

AISC (2021), "Speedcore," https://www.aisc.org/why-steel/innovative-systems/SpeedCore/#55717.

Agarwal, A., Selden, K., and Varma A.H. (2014), "Stability Behavior of Steel Building Structures in Fire Conditions: Role of Composite Floor System with Shear-Tab Connections," *Journal of Structural Fire Engineering, Special Issue on Structures in Fire-2012 Conference,* Vol. 5, No. 2, June. http://dx.doi.org/10.1260/2040-2317.5.2.77

Agarwal, A. and Varma, A.H. (2011), "Design of Steel Columns for Fire Loading Including Effects of Rotational Restraints," *Engineering Journal,* AISC, Vol. 48, No. 4, pp. 297–314.

Agarwal, A. and Varma, A.H. (2014), "Fire Induced Progressive Collapse of Steel Building Structures: The Role of Interior Gravity Columns," *Engineering Structures, Special Issue on Fire Analysis of Structures,* Vol. 58, pp. 129–140. http://dx.doi.org/10.1016/j.engstruct.2013.09.020

Alasiri, M., Chicchi, R., and Varma, A.H. (2020), "Post-Earthquake Fire Behavior and Structural Performance-Based Fire Design of a Steel Moment Frame Building," *Journal of Constructional Steel Research*, Vol. 177.

ASI (2017), *Australian Composite Structures Standard*, AS 2327, Australian Steel Institute, Sydney, Australia.

Batista Abreu, J.C., Vieira Jr., L.C.M., Moreno Jr., A.L., Gernay, T., and Schafer, B.W. (2020), "Experiments on Load-Bearing Cold-Formed Steel Sheathed Studs at Elevated Temperatures," *Thin-Walled Structures,* Vol. 156, 106968.

Batista Abreu, J.C., Vieira Jr., L.C.M., Gernay, T., and Schafer, B.W. (2021), "Cold-Formed Steel Sheathing Connections at Elevated Temperature," *Fire Safety Journal,* Vol. 123, 103358.

Bhardwaj, S.R., Sener, K.C., and Varma, A.H. (2019), "Multi-Hazard Investigation and Testing of Composite (SC) Wall Piers: Seismic and Thermal Loads," *Nuclear Engineering and Design,* Vol. 348, pp. 121–130. https://doi.org/10.1016/j.nucengdes.2019.03.026

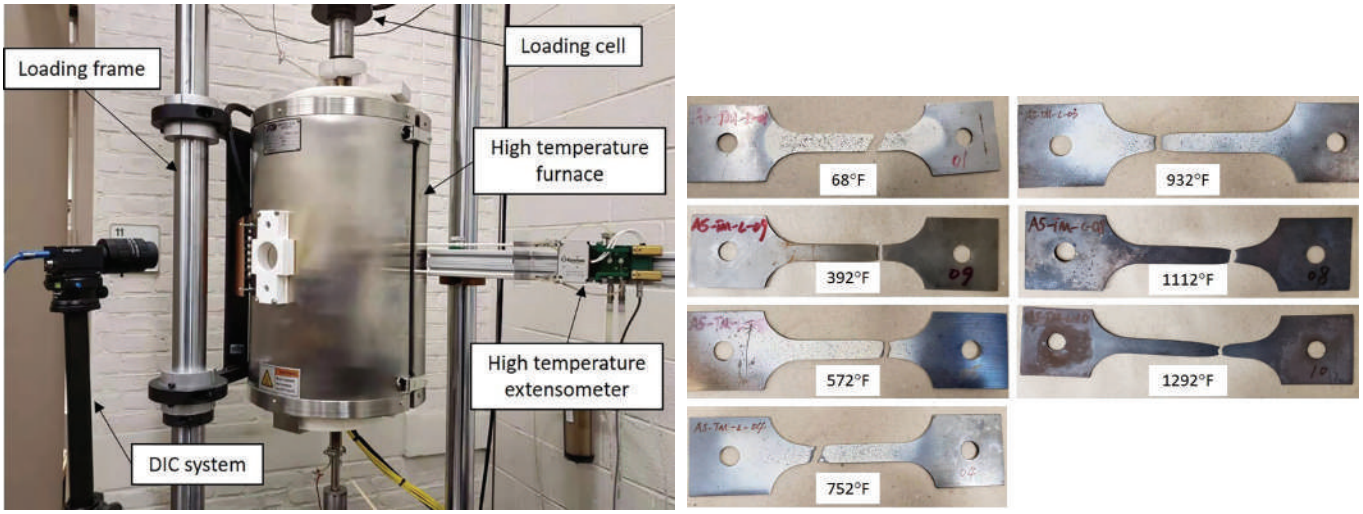

(a) *(b)*

Fig. 11. (a) Test set-up and (b) a set of AHSS specimens after testing.

CEN (2009), *Eurocode 4: Design of Composite Steel and Concrete Structures*, Comite Européen de Normalisation, Brussels, Belgium.

Chicchi, R. and Varma, A.H. (2017), "Research Review: Post-Earthquake Fire Assessment of Steel Moment Frame Buildings," *Advances in Structural Engineering*. https://doi.org/10.1177/1369433217711617

Chicchi, R. and Varma, A.H. (2018), "Assessment of Post-Earthquake Fire Behavior of a Steel MRF Building in a Low Seismic Region," *International Journal of Steel Structures*, Vol. 18, No. 4, pp. 1470–1481. https://doi.org/10.1007/s13296-018-0183-y

Chicchi, R. and Varma, A.H. (2021), "Comparison of Simple and Advanced Methods of Analysis in AISC 360 for Fire Resistant Structural Design," *Engineering Journal*, AISC [accepted pending revisions].

Choe, L., Ramesh, S., Dai, X., Hoehler, M., and Bundy, M. (2020b), "Experimental Study on Fire Resistance of a Full-Scale Composite Floor Assembly in a Two-Story Steel Framed Building," *SiF 2020—The 11th International Conference on Structures in Fire,* Brisbane, Australia, November 30–December 2.

Choe, L., Ramesh, S., Grosshandler, W., Hoehler, M., Seif, M., Gross, J., and Bundy, M. (2020a), "Behavior and Limit States of Long-Span Composite Floor Beams with Simple Shear Connections Subject to Compartment Fires: Experimental Evaluation," *Journal of Structural Engineering*, ASCE. https://doi.org/10.1061/(ASCE)ST.1943-541X.0002627

Choe, L., Ramesh, S., Zhang, C., and Clifton, C. (2021), "Behaviour of Composite Floor Assemblies Subject to Fire: Influence of Slab Reinforcement." *Proceedings of 2021 Eurosteel Conference,* September 1–3, University of Sheffield, United Kingdom (in production).

Choe, L., Zhang, C., Luecke, W., Gross, J., and Varma, A.H. (2017), "Influence of Material Models on Predicting the Fire Behavior of Steel Columns," *Fire Technology*, Vol. 53, No. 1, pp. 375–400. http://dx.doi.org/10.1007/s10694-016-0568-4

Coar, M., Sarreshtehdari, A., Garlock, M.E.M., and Elhami-Khorasani, N. (2021), "Methodology and Challenges of Fire Following Earthquake Analysis: An Urban Community Study Considering Water and Transportation Networks," *Natural Hazards*, in press.

Drury, M.M., Kordosky, A.N., and Quiel, S.E. (2020), "Structural Fire Resistance of Partially Restrained, Partially Composite Floor Beams, II: Modeling," *Journal of Constructional Steel Research*, Vol. 167. https://doi.org/10.1016/j.jcsr.2020.10594

Elhami-Khorasani, N., Gernay T., and Fang, C. (2019), "Parametric Study for Performance-Based Fire Design of US Prototype Composite Floor Systems," *Journal of Structural Engineering*, ASCE, Vol. 145, No. 5.

Fischer, E., Agarwal, A., and Varma, A.H. (2019), "Performance-Based Structural Fire Engineering of Steel Building Structures: Design-Basis Compartment Fires," *Journal of Structural Engineering,* ASCE, Vol. 145, No. 9. https://doi.org/10.1061/(ASCE)ST.1943-541X.0002370

Fischer, E., Chicchi, R., and Choe, L. (2021), "Review of Research on the Fire Behavior of Simple Shear Connections," *Fire Technology,* April.

Fischer, E. and Varma, A.H. (2017), "Fire Resilience of Composite Beams with Simple Connections: Parametric Studies and Design," *Journal of Constructional Steel Research,* Vol. 128, pp. 119–135. http://dx.doi.org/10.1016/j.jcsr.2016.08.004

Fischer, E. and Varma, A.H. (2018), "Experimental Evaluation of Single-Bolted Lap Joint at Elevated Temperatures," *Journal of Structural Engineering,* ASCE, Vol. 144, No. 1. https://doi.org/10.1061/(ASCE)ST.1943-541X.0001911

Frankel, A., Wirth, E., Marafi, N., Vidale, J., and Stephenson, W. (2018), "Broadband Synthetic Seismograms for Magnitude 9 Earthquakes on the Cascadia Megathrust Based on 3D Simulations and Stochastic Synthetics, Part 1: Methodology and Overall Results," *Bulletin of the Seismological Society of America,* Vol. 108.5A, pp. 2,347–2,369.

Garlock, M. (2016), "T.R. Higgins Lecture: Get Fired Up: What Structural Engineers Should Know about Fire Design," *Proceedings of NASCC: The Steel Conference,* April 13–15, Orlando, Fla. https://www.aisc.org/education/continuingeducation/education-archives/t.r.-higgins-lecture-get-fired-up-what-structural-engineers-should-know-about-fire-design-n79/

Gernay, T., Elhami-Khorasani, N., and Garlock, M.E.M. (2018), "Fire Fragility Functions for Steel Frame Buildings: Sensitivity Analysis and Reliability Framework," *Fire Technology*, Vol. 55, 1175. https://doi.org/10.1007/s10694-018-0764-5

Gernay, T., and Khorasani, N. E. (2020), "Recommendations for Performance-Based Fire Design of Composite Steel Buildings Using Computational Analysis," *Journal of Constructional Steel Research,* Vol. 166, 105906.

Hong, S. and Varma, A.H. (2010), "Predicting Column Buckling under Fire Loading Using Fundamental Section Behavior," *Journal of ASTM International,* ASTM, Vol. 7, No. 1. http://dx.doi.org/10.1520/JAI102311

Kodur, V.K.R. and Naser, M. (2017), "Effect of Local Instability on Fire Response of Steel Girders," *PSU Research Review Journal,* Vol. 1, No. 2, pp. 170–179.

Kodur, V.K.R. and Naser, M.Z. (2018), "Approach for Shear Capacity Evaluation of Fire Exposed Steel and Composite Beams," *Journal of Constructional Steel Research,* Vol. 141, pp. 91–103.

Kodur, V.K.R. and Naser, M.Z. (2020), *Structural Fire Engineering*, McGraw-Hill Professional (Education), New York, N.Y. ISBN 126012858X, 9781260128581

Kordosky, A.N., Drury, M.M., and Quiel, S.E. (2020), "Structural Fire Resistance of Partially Restrained, Partially Composite Floor Beams, I: Experiments," *Journal of Constructional Steel Research*, Vol. 167, https://doi.org/10.1016/j.jcsr.2020.105945

Lee, S.W., and Davidson, R.A. (2010a), "Application of a Physics-Based Simulation Model to Examine Post-Earthquake Fire Spread," *Journal of Earthquake Engineering,* Vol 14.5, pp. 688–705. ISSN: 13632469. DOI: 10.1080/13632460903336936

Lee, S.W. and Davidson, R.A. (2010b), "Physics-Based Simulation Model of Post-Earthquake Fire Spread," *Journal of Earthquake Engineering,* Vol. 14.5, pp. 670–687. ISSN: 13632469. DOI: 10.1080/13632460903336928

Li, S. and Davidson, R.A. (2013), "Parametric Study of Urban Fire Spread Using an Urban Fire Simulation Model with Fire Department Suppression," *Fire Safety Journal,* Vol. 61, pp. 217–225. ISSN: 03797112; DOI: 10.1016/j.firesaf.2013. 09.017. URL: http://dx.doi.org/10.1016/j.firesaf.2013.09.017

Maddalozzo, W. and Fischer, E.C. (2020), "Post-Earthquake Fire Performance of Steel Buildings," *Proceedings of the 17th World Conference on Earthquake Engineering* (17WCEE), Sendai, Japan, September 13–18.

Memari, M. and Mahmoud, H. (2018a), "Design Formulation for Critical Buckling Stress of Steel Columns Subjected to Nonuniform Fire Loads," *Engineering Journal*, AISC, Vol. 55, No. 2, pp. 89–108.

Memari, M. and Mahmoud, H. (2018b), "Framework for a Performance-Based Analysis of Fires Following Earthquakes," *Engineering Structures,* Vol. 171. https://doi.org/10.1016/j.engstruct.2018.05.099

Memari, M., Wang, X., Mahmoud, H., and Kwon, O. (2020), "Hybrid Simulation of Small-Scale Steel Braced Frame Subjected to Fire and Fire Following Earthquake," *Journal of Structural Engineering*, ASCE, Vol. 146, No. 1. https://doi.org/10.1061/(ASCE)ST.1943-541X.0002466

Naser, M.Z. (2020), "Autonomous Fire Resistance Evaluation," *Journal of Structural Engineering*, ASCE, Vol. 146. https://doi.org/10.1061/(ASCE)ST.1943-541X.0002641

Naser, M.Z. and Corbett, G. (2022), *Handbook of Cognitive and Autonomous Systems for Fire Resilient Infrastructures*, Springer, to be released in 2022.

Naser, M.Z. and Kodur, V.K.R. (2020), "Temperature-Induced Moment-Shear Interaction in Steel Beams." *International Journal of Steel Structures*. Vol. 20, pp. 1,540–1,551. https://doi.org/10.1007/s13296-020-00388-4

Naser, M.Z., Thai S., and Thai, T. (2021), "Evaluating Structural Response of Concrete-Filled Steel Tubular Columns through Machine Learning," *Journal of Building Engineering*. https://doi.org/10.1016/j.jobe.2020.101888.

Pali, T., Macillo, V., Terracciano, M.T., Bucciero, B., Fiorino, L., and Landolfo, R. (2018), "In-Plane Quasi-Static Cyclic Tests of Nonstructural Lightweight Steel Drywall Partitions for Seismic Performance Evaluation," *Earthquake Engineering and Structural Dynamics,* Vol. 47, pp. 1,566–1,588. DOI: 10.1002/eqe.3031

Quiel, S.E. and Garlock, M.E.M. (2010), "Stress-Based Equations for Predicting the Buckling Capacity of Steel Plates Exposed to Fire," *Structures in Fire—Proceedings of the Sixth International Conference,* SiF'10, East Lansing, Mich., June 2–4.

Qureshi, R. (2021), "Evaluation of Steel Columns under Fire: Real-Time Hybrid Testing and Reliability Assessment," PhD Dissertation, University at Buffalo, Buffalo, N.Y.

Qureshi, R., Elhami-Khorasani, N., and Sivaselvan, M. (2020b), "Developing Real-Time Hybrid Simulation to Capture Column Buckling in a Steel Frame under Fire," *Proceedings of 11th International Conference on Structures in Fire,* Queensland, Australia, November 30–December 2.

Qureshi, R., Ni, S., Elhami-Khorasani, N., Van Coile, R., Hopkin, D., and Gernay, T. (2020a), "Probabilistic Models for Temperature Dependent Strength of Steel and Concrete," *Journal of Structural Engineering,* ASCE, Vol. 146, No. 6.

Sauca, A., Chicchi, R., Zhang, C., and Choe, L. (2021), "Critical Temperature of Axially Loaded Steel Members with Wide-Flange Shapes Exposed to Fire," *Engineering Journal*, AISC, Vol. 58, No. 1.

Selden, K., Fischer, E., and Varma, A.H. (2016), "Experimental Investigation of Composite Beams with Shear Connections Subjected to Fire Loading," *Journal of Structural Engineering,* ASCE, Vol. 142, No. 2. http://dx.doi.org/10.1061/(ASCE)ST.1943-541X.0001381, 04015118

Selden, K. and Varma, A.H. (2016), "Composite Beams under Fire Loading: Numerical Modeling of Behavior," *Journal of Structural Fire Engineering,* Vol. 7, No. 2, pp. 142–157. http://dx.doi.org/10.1108/JSFE-06-2016-011

Soroushian, S., Maragakis, E., Zaghi, A.E., Echevarria, A., Tian, Y. and Filiatrault, A. (2014), "Comprehensive Analytical Seismic Fragility of Fire Sprinkler Piping Systems," MCEER 14.0002.

Varma, A., (2021), "SpeedCore-Fire-Research." [Video playlist.] *YouTube*. https://www.youtube.com/playlist?list=PLv1o8rALuecH5N59niiCmrSmi3w_SZeci

Varma, A.H. and Anvari, A.T. (2020), "Fire Design of SpeedCore Walls and CFT Columns," Purdue University Research Repository. doi:10.4231/JQHG-1N93

Venkatachari S. and Kodur, V.K.R (2020), "System Level Response of Braced Frame Structures under Fire Exposure Scenarios," *Journal of Constructional Steel Research,* Vol. 170, 106073, pp. 1–22.

Yan, X., Abreu, J.C.B., Glauz, R.S., Schafer, B.W., and Gernay, T. (2021b), "Simple Three-Coefficient Equation for Temperature-Dependent Mechanical Properties of Cold-Formed Steels," *Journal of Structural Engineering*, Vol. 147, No. 4, 04021035.

Yan, X., Xia, Y., Blum, H.B., and Gernay, T. (2020), "Elevated Temperature Material Properties of Advanced High Strength Steel Alloys," *Journal of Constructional Steel Research,* Vol. 174, 106299.

Yan, X., Xia, Y., Blum, H. B., and Gernay, T. (2021a), "Post-Fire Mechanical Properties of Advanced High-Strength Cold-Formed Steel Alloys," *Thin-Walled Structures,* Vol. 159, 107293.

Wellman, E., Varma, A.H., Fike, R., and Kodur, V., (2011), "Experimental Evaluation of Thin Composite Floor Assemblies under Fire Loading," *Journal of Structural Engineering*, Special 9/11 Commemorative Issue, ASCE, Vol. 37, No. 9, pp. 1002–1016. http://dx.doi.org/10.1061/(ASCE)ST.1943-541X.0000451

Zhang, G. and Kodur, V.K.R. (2019), "Evaluating Fire Resistance of Composite Box Bridge Girders," *Proceedings: 6th International Conference on Applications of Structural Fire Engineering (ASFE'19)*, pp. 1–8, Singapore.